SALT Spectropolarimetry Commissioning

by

Janus Daniël Brink

Thesis presented for the degree of

Master of Science

In the Department of Astronomy

UNIVERSITY OF CAPE TOWN

Supervised by:

A/Prof. Patrick Woudt[1], Dr. David Buckley[2] and Dr. Stephen Potter[2]

October 2010

[1]Department of Astronomy, University of Cape Town

[2]South African Astronomical Observatory

Abstract

The large (∼10m) aperture of the Southern African Large Telescope (SALT) coupled with the unique capabilities of the Robert Stobie Spectrograph (RSS), promises unparalleled prospects for polarimetric observations on an 8 - 10 m class telescope. RSS is a complex and highly versatile first-generation instrument of the SALT. RSS-VIS, the visible arm spanning 320-900 nm, employs a high UV-transmitting optical design to support UV spectroscopy down to the atmospheric cutoff at 320nm (rare on large telescopes). The RSS-NIR arm, currently under construction, will extend the wavelength coverage into the near-infrared (to 1.7μm), allowing for simultaneous UV-VIS-NIR observations.

RSS resides at the f/4.2 prime focus and provides operational modes including long-slit and multi-object spectroscopy, Fabry-Perot imaging spectroscopy and narrow band imaging, all over an 8 arcmin diameter field of view. The RSS has the ability to combine linear and circular polarimetry, separately or an "all-Stokes" mode, with any of these modes, allowing a wide range of polarimetric capabilities.

Results from some of the first polarimetric commissioning observations with the RSS-VIS, collected in 2006, are presented here. A method for reducing SALT RSS spectropolarimetry data is proposed and verified on observations of unpolarized and polarized standard stars. The method includes robust spectrum extraction, the use of variance and data-quality planes for error propagation and analysis techniques to estimate the Stokes parameters, combined with estimates of systematic and extraction errors. The results provide estimates of telescope and instrumental polarization as well as a cali-

bration of the instrument's polarimetric position angle offset. The calibration results and reduction methods described here will be directly applicable to the pipeline data reduction of future RSS polarimetric data.

Keywords: polarimetry, spectropolarimetry, instrument calibration, RSS, SALT.

Acknowledgements

I would like to thank the following people for their help and support, without which this project would not have been possible:

- Patrick Woudt, David Buckley and Stephen Potter for their support as supervisor and co-supervisors, respectively.
- Ken Nordsieck, for his valuable input as Principal Investigator of the RSS instrument.
- Peter Dunsby for his assistance as NASSP coordinator.
- My wife, Anita, for all her support.

In memory of D.P. Rossouw.

Contents

Abbreviations

ADC	Analogue-to-digital converter
ADC	Atmospheric Dispersion Compensator
ADU	Analogue-to-digital unit
APD	Avalanche photo-diode
CCD	Charged-Coupled Device
DQ	Data Quality
FIF	Fibre Instrument Feed
HET	Hobby Eberly Telescope
HDF	Hubble Deep Field
HRS	High Resolution Spectrograph
IRAF	Image Reduction and Analysis Facility
LLNL	Lawrence Livermore National Laboratory
LMC	Large Magellanic Cloud
NASSP	National Astrophysics and Space Science Program
NIR	Near-Infrared
NOAO	National Optical Astronomy Observatories
PFIS	Prime Focus Imaging Spectrograph
PMT	Photomultiplier Tube
RMS	Root Mean Square

Abbreviations

SAAO	South African Astronomical Observatory
SAC	Spherical Aberration Corrector
SALT	Southern African Large Telescope
SALTICAM	SALT Imaging Camera
SMC	Small Magellanic Cloud
RSS	Robert Stobie Spectrograph
UV	Ultra-violet
VIS	Visible
VPH	Volume Phase Holographic (grating)

List of Figures

List of Tables

Chapter 1

Introduction

1.1 Introduction

The Southern African Large Telescope (SALT) is a 10-metre class optical telescope situated near the Karoo town of Sutherland in South Africa and is operated by the South African Astronomical Observatory (SAAO). The SALT was officially inaugurated in November 2005 and its main work-horse instrument - the Robert Stobie Spectrograph (RSS) (Nordsieck et al., 2001) - was installed one month earlier. Commissioning of RSS was performed in 2006. The RSS is a multi-purpose visible and ultraviolet prime-focus instrument catering for standard seeing-limited long-slit spectroscopy, multi-object spectroscopy, narrow-band Fabry-Perot imaging as well as polarimetry (Nordsieck et al., 2001).

As part of the RSS commissioning effort, this study is specifically concerned with investigating methods for reducing the raw data obtained from RSS spectropolarimetry observations and investigating the quality of the observations and the reduction methods by determining the extent of the systematic and extraction errors of each data set.

A reduction process for such data and a polarimetric calibration of the instrument

needed to be developed. A means of obtaining accurate signal-to-noise estimates of the reduced data is required as this is of key importance during polarimetric data reduction and analysis. In addition, a robust method of aperture tracing for high signal-to-noise data is required to minimise systematic errors. Aperture tracing is the task of defining appropriate regions of interest in an image to define the shape and extent of both the target spectrum and suitable background regions.

Finally an estimate of the RSS instrumental polarisation parameters needed to be characterised.

1.2 Approach

A method for preparing the raw data, extracting the spectra and determining the polarisation parameters based on data obtained from polarimetric standard stars is developed.

Data preparation includes mechanisms to handle artifacts such as cosmic rays and detector defects as well as estimating the noise level at each detector location. These meta-data are propagated via data-quality and variance planes throughout the reduction process in order to propagate errors correctly.

A spectrum extraction method is developed that robustly derives the spectra from the multiple image frames comprising a polarimetric observation. A mechanism to minimise variations in the aperture tracing of high signal-to-noise spectra is proposed.

Techniques for obtaining the polarisation parameters from these spectra is developed, including an improved "all-Stokes" method for determining simultaneous linear and circular polarisation parameters from an observation.

These reduction techniques are then applied to data from appropriate polarimeteric standard stars to verify the method as well as obtain initial results for calibrating the intrinsic polarisation characteristics of the instrument and telescope.

These results will provide a basis for reducing data obtained from future RSS spectropolarimetric observations, particularly the development of a polarimetric data reduction pipeline.

1.3 Thesis outline

Chapter 2 gives the theoretical background for this study - briefly describing the polarised nature of light and methods of analysing it. An overview of the SALT and the characteristics of the RSS is given in Chapter 3, while the processing techniques and models used in analysing the data are outlined in Chapter 4.

Chapter 5 describes the observations performed, the data obtained and discusses the results for each target.

A global overview of the results and concluding remarks are given in Chapter 6.

Chapter 2

Polarimetry

This chapter provides some background on the theory of the polarisation of light, methods for measuring its properties and its application to astronomy and astronomical instrumentation.

A brief treatment of the theory of polarised light is given below, starting with the wave equation of light, deriving ways to parameterise the polarisation properties of completely polarised coherent waves and finally generalising to partially polarised incoherent beams. A more detailed introduction to the subject is given, for example, by Ramachandran & Ramaseshan (1961), Shurcliff & Ballard (1964) and Clarke & Grainger (1971).

2.1 The polarised nature of light

From Maxwell's equations we have for the electric (**E**) and magnetic (**H**) fields:

$$\nabla \times \mathbf{E} = -\mu\mu_0 \frac{\partial \mathbf{H}}{\partial t} \tag{2.1}$$

$$\nabla \cdot \mathbf{H} = 0 \tag{2.2}$$

$$\nabla \times \mathbf{H} = \sigma E + \varepsilon\varepsilon_0 \frac{\partial \mathbf{E}}{\partial t} \tag{2.3}$$

$$\nabla \cdot \mathbf{E} = 0 \tag{2.4}$$

where ε, μ and σ are the dielectric constant, permeability and conductivity of the medium, respectively; with ε_0 and μ_0 respectively the dielectric constant and permeability of vacuum.

The wave equations resulting from these relationships are:

$$\nabla^2 \mathbf{E} - \sigma\mu\mu_0 \frac{\partial \mathbf{E}}{\partial t} - \varepsilon\varepsilon_0\mu\mu_0 \frac{\partial^2 \mathbf{E}}{\partial t^2} = 0 \tag{2.5}$$

and

$$\nabla^2 \mathbf{H} - \sigma\mu\mu_0 \frac{\partial \mathbf{H}}{\partial t} - \varepsilon\varepsilon_0\mu\mu_0 \frac{\partial^2 \mathbf{H}}{\partial t^2} = 0 \tag{2.6}$$

These form a set of six linear equations for which sinusoids and combinations of sinusoids are solutions. From the solutions the following main characteristics of the waves are evident:

1. The wave motion is transverse to the direction of propagation,
2. **E** and **H** are perpendicular to each other and in-phase,
3. the wave travels at velocity $c = \frac{1}{\sqrt{\varepsilon_0\mu_0}}$ in a vacuum and
4. slows to $\frac{1}{\sqrt{\varepsilon\varepsilon_0\mu\mu_0}}$ in other media. (Refractive index $(n) = c/v = \sqrt{\varepsilon\mu}$)

For the simple case of a sinusoidal wave in a non-conducting medium the solution for the electric vector in a right-handed cartesian coordinate system becomes:

$$\mathbf{E}(\mathbf{r}, t) = \mathrm{Re}\left[(E_{x0}, E_{y0}, 0)\, e^{i(\omega t - \frac{2\pi z}{\lambda})}\right] \tag{2.7}$$

or alternatively,

$$\mathbf{E}(\mathbf{r},t) = \left[E_{x0}\cdot\cos\left(\omega t - \frac{2\pi z}{\lambda}\right), E_{y0}\cdot\cos\left(\omega t - \frac{2\pi z}{\lambda}\right), 0\right], \tag{2.8}$$

which represents a plane wave at time t and position z traveling in the positive z direction with $x-$ and $y-$components of amplitudes E_{x0} and E_{y0}, respectively, with ω the angular frequency of the wave ($= 2\pi\nu$), ν is the frequency and λ the wavelength of the light.

In this case the locus of the tip of the electric vector at a fixed point in space would describe a straight line in the $x-y$ plane. Such a wave would be 100% *linearly* polarised.

As mentioned above, the linear combination of any number of sinusoidal waves also form a solution to the wave equations. Considering the case where two coherent linearly polarised waves are combined, one in the $x-$ and one in the $y-$direction, the resulting vector components become:

$$E_x = E_{x0}\cdot\cos\left(\omega t - \frac{2\pi z}{\lambda} + \delta_x\right), \tag{2.9}$$

$$E_y = E_{y0}\cdot\cos\left(\omega t - \frac{2\pi z}{\lambda} + \delta_y\right) \tag{2.10}$$

where δ_x and δ_y represent the relative phase shift between the waves.

Considering the resulting vector at, say $z = 0$, the above reduce to:

$$E_x = E_{x0}\cdot\cos\left(\omega t + \delta_x\right), \tag{2.11}$$

$$E_y = E_{y0}\cdot\cos\left(\omega t + \delta_y\right) \tag{2.12}$$

which traces an ellipse in the $x-y$ plane, describing the general case of an *elliptically polarised* beam. If the amplitudes of the two components are assumed equal and the phase difference $\delta_y - \delta_x = \pi/2$ the locus becomes a circle and the beam is called *circularly polarised*. The *handed-ness* is defined such that right-handed indicates an electric vector rotating clockwise when 'viewed' by an observer receiving the radiation and vice-versa for left-handed.

An equation describing the ellipse is obtained by eliminating t above, obtaining:

$$\frac{E_x^2}{E_{x0}^2} + \frac{E_y^2}{E_{y0}^2} - \frac{2E_xE_y\cos(\delta_y-\delta_x)}{E_{x0}E_{y0}} = \sin^2(\delta_y-\delta_x). \tag{2.13}$$

Though the four parameters E_{x0}, E_{y0}, δ_x and δ_y completely describe the shape of the polarisation ellipse, they are all related to the arbitrarily chosen reference frame. A more convenient parameterisation can be obtained by considering the *ellipticity* of the ellipse and the total *intensity* of the beam independently from the reference frame, while relating to the frame via the *azimuth* angle of the major axis of the ellipse and the *handedness* of the polarisation as follows:

$$I_p = a^2 + b^2 = E_{x0}^2 + E_{y0}^2, \tag{2.14}$$

$$\tan 2\psi = \frac{2E_{x0}E_{y0}\cos(\delta_y - \delta_x)}{E_{x0}^2 + E_{y0}^2}, \tag{2.15}$$

$$\frac{2\eta}{1+\eta^2} = \frac{2E_{x0}E_{y0}\sin(\delta_y - \delta_x)}{E_{x0}^2 + E_{y0}^2}, \tag{2.16}$$

where I_p indicates the total (polarised) intensity, ψ is the azimuth angle of the major axis, $|\eta|$ indicates the amount of ellipticity (*ellipticity* $= 1 - \eta; \eta \equiv b/a$, with a the major- and b the minor axis of the ellipse) and $\eta > 0$ indicates right-handed ($\eta < 0 \Rightarrow$ left-handed) polarisation.

The ellipticity can also be described by the *ellipticity angle* (χ) defined as:

$$\tan\chi = 1 - \eta, \tag{2.17}$$

as shown in Figure 2.1.

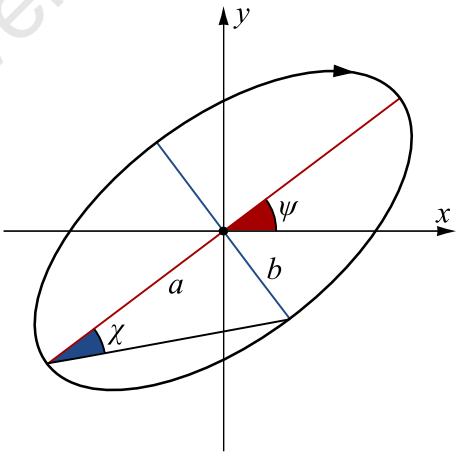

Figure 2.1: The polarisation ellipse.

A way of visualising the effect of an optical element (typically a retarder) on a polarised beam is to plot the parameters of the polarisation ellipse in a spherical coordinate

system, called the *Poincaré sphere*, as shown in Figure 2.2. The properties of the beam can be interpreted from the position of the vector I_p on the sphere: The V-axis indicates the degree of circular polarisation, with the poles at $+V$ and $-V$ representing right- and left-handed circular polarised light, respectively. Vectors located along the "equator" have $V = 0$ and are therefore linearly polarised with $+Q$ representing a purely horisontally polarised beam and $-Q$ a vertically polarised beam. Vectors on the $+U$ and $-U$ axes indicate linearly polarised light at $+45°$ and $-45°$ azimuth angles, respectively. Vectors with non-zero V, but $|V| < 1$ are therefore elliptically polarised with the azimuth of the major axis indicated by "longitude".

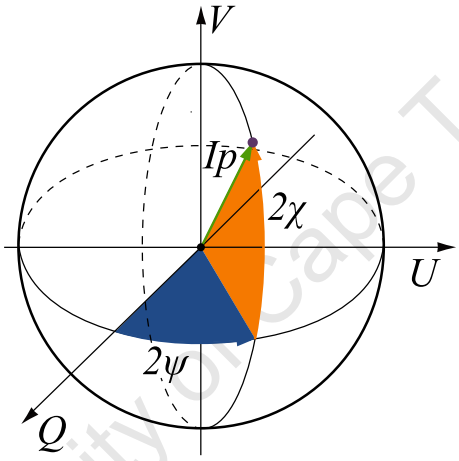

Figure 2.2: The Poincaré sphere.

The cartesian coordinate axes Q, U, and V are defined in terms of the parameters of the polarisation ellipse as follows:

$$Q = I_p \cos 2\psi \cos 2\chi \tag{2.18}$$

$$U = I_p \sin 2\psi \cos 2\chi \tag{2.19}$$

$$V = I_p \sin 2\chi \tag{2.20}$$

The parameters defined above apply to simple sinusoidal, perfectly polarised and coherent beams. In the more general case one requires parameters capable of describing the properties of partially polarised light formed by combining *incoherent* beams. This is accomplished by time-averaging the beam components to obtain a measure of affinity

of the beam for each of the parameters:

$$I = < E_x^2 + E_y^2 >, \tag{2.21}$$

$$Q = < E_x^2 - E_y^2 >, \tag{2.22}$$

$$U = < 2E_x E_y \cos(\delta_y - \delta_x) >, \tag{2.23}$$

$$V = < 2E_x E_y \sin(\delta_y - \delta_x) >, \tag{2.24}$$

where I indicates the total beam intensity and

$$\frac{I_p}{I} = \frac{\sqrt{Q^2 + U^2 + V^2}}{I} \tag{2.25}$$

denotes the degree of polarisation. The parameters I, Q, U and V are known as the *Stokes parameters* (Stokes, 1852). The power of the Stokes parameters are that they can be used to determine the result of combining two incoherent partially polarised beams by summation of their respective parameters to obtain the Stokes vector describing the polarisation characteristics of the resultant beam.

Mueller matrix calculus allows one to calculate the effect of various optical elements on an incident beam. The beam is described by its Stokes vector, while transformation due to the optical element is defined as a matrix. Some examples of optical operations and their corresponding Mueller matrices are shown in Table 2.1 (Serkowski, 1974).

2.2 Crystal optics

This section describes the use of optical elements manufactured from crystals that are typically used to determine the polarisation properties of a light beam. Some of the optical properties of crystals are discussed as well as their application to the optical elements typically used in constructing polarimeters.

The application of crystal optics in polarimeters may be appreciated by considering the six basic properties of such crystals (Schurcliff and Ballard, 1964):

1. In a uniaxial doubly-refracting crystal an incident beam generally splits into

Operation	Matrix	Notes
Perfect polariser	$\frac{1}{2}\begin{pmatrix} 1 & \cos 2\theta & \sin 2\theta & 0 \\ \cos 2\theta & \cos^2 2\theta & \frac{1}{2}\sin 4\theta & 0 \\ \sin 2\theta & \frac{1}{2}\sin 4\theta & \sin^2 2\theta & 0 \\ 0 & 0 & 0 & 0 \end{pmatrix}$	θ = principle plane of polariser.
Pure retarder	$\begin{pmatrix} 1 & 0 & 0 & 0 \\ 0 & G + H\cos 4\phi & H\sin 4\phi & -\sin\tau\sin 2\phi \\ 0 & H\sin 4\phi & G - H\cos 4\phi & \sin\tau\cos 2\phi \\ 0 & \sin\tau\sin 2\phi & -\sin\tau\cos 2\phi & \cos\tau \end{pmatrix}$	τ = retardance, ϕ = angle of the optic axis, $G = \frac{1}{2}(1+\cos\tau)$, $H = \frac{1}{2}(1-\cos\tau)$
Rotation	$\begin{pmatrix} 1 & 0 & 0 & 0 \\ 0 & \cos 2\gamma & \sin 2\gamma & 0 \\ 0 & -\sin 2\gamma & \cos 2\gamma & 0 \\ 0 & 0 & 0 & 1 \end{pmatrix}$	γ is measured anti-clockwise from the x-axis.

Table 2.1: Example Mueller matrices.

two surprisingly invariant beams (the polarisation state of the two beams are constrained by the medium).

2. Usually one of these beams have a direction of energy flow that is *oblique* rather than normal to the wavefronts.

3. Usually the two beams have different propagation speeds

4. Usually they have differing propagation directions

5. Each beam is perfectly polarised

6. The two polarisation forms are orthogonal.

Not all optical materials are isotropic (optically equivalent in all directions). In an anisotropic medium the medium's optical properties depend on the direction a light ray is traveling through the medium. In the case of a doubly-refracting crystal, its refractive index is anisotropic causing an incident beam of light to be refracted into

two distinct beams upon entering the medium - called the *ordinary* and *extra-ordinary* beam. The ordinary (or O-) beam is defined such that the electric vector of its light waves has a direction of vibration orthogonal to the crystal's optic axis and travels at a fixed speed of c/n_o, with c the velocity of light in a vacuum and n_o the invariant refractive index, or *major principal refractive index*. The extra-ordinary (or E-) beam travels at a *wave normal speed* c/n'_e, with n'_e dependent on the vibration direction. The *wave normal speed* ($V_\perp$) is defined as the speed solely dependent on the vibration direction of the wave:

$$V_\perp = V_r \cos A \tag{2.26}$$

with V_r the speed of energy flow (in the *ray direction*) and A the angle between the ray direction and the *wavenormal direction* - as depicted in Figure 2.3 (Ramachandran and Ramaseshan, 1961).

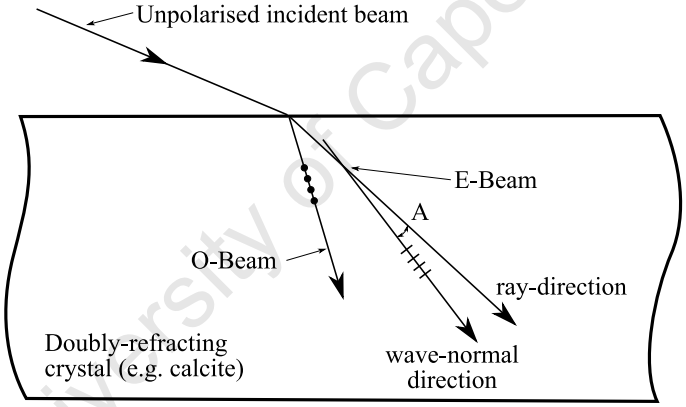

Figure 2.3: Diagram indicating the properties of a doubly-refracting crystal - in this case calcite with an optic axis in the plane of the paper. The diagram depicts: two refracted beams (the O- and E-beam) traveling in different directions; a slower O-beam (in the case of calcite); the orthogonal polarisation state of the two beams (dots and cross hatches); energy flow of the E-beam is oblique to the wave-normal direction (adapted from Shurcliff & Ballard, 1964).

In the case of calcite $n'_e \leq n_o$ and the crystal is called "negative", while for quartz $n'_e \geq n_o$ and it is called a "positive" crystal.

The optic axis of a crystal is defined as the axis where if the incident ray is normal to the

crystal surface, both O- and E-rays have the same normal speed and ray-directions. Calcite has only one such axis (uniaxial) while other crystals (including quartz) are generally biaxial (Clarke and Grainger, 1971).

When the vibrations of the E-ray are parallel to the crystal's optic axis, its normal speed takes its extreme value (minimum for calcite, maximum for quartz) and n'_e becomes the *minor principle refractive index* (n_e). The value $\Delta n = |n_e - n_o|$ is then defined as the *birefringence* (J) of the material. In the case of calcite its birefringence is large with $|n_e - n_o| = |1.486 - 1.659| = 0.172$ at 5790Å. For quartz the birefringence is less prominent with $|n_e - n_o| = |1.55170 - 1.54265| = 0.00905$ at 6330Å.

2.3 Polarisers

A polariser (or analyser) is an optical element used to discriminate between beams of differing polarisation states. Polarisers may use asymmetry of absorbtion, reflection, refraction or scattering to achieve this. The perfect polariser would force the emergent beam to be linearly polarised, regardless of the state of polarisation of the incident beam. The direction of vibration of the emergent beam is a property of the polariser and is referred to as the polariser's *axis*. Some polarisers allow both doubly-refracted beams to emerge and function as two polarisers operating at 90° to each other.

One of the most well-known such birefringent *polarising beam-splitters* is the *Rochon* prism, where two prisms of calcite or quartz are cemented together such that light entering the prism first travels parallel to the optic axis in the first prism, but perpendicular to the optic axis in the second. This causes the O-beam to be transmitted without deviation, while the E-beam is refracted at both crystal-crystal and crystal-air interfaces. A Rochon prism is illustrated in Figure 2.4, indicating the deviation of the E-beam for an all-calcite case (solid line) and an all-quartz case (dashed line).

The *Wollaston* prism, as is used in the SALT RSS, is a variation of the Rochon design such that the optic axes of both prism are selected to be parallel to the entrance/exit

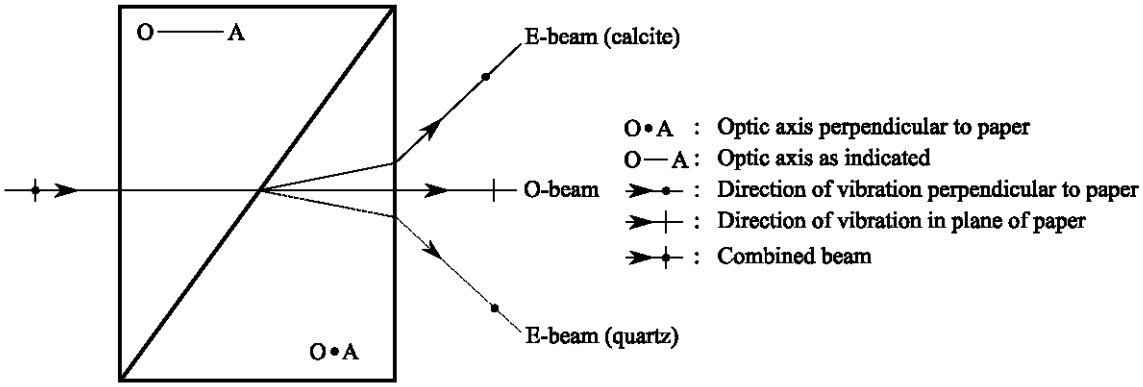

Figure 2.4: Rochon prism, adapted from Shurcliff & Ballard, 1964.

faces of the polariser (as shown for calcite in Figure 2.5). This causes both the O- and E-beam to be deviated in equal amounts, but in opposite sense, resulting in greater separation of the two beams than in the Rochon case. If the prism were constructed of quartz instead, the deviations would be as shown, but of lesser extent and with the E- and O-beam reversed.

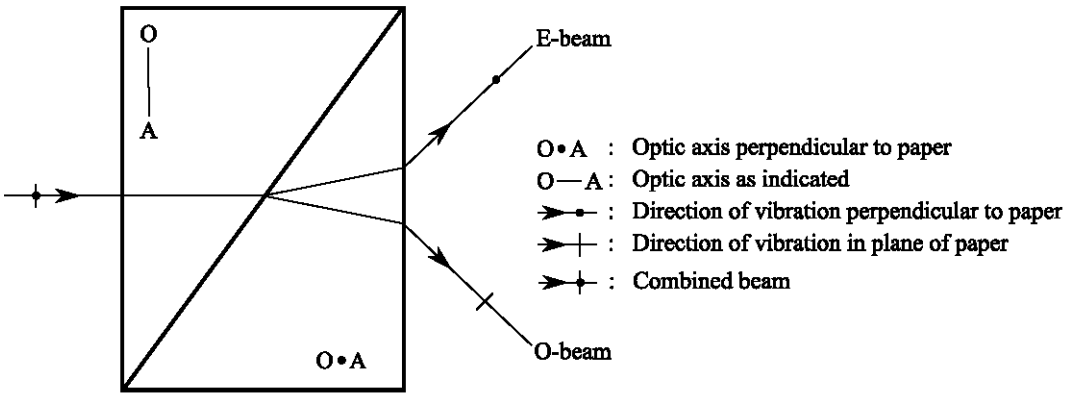

Figure 2.5: Wollaston prism (adapted from Shurcliff & Ballard, 1964).

2.4 Retarders

Retarders or wave plates are used to change the form of polarisation. Retarders function by shifting the phase of one (orthogonal) polarisation state of the incident beam relative to the other. Linear retarders (which resolve an incident beam into two linearly polarised components internal to the retarder) are typically constructed as a thin plate

of birefringent crystal with its optic axis parallel to the plane of the plate. If calcite is used, the plate then delays the O-beam relative to the E-beam (the *retardance*). In this case the direction of vibration of the O-beam (electric vector normal to the optic axis) is labeled the *slow* axis (S), with the E-beam's direction of vibration the *fast* (F) axis.

If the incident beam makes a small angle i with the normal to the retarder plate surface and the plane of incidence is at an angle ω with respect to the plate's optic axis, the retardance at wavelength λ is given by:

$$\tau \cong 2\pi(n_e - n_o)(s/\lambda)\left[1 - \frac{i^2}{2n_o}\left(\frac{\cos^2\omega}{n_o} - \frac{\sin^2\omega}{n_e}\right)\right], \tag{2.27}$$

with s the thickness of the retarder (Serkowski, 1974).

A half-wave plate retards the phase of the slow beam by 180° that results in "mirroring" the polarisation form around one of the axes of the retarder. For example a linearly polarised incident beam at 45° is converted to a beam with a linear polarisation angle of of −45°. Similarly a right-circularly polarised beam is converted to a left-circularly polarised beam while a right-elliptically polarised beam converts to a left-elliptically polarised beam with the major axis of the ellipse reflected around the fast (or slow) axis of the retarder.

Typically retarders are manufactured from crystals with a smaller birefringence than calcite, allowing the plate to be thicker for a given retardance.

In the case of a quarter-wave plate the retardance is 45° and thus it converts linearly polarised light into circularly polarised light and vice-versa if the linear polarisation direction is parallel to the retarder's fast or slow axis. Otherwise the translation is between linear and elliptical polarisation. Quarter-wave retarders need not be manufactured from birefringent material, as in the case of the Fresnel and Mooney rhomb where asymmetry in reflection is used.

Circular retarders can be manufactured where a crystal resolves the incident beam into two circularly polarised components (one left-handed and one right-handed) internal

to the crystal.

2.5 Polarimeters

A polarimeter is an instrument that combines one or more retarders and a polariser in the beam. This allows relative photometric measurements over a range of retarder angles to be used to determine some or all of the Stokes parameters of the incident beam. Two main types of polarimeters are found - those with and those without rapid modulation of the signal. Rapid modulation, as in a photo-polarimeter, is typically achieved by continuously rotating one or more of the optical elements of the retarder and helps to avoid measurement errors due to temporal effects such as atmospheric transparency and bad telescope guidance. Alternatively the elements are rotated or moved in discrete steps. With rapid modulation a continuous signal is recorded by the detector(s) - typically a photomultiplier tube (PMT), avalanche photo-diode (APD) or other photon-counting devices. The discrete case is suited for integrating area detectors, such as charged-coupled devices (CCDs), which allows for *imaging* polarimetry where the polarisation over an extended field can be determined. The efficiency of a polarimeter is defined as the fraction of incident intensity it transmits. For instance, if a polarimeter is constructed from a rotatable half-wave plate followed by a linear polariser, only half of the incident intensity is transmitted on average (Serkowski, 1974). If the linear polariser is replaced by a Wollaston prism and both exit beams are recorded the efficiency can approach 100% (ignoring attenuation losses). Such a configuration is depicted in Figure 2.6 and allows determination of linear polarisation. By adding a rotatable quarter-wave plate in front one can determine both linear and circular polarisation simultaneously. This configuration is shown in Figure 2.7 and is similar to that employed in the SALT RSS[1] and is known as "all-Stokes" mode, since it determines all four Stokes parameters.

[1]In the SALT RSS the quarter-wave and half-wave plates are reversed.

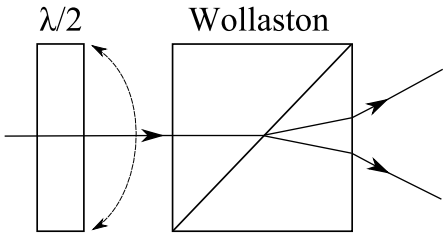

Figure 2.6: Linear polarimeter, adapted from Serkowski, 1974.

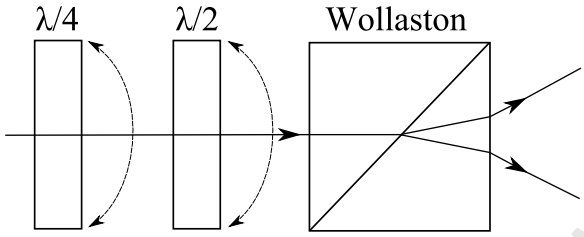

Figure 2.7: All-Stokes polarimeter, adapted from Serkowski, 1974.

2.6 Spectropolarimeters

A spectropolarimeter combines the capabilities of an imaging-polarimeter with that of a spectrograph. The degree of polarisation of the incident beam can therefore be determined as a function of wavelength. In the case of the SALT RSS this is achieved by introducing a grating in the collimated beam, between the retarder plates and the Wollaston prism assembly. The configuration is such that the grating disperses the beam perpendicularly to the displacement axis of the polariser, resulting in two spectra at the detector - one for the O-beam and one for the E-beam.

2.7 Obtaining the Stokes parameters

This section details the analysis performed to transform the extracted O- and E-beam spectra obtained from a discrete set of exposures into actual Stokes parameters and polarisation values. The basic case of linear polarimetry is discussed first and is then expanded to include circular and “all-Stokes” modes.

The methods discussed here are aimed at extracting the Stokes parameters from each

beam separately, as this is appropriate for the calibration purposes of this study (see Section 4.4). For a fully calibrated and characterised instrument, the polarisation parameters may be determined from both beams, requiring half the number of exposures in the waveplate sequence.

2.7.1 Linear polarimetry

From Table 2.1 the intensity transmitted through a perfect polariser with principal plane at angle θ is found to be:

$$\begin{aligned} I' &= \hat{i} \cdot \mathbf{P} \begin{bmatrix} I \\ Q \\ U \\ V \end{bmatrix} \\ I' &= \tfrac{1}{2}(I + Q\cos 2\theta + U \sin 2\theta), \end{aligned} \tag{2.28}$$

with $\mathbf{P}$ the Mueller matrix for a perfect polariser and $\hat{i}$ the unity vector $[\ 1 \quad 0 \quad 0 \quad 0\ ]$, isolating the intensity (I) component.

The combined transformation for a retarder with optic angle at ϕ followed by a polariser with principal plane at $\theta = 0°$ (upper signs, Wollaston O-beam) and $\theta = 90°$ (lower signs, Wollaston E-beam) then becomes:

$$\begin{aligned} I' &= \hat{i} \cdot \mathbf{PR} \begin{bmatrix} I \\ Q \\ U \\ V \end{bmatrix} \\ I' &= \tfrac{1}{2}\left[I \pm Q(G + H\cos 4\phi) \pm UH \sin 4\phi \mp V \sin\tau \sin 2\phi\right], \end{aligned} \tag{2.29}$$

with $\mathbf{R}$ the Mueller matrix of the retarder, $G = \frac{1}{2}(1 + \cos\tau)$ and $H = \frac{1}{2}(1 - \cos\tau)$ and τ the retardance of the waveplate.

From Eqn. 2.29 it is clear that the Q and U components cause an intensity variation in the transmitted beam related to four times the rotation angle of the waveplate. If the

i	ϕ_i	I'_i						
1	0	0.5I	+	0.5Q	+	0U	+	0V
2	45	0.5I	-	0.5Q	+	0U	+	0V
3	22.5	0.5I	+	0Q	+	0.5U	+	0V
4	67.5	0.5I	+	0Q	-	0.5U	+	0V
5	11.25	0.5I	+	0.354Q	+	0.354U	+	0V
6	56.25	0.5I	-	0.354Q	-	0.354U	+	0V
7	33.75	0.5I	-	0.354Q	+	0.354U	+	0V
8	78.75	0.5I	+	0.354Q	-	0.354U	+	0V

Table 2.2: Components of the O-beam intensity (I'_i) for a linear polarimetry waveplate pattern $\{\phi_i\}$, where ϕ is the angle of the half-wave plate and i the sample (exposure) number.

retarder is a half-wave plate $G = 0$, $H = 1$ and $\sin\tau = 0$ and the transmitted intensity as a function of waveplate angle becomes:

$$I' = \tfrac{1}{2}\left[I \pm Q\cos 4\phi \pm U\sin 4\phi\right]. \tag{2.30}$$

These two out-of-phase components can then easily be separated by taking exposures at appropriate waveplate angles to obtain the linear polarisation parameters. Table 2.2 indicates the contribution of each of the Stokes parameters to the intensities $\{I'_i\}$ of the $\theta = 0°$ (O-) beam of the polariser, given the waveplate angle sequence $\{\phi_i\}$.

The components I, Q and U of the incident beam can then be reconstructed from these eight intensities $\{I'_i\}$ as follows:

$$I = \tfrac{1}{4}\sum_{i=1}^{8} I'_i \tag{2.31}$$

$$Q = \tfrac{1}{2}\sum_{i=1}^{8} \cos 4\phi_i I'_i \tag{2.32}$$

$$U = \tfrac{1}{2}\sum_{i=1}^{8} \sin 4\phi_i I'_i \tag{2.33}$$

From Table 2.2, it is clear that this sequence contains redundant information that may

be useful for characterising systematic errors, but can be omitted if a shorter exposure sequence is desired (i.e. using the first four exposures $i = 1..4$ only).

The amount of linear polarisation P_L and position angle of this polarisation may be determined from Q and U as follows (Landi Degl'Innocenti, Bagnulo and Fossati, 2007):

$$\begin{aligned} P_L &= \sqrt{Q^2 + U^2}, and \\ PA &= \tfrac{1}{2} sign(U) \arccos\left(\frac{Q}{\sqrt{Q^2 + U^2}}\right) \end{aligned} \tag{2.34}$$

2.7.2 Circular polarimetry

Adding a second retarder to the optical train to create an all-Stokes capable polarimeter results in the following transform:

$$I' = \hat{i} \cdot \mathbf{PR_2R_1} \begin{bmatrix} I \\ Q \\ U \\ V \end{bmatrix}$$

$$\begin{aligned} I' = \tfrac{1}{2}\{ & I \pm Q[G_1G_2 + H_1H_2 \cos 4(\phi_1 - \phi_2) + H_1G_2 \cos 4\phi_1 + G_1H_2 \cos 4\phi_2 \\ & - \sin\tau_1 \sin\tau_2 \sin 2\phi_1 \sin 2\phi_2] \\ & \pm U[H_1H_2 \sin 4(\phi_1 - \phi_2) + H_1G_2 \sin 4\phi_1 + G_1H_2 \sin 4\phi_2 \\ & + \sin\tau_1 \sin\tau_2 \cos 2\phi_1 \sin 2\phi_2] \\ & \mp V[H_2 \sin\tau_1 \sin(2\phi_1 - 4\phi_2) + G_2 \sin\tau_1 \sin 2\phi_1 \\ & + \cos\tau_1 \sin\tau_2 \sin 2\phi_2], \end{aligned} \tag{2.35}$$

with ϕ_1, τ_1, ϕ_2, τ_2 the angle and retardance of retarders R_1 and R_2, respectively.

From Eqn. 2.35 it is clear that Q, U and V components are modulated at 2 and 4 times the waveplate angles as well as the same multiples of the difference in angle between the waveplates. Table 2.3 shows a waveplate pattern that exploits this relationship to extract the circular polarisation component, V.

i	ϕ_{1_i}	ϕ_{2_i}	I'_i						
1	0	+45	0.5I	+	0Q	+	0U	+	0.5V
2	0	-45	0.5I	+	0Q	+	0U	-	0.5V
3	22.5	-45	0.5I	+	0Q	+	0U	-	0.5V
4	22.5	+45	0.5I	+	0Q	+	0U	+	0.5V
5	45	+45	0.5I	+	0Q	+	0U	+	0.5V
6	45	-45	0.5I	+	0Q	+	0U	-	0.5V
7	67.5	-45	0.5I	+	0Q	+	0U	-	0.5V
8	67.5	+45	0.5I	+	0Q	+	0U	+	0.5V

Table 2.3: Components of the O-beam intensity (I'_i) for a circular polarimetry wave-plate pattern $\{\phi_{1_i}, \phi_{2_i}\}$, with ϕ_1 and ϕ_2 the angles of the half- and quarter-wave plate, respectively.

In this case the intensity I is determined as before, while V is simply calculated from:

$$V = \tfrac{1}{4} \sum_{i=1}^{8} \sin 2\phi_{2_i} I'_i \tag{2.36}$$

Using a combination of exposures at different half-wave plate angles allows any circular-to-linear polarisation conversion inherent to the half-wave plate to be canceled.

2.7.3 All-Stokes polarimetry

Nordsieck et al. 2003 propose an all-Stokes waveplate pattern where the half-wave plate angle (ϕ_1) is advanced in 22.5° steps, while the quarter-wave plate angle (ϕ_2) is advanced in steps $\frac{3}{2}$ times this amount. Table 2.4 numerically indicates the relative intensities of the four Stokes parameters (for the O-beam) given this waveplate pattern.

When attempting to isolate I, Q, U and V from the above exposures, it becomes clear that while the 3 : 2 ratio between ϕ_2 and ϕ_1 steps is appropriate when applied to the signal from continuously rotating waveplates, the discrete sampling applied in Table 2.4

i	ϕ_{1_i}	ϕ_{2_i}	I'_i							
1	0	0	0.5I	+	1Q	+	0U	+	0V
2	22.5	33.75	0.5I	+	0.354Q	+	0.146U	+	0.924V
3	45	67.5	0.5I	-	0.5Q	-	0.5U	+	0.707V
4	67.5	101.25	0.5I	-	0.354Q	-	0.854U	-	0.383V
5	90	135	0.5I	+	0Q	+	0U	-	1V
6	112.5	168.75	0.5I	-	0.354Q	+	0.854U	-	0.383V
7	135	202.5	0.5I	-	0.5Q	+	0.5U	+	0.707V
8	157.5	236.25	0.5I	+	0.354Q	-	0.146U	+	0.924V

Table 2.4: Components of the O-beam intensity (I'_i) for an all-Stokes polarimetry waveplate pattern $\{\phi_{1_i}, \phi_{2_i}\}$ with ϕ_1 step size of 22.5°.

causes residual contamination to remain between I, Q and V and only the U term can be fully isolated. For example:

$$Q \approx 2\left[\sum_{i=1}^{8}\cos 4\phi_{1i}I'_i + \sum_{i=1}^{8}\cos 2\phi_{1i}I'_i\right] = 0I + 1Q + 0U + 0.108V \quad (2.37)$$

$$U = 2\left[\sum_{i=1}^{8}\sin 4\phi_{1i}I'_i - \sum_{i=1}^{8}\sin 2\phi_{1i}I'_i\right] = 0I + 0Q + 1U + 0V \quad (2.38)$$

$$V \approx 2\sum_{i=1}^{8}\sin 3\phi_{1i}I'_i = 0.187I + 0.054Q + 0U + 1V \quad (2.39)$$

and there is no clear way to determine I.

The author therefore proposes a new waveplate pattern for use in all-Stokes polarimetry with RSS where the ratio in step size of the waveplate angles remains 3 : 2, but the step size of the half-wave plate is doubled to 45°. This pattern is shown in Table 2.5.

i	ϕ_{1_i}	ϕ_{2_i}	I'_i							
1	0	0	0.5I	+	1Q	+	0U	+	0V
2	45	67.5	0.5I	-	0.5Q	-	0.5U	+	0.707V
3	90	135	0.5I	+	0Q	+	0U	-	1V
4	135	202.5	0.5I	-	0.5Q	+	0.5U	+	0.707V
5	180	270	0.5I	+	1Q	+	0U	+	0V
6	225	337.5	0.5I	-	0.5Q	-	0.5U	-	0.707V
7	270	45	0.5I	+	0Q	+	0U	+	1V
8	315	112	0.5I	-	0.5Q	+	0.5U	-	0.707V

Table 2.5: Components of the O-beam intensity (I'_i) for an all-Stokes polarimetry waveplate pattern $\{\phi_{1_i}, \phi_{2_i}\}$. with ϕ_1 step size of 45°.

The individual Stokes parameters can then be reconstructed from:

$$I = \frac{1}{4}\sum_{i=1}^{8} I_i \tag{2.40}$$

$$Q = \frac{1}{2}\sum_{i=1}^{8} \cos 4\phi_{1_i} I'_i \tag{2.41}$$

$$U = -\sum_{i=1}^{8} \sin 2\phi_{1_i} I'_i \tag{2.42}$$

$$V = \frac{1}{2}\sum_{i=1}^{8} \sin 3\phi_{1_i} I'_i \tag{2.43}$$

This section has listed methods for determining polarisation parameters from a number of individual exposures, each taken at a different step of a waveplate sequence. The reader may notice that all parameters are determined from one beam of the polariser only (the $\theta = 0°$, or O-beam). The shortcomings in the treatment so far are that no consideration is made for noise inherent in the signal and furthermore assumes perfect optics - specifically the polariser. Extending the analysis to optimise the signal-to-noise while compensating for varying efficiency of the system from one exposure to the next is detailed in Section 4.4.

Chapter 3

SALT and the RSS instrument

3.1 Characteristics of the SALT

The Southern African Large Telescope (SALT) is a 10-metre class optical telescope situated at the South African Astronomical Observatory's facility near Sutherland in the Northern Cape Province. The optical design, based on the Hobby Eberly Telescope (HET) in Texas, consists of a segmented, spherical primary mirror combined with a four-mirror spherical aberration corrector (SAC) that delivers a corrected flat focal plane ~160mm (10 arc minutes) in diameter to one of four instrument ports (O'Donoghue, 2000). The design is such that the elevation-angle of the primary remains fixed at 37° from the vertical and can be pointed in azimuth only (Figure 3.1). This results in a fixed gravity vector on the primary, greatly reducing the weight, cost and complexity of the main telescope support structures (Stobie, Meiring and Buckley, 2000; Buckley et al., 2003; Buckley et al., 2004).

The trade-off of this approach is that the telescope needs to follow astronomical objects using an Arecibo-style moving payload at the prime focus that traverses the focal sphere of the primary during an observation. This is achieved by a tracker system mounted at the top of the telescope structure, providing precision motion in six degrees of freedom

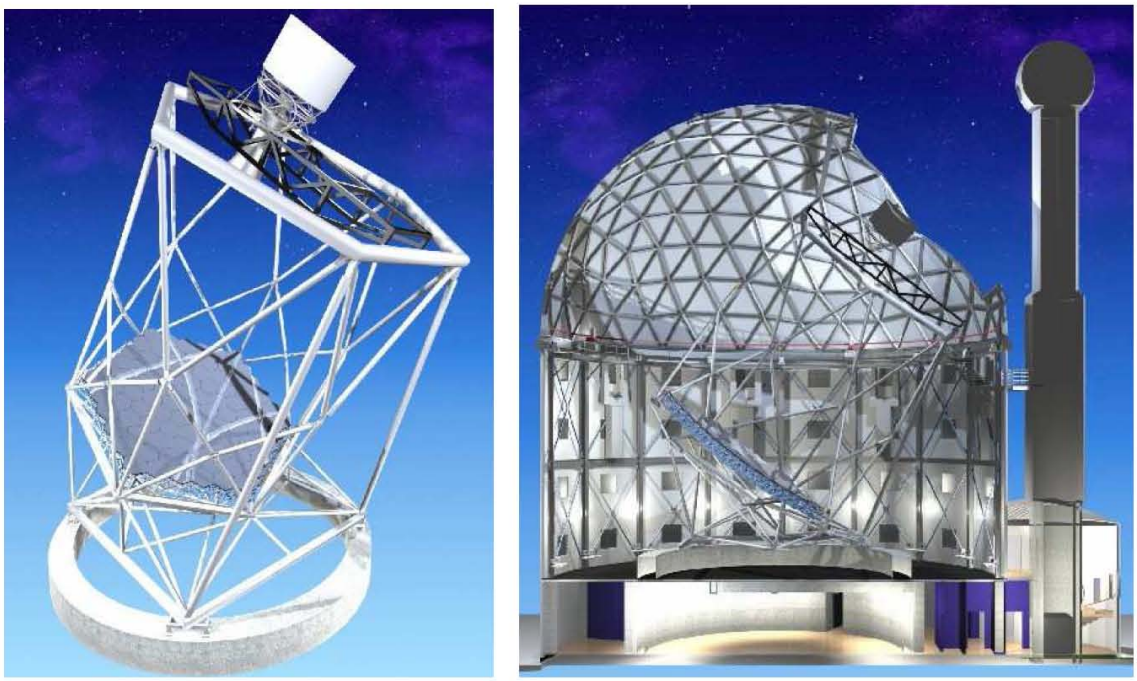

Figure 3.1: Three dimensional model views of the SALT indicating the fixed elevation of the primary mirror, the concrete pier that allows azimuth rotation and the instrument payload supported by the tracker at the top of the telescope structure. At right, the centre-of-curvature alignment tower is shown next to the main telescope building.

of the SALT payload and SAC, which allows an object to be followed for 12 degrees on the sky while the primary mirror is kept stationary.

The SALT payload houses two first-light prime-focus science instruments - an acquisition and science imager called SALTICAM (O'Donoghue et al., 2003) as well as the Robert Stobie Spectrograph (RSS) (Nordsieck et al., 2001). SALTICAM provides traditional imaging modes such as full-frame imaging for extended objects, but also more advanced modes of operation such as frame-transfer and slot-mode imaging, supporting exposure times down to 100ms, allowing fast photometry of faint objects when combined with SALTs large collecting area (O'Donoghue et al., 2003). RSS is a multi-purpose instrument providing many modes of operation including low to medium-resolution spectroscopy of single or multiple sources in the field of view, Fabry-Perot imaging as well as imaging- and spectro-polarimetry (Burgh et al., 2003). The third payload instrument port is designated to house the Fibre Instrument Feed (FIF) that

allows light to be fed to the SALT High Resolution Spectrograph (HRS), currently under construction (Barnes et al., 2003). Finally an auxiliary port is provided in the payload for small visitor instruments to the SALT.

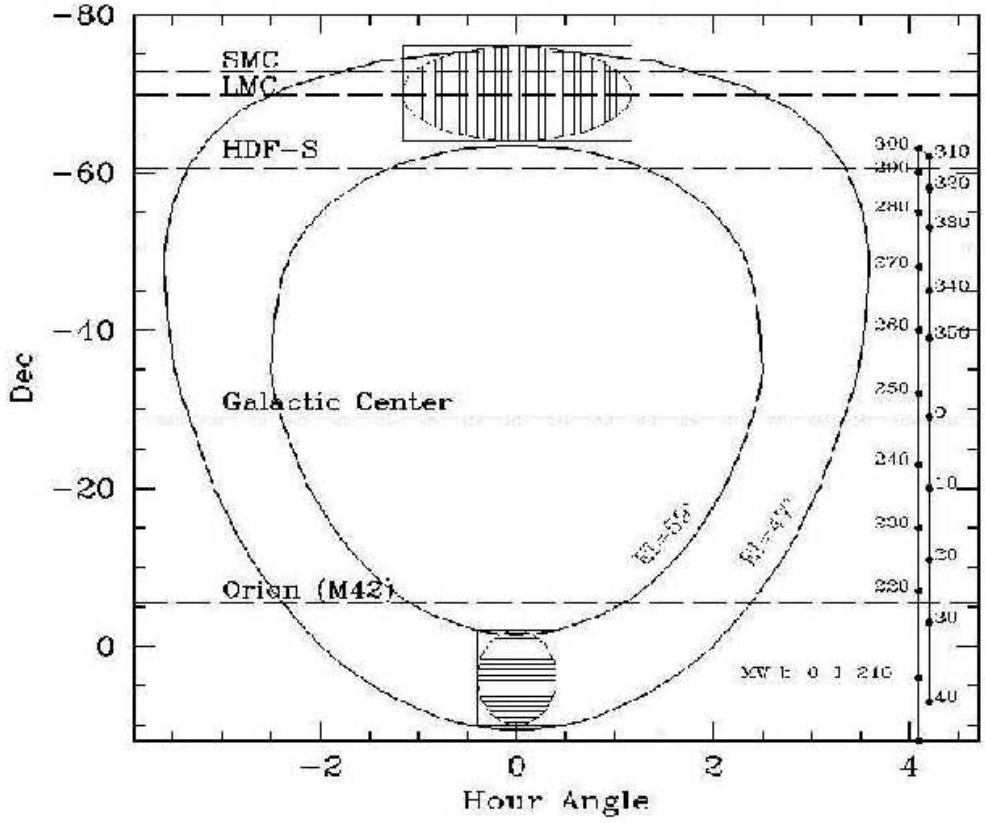

Figure 3.2: The SALT's visibility envelope, indicating the annulus in declination versus hour angle space that SALT can access at any particular moment - by moving the tracker between its elevation extremes (EL=47° and EL=59°) and rotating the telescope structure in azimuth. The vertical lines on the right indicate the declination range of the Galactic plane for differing Galactic longitude. The declinations of some well-known astronomical targets including the Large and Small Magellanic Clouds (LMC, SMC) and the Hubble-Deep-Field South (HDF S) are shown for reference.

The SALT design limits access to targets located within an annulus on the sky 12-degrees wide and centered around 37° from the zenith. As seen in Figure 3.2, the maximum duration an object can be followed on sky depends on its declination angle and ranges from almost six hours in the South (Declination -67°) to around 40-minutes for objects lying due West or East (Declination -30°). Figure 3.2 also shows that

most objects are visible at two intervals during the night - an "East track" as the object rises followed by a "West track" later in the night. This annular "visibility window", which is approximately 12.5% of the available sky, allows SALT to observe 70 percent of the night sky visible from Sutherland throughout the year, but implies strict windows of opportunity for any specific object. Therefore, in order to make optimal use of telescope time, SALT needs to be operated in a queue-scheduled fashion where the targets for a night can be selected from a pool of proposed observations. An additional caveat of tracking the payload across the focal sphere is that the effective size of the entrance pupil (footprint on the primary mirror visible by the SAC and instruments) varies with tracker location (Figure 3.3). This implies that the intensity for any target recorded at the focal plane varies as a function of tracker payload position (time) during an observation. Generation of calibration flat field frames are therefore required via a calibration source that mimics the changes in pupil observed during the science exposures.

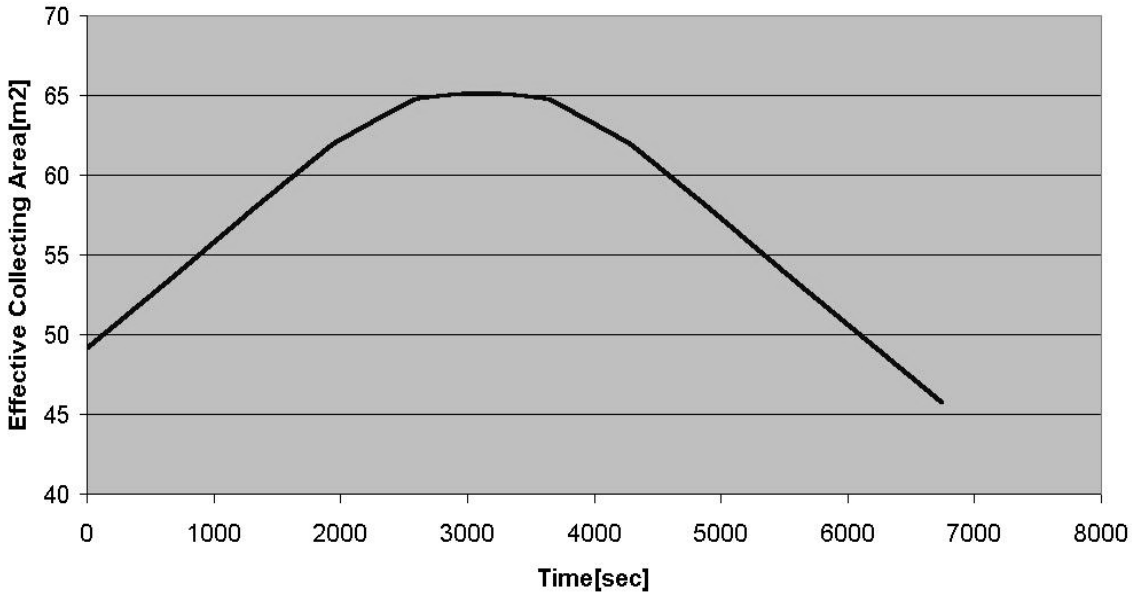

Figure 3.3: Varying effective pupil size for an arbitrary track as a function of time, with the telescope structure pointing South.

3.2 RSS

The Prime Focus Imaging Spectrograph (PFIS) (Buckley et al., 2003; Burgh et al., 2003; Kobulnicky et al., 2003; Nordsieck et al., 2003) is a highly versatile workhorse first-generation instrument of the SALT. The instrument was renamed the Robert Stobie Spectrograph (RSS) in honour of the late director of the South African Astronomical Observatory in 2002.

The instrument resides at the f/4.2 prime focus of the SALT and exploits this by providing operational modes such as multi-object spectroscopy and Fabry-Perot imaging spectroscopy over the full science field of view. RSS-VIS (a UV-visible instrument) employs a high UV-transmitting optical design to support UV spectroscopy down to the atmospheric cutoff at 320nm (rare on large telescopes)[1]. The RSS-VIS detector is comprised of a linear mosaic of three 4096×2048 E2V CCDs. The dispersive elements in RSS-VIS include a suite of five volume-phase-holographic (VPH) gratings, a standard 300 l/mm transmission grating as well as a double etalon Fabry-Perot system. Additionally RSS includes polarimetric optics allowing the instrument to support both imaging- and spectro-polarimetric modes for all the above configurations. The RSS-VIS has a wavelength coverage from 320nm to 900nm, while a near-infrared spectrometer (RSS-NIR), allowing simultaneous coverage from 850nm to 1.7μm is currently under construction. These two instruments will operate in parallel, allowing potentially simultaneous visible to near-infrared coverage. The optical layout of RSS-VIS is shown in Figure 3.4.

3.2.1 RSS polarimetric modes

RSS is capable of linear, circular and all-stokes polarimetry depending on the wave-plates used. The polarimetric module can be used in parallel with all other RSS modes, enabling imaging-polarimetry (where no dispersive elements are used), spectro-

[1] another example is X-shooter on the VLT (D'Odorico et al., 2006)

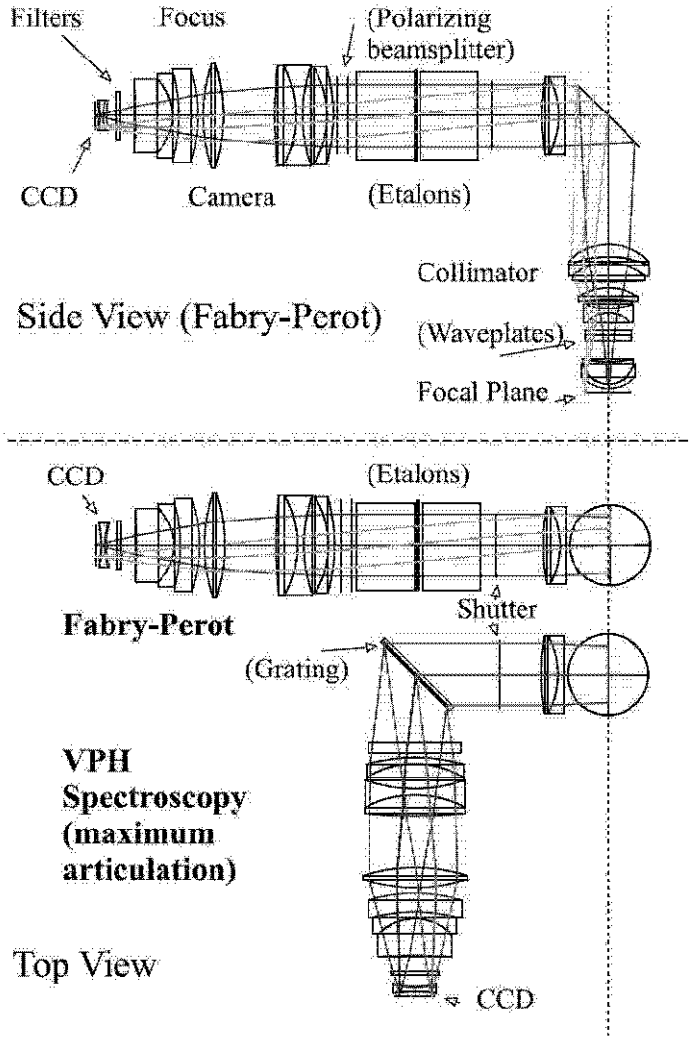

Figure 3.4: RSS-VIS optical layout showing the straight-through (imaging) configuration with the double-etalon system employed for Fabry-Perot mode (upper) as well as the articulated configuration including the VPH grating used for spectroscopy (lower). The locations of the waveplates and polarising beam splitter are shown in the side-view (upper). These are used in conjunction with the grating to allow spectro-polarimetry modes, from Nordsieck et al. (2003).

polarimetry (where a transmission grating is inserted and the camera articulated) and also a unique Fabry-Perot-polarimetry mode (where etalons are inserted to act as a tunable scanning bandpass filter).

In linear polarimetry mode only the half-wave plate is used (a quarter-wave plate

blank is inserted to maintain focus compatibility) and is rotated between exposures in a standard sequence resulting in exposure pairs separated in phase by 90° at the detector (waveplate is rotated by 45°).

In circular polarimetry mode both waveplates are used. Exposures are taken with the quarter-wave plate at angles of +45° and −45°, while the half-wave plate is advanced by 22.5° between exposures. These two quarter-wave plate positions convert circular to linear polarisation that is aligned with and orthogonal to the polariser principal axis, respectively. Rotation of the half-wave plate is used to rotate the axis of any incident linear polarisation to different angles so that this component cancels out during reduction.

In all-Stokes mode both waveplates are advanced, but with differing steps, resulting in linear an circular polarisation contributing to the intensity of the resulting image at different frequency multiples of the rotation rate. By convolving the resulting signal with sines and cosines of the appropriate frequencies both components may be extracted (Serkowski, 1974).

As mentioned above, the polarimeter module may be used without any dispersive elements in the beam. The beam divergence of the polarising beamsplitter is wavelength dependent, however, being more pronounced at the blue end. The wavelength dependence is clearly illustrated by the curvature of the spectra (taken in spectro-polarimetric mode) shown in the RSS CCD image of Figure 3.5. In imaging-polarimetry mode, this results in a low-resolution spectrum (of orthogonal dispersion sense for E- and O-beam and perpendicular to the grating dispersion axis) at the detector for each point source. This mode is therefore suitable for low-resolution multi-object sprectro-polarimetry rather than imaging-polarimetry of extended objects.

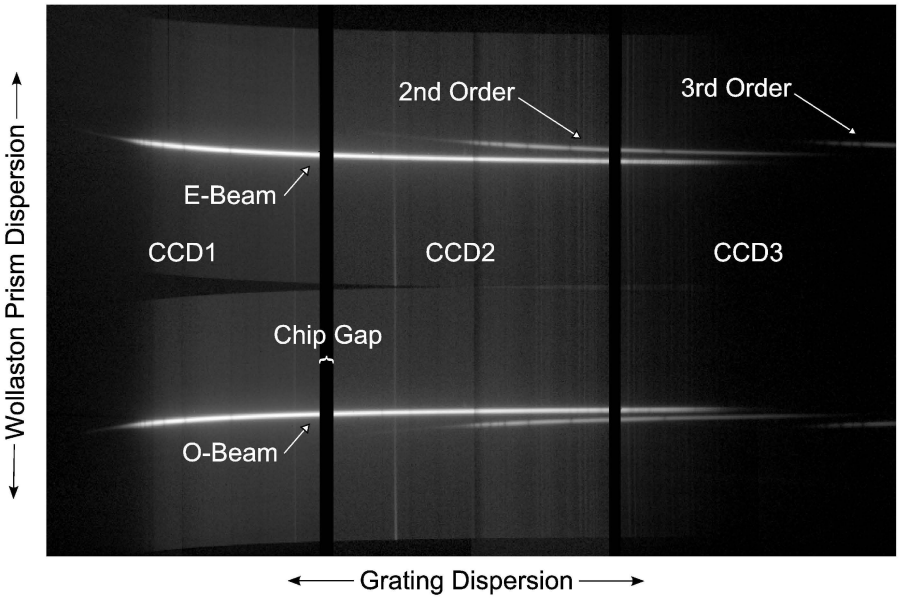

Figure 3.5: An RSS image taken in spectro-polarimetric mode with the 300 l/mm grating clearly shows the wavelength dependence of the beamsplitter dispersion on the O- and E-beam spectra. The beamsplitter dispersion is in the vertical (column) direction and grating dispersion is in the horizontal (row) direction. The three CCD chips comprising the RSS detector can also be seen, with gaps between them. Higher-order spectra are present on the second and third CCDs.

3.2.2 RSS polarimeter design

The RSS polarimetric module consists of a rotatable half- and quarter-wave plate inserted into the diverging beam within the collimator, just after the focal plane, followed by an array of Wollaston beamsplitters in the collimated space in front of the visible-beam camera (Nordsieck et al., 2003). The half- and/or quarter-wave plate may be inserted into the beam depending on the polarimeter mode.

The waveplates shown in Figure 3.7 are of *Pancharatnam superachromatic* design. A single birefringent plate acts as a half- (or quarter-) wave plate only at a single wavelength, since its birefringence is a function of wavelength (see Section 2.27). A conventional achromatic (wide-band) retarder can be constructed by combining two retarders manufactured from different materials, such that it exhibits a specific retardance at

two wavelengths. In the Pancharatnam design (Pancharatnam, 1955) a central plate is surrounded by a pair of identical waveplates, rotated by some angle. This arrangement can also be adjusted to produce a specific combined retardance at two wavelengths. By combining these two techniques a so-called Pancharatnam superachromatic waveplate can be constructed with good broadband performance. In RSS each Pancharatnam element is constructed as an achromatic pair constructed from magnesium fluoride and crystal quartz. The half-wave plate is 100 mm in diameter and provides a full 8×4 arc-minute polarimetric field used for linear polarimetry, while the quarter-wave plate is only 60 mm in diamter and covers a 3.9×4 arc-minute field available for circular and all-Stokes polarimetry modes.

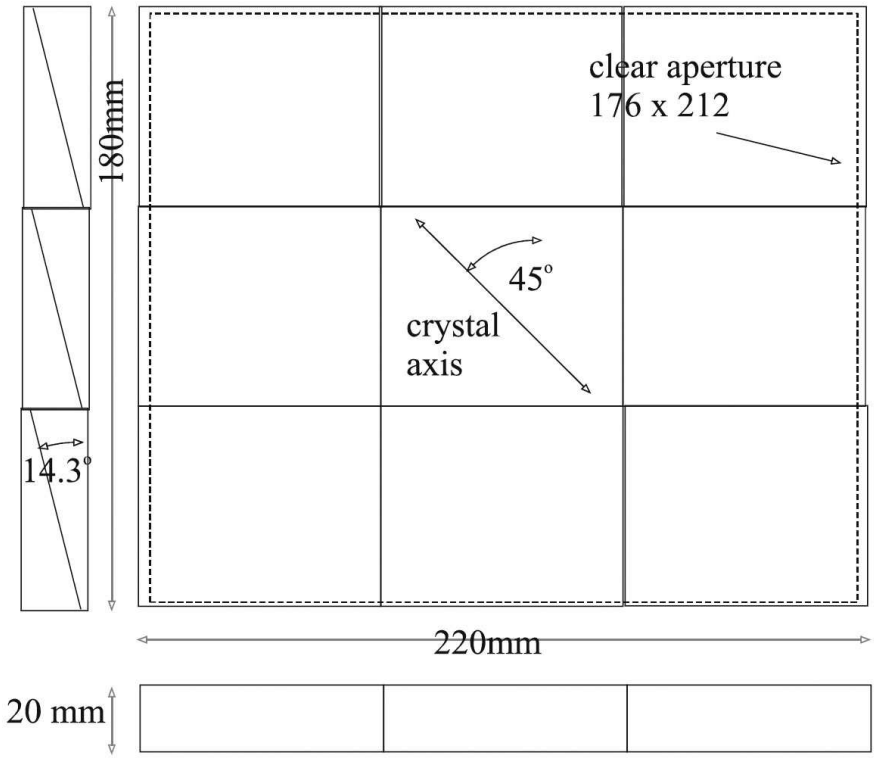

Figure 3.6: RSS polarising beamsplitter design, from Nordsieck et al. (2003). The final construction placed the crystal axis at 90°

The polariser used in RSS comprises a 3×3 mosaic of calcite Wollaston beam-splitters shown in Figure 3.8 providing a clear aperture of 176×212 mm. A mosaic is used to provide the required large aperture while retaining a physically thin polariser design.

Figure 3.7: The RSS half-wave plate (left) and quarter-wave plate (right).

The polariser splits the beam in a direction orthogonal to the dispersion axis delivering completely separated E- and O-beam images at the detector, each covering an 8×4 arc-minute field. The prisms' optic axis was originally chosen to be at a 45° angle to the dispersion axis to mitigate against throughput differences between the E- and O-beam caused by the grating (Figure 3.6). The final design was, however, changed to place the optic axis at 90° - orthogonal to the depolarisation axis of the RSS fold-mirror, which has a complex dielectric coating resulting in varying phase changes between the O and E beams. As a result the throughput of the E-beam for RSS is more efficient than that of the O-beam, especially at high dispersion angles. An example of the two separated E- and O-beam images delivered by the beamsplitter can be seen in Figure 3.5, where the two polarisation state images are vertically separated while the grating dispersion axis is in the horizontal direction.

Telescope instrumental polarisation is a concern for RSS polarimetry with reflections off the SALT primary and SAC mirrors with relatively large incidence angles (up to ∼20°) which additionally vary during a track. Modeling of the telescope's effect on polarisation, assuming a pure aluminium coating on the primary and Lawrence Livermore National Laboratory (LLNL) multi-layer coatings on all four SAC mirrors, indicate expected linear polarisation of up-to $\sim 0.2\%$ at blue wavelengths and at a field angle of four arc-minutes (Nordsieck et al., 2003). Curves indicating the expected polarisa-

Figure 3.8: Mosaic of Wollaston prims forming the RSS polarising beamsplitter.

tion as a function of wavelength for a number of different field and track angles are shown in Figure 3.9. Dielectric coatings on the SAC (and RSS fold) mirrors influence the polarisation properties of the reflected light due to the nature of reflection at a dielectric-metal boundary, which causes a phase change that is dependent on the wavelength and incidence angle (Hass, 1965).

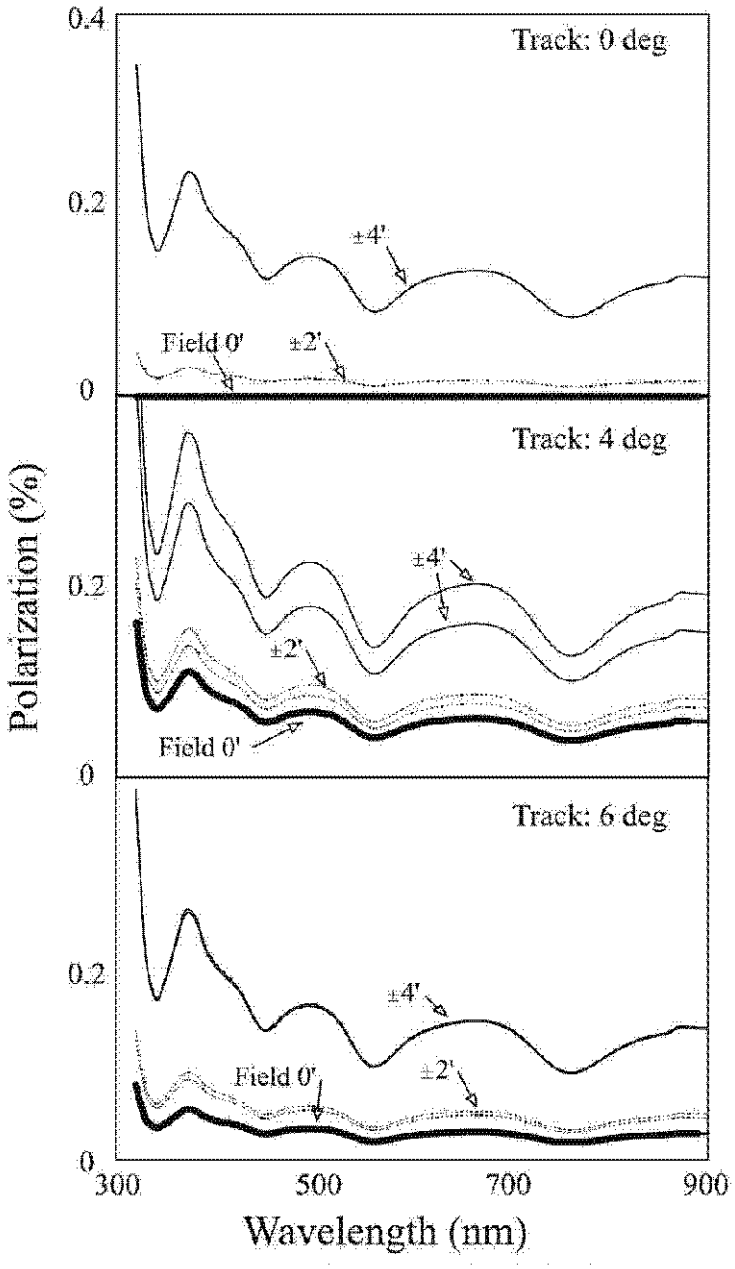

Figure 3.9: Expected SALT instrumental polarisation, from Nordsieck et al. (2003). The top panel indicates polarisation expected with the telescope tracker located on-axis over the centre of the primary mirror. The middle panel indicates larger amounts of expected polarisation arising from light reflecting at more oblique angles when the tracker is at four degrees from the telescope optical axis. Finally the bottom panel indicates the extreme case with the tracker six degrees off-axis.

Chapter 4

Processing and analysis of RSS data

This section details the techniques used to prepare raw RSS data for analysis, how the spectra were extracted from the two-dimensional images and finally the detailed method used for analysing these spectra to determine the polarisation parameters of a target.

4.1 Recording the data

As mentioned in Section 3.2, RSS-VIS employs a charge-coupled-device (CCD) detector at the visible camera focal plane. CCDs are versatile high-efficiency area detectors often used in astronomical instruments (see e.g. McLean, 2008). Fundamentally CCDs employ a variant of the photo-electric effect where electrons are knocked from the valence levels and into the conduction band of a semiconductor by incident photons, thereby converting photons into electron-hole pairs, which are separated by a potential difference applied across a P-N junction (Janesick, 2001). In a CCD each picture element or *pixel* is a capacitor that acts as a trap for such freed electrons as long as a positive potential is applied to it. While light falls on the detector each pixel collects electrons proportional to the number of photons absorbed, thus recording the image scene electrically. Following exposure to light, applying a sequence of potential changes

to adjacent pixels in a column the charge from each pixel can be shifted to the next, allowing the charge in each column to be shifted to the edge of the array from where it is shifted into a readout register. During readout the tiny charge for each pixel is amplified and finally digitized.

Sources of noise in CCDs therefore include variations in the charge transfer efficiency (indicating the fraction of electrons transferred successfully from one pixel to the next), Poisson (counting) noise related to any bias level charge, reset noise (noise incurred when re-charging the readout register as each pixel's charge is shifted into it) and amplifier noise. Collectively these sources contribute to the noise of the device.

While CCDs exhibit a very linear response to the incident light intensity, eventually no more electrons can be captured by the pixel's capacitor. This amount is defined as the full-well capacity of the detector and indicates the saturation level (in electrons) of the detector.

The amplification factor of the readout amplifier, or gain, needs to be chosen such that digitization by the analogue-to-digital converter (ADC) is sensitive enough to detect small numbers of photons and convert this into a digital '1', while at the same time ensuring that the full-well charge of the detector can be digitized within the available bit-depth of the ADC. For instance, an 16-bit ADC can represent an analogue input value by a number from 0 to 65535, representing 65536 levels, or analogue-to-digital units (ADUs). If the full-well capacity of the detector is 100000 electrons, then the amplifier gain can be set no higher than $100000/65536 = 1.53$ electrons per ADU, if the ADC is not to become the limiting factor for saturation. A choice of gain and readout-speed are allowed, depending on the object brightness and integration time, to optimise the resulting signal-to-noise for a specific exposure.

These concepts of amplifier gain and detector noise are used below to define the error propagation techniques used during the reduction process.

4.2 Preparing the data

The data were prepared using existing PyRAF[1] SALT pipeline reduction software, including NOAO IRAF tools[2]. Additional PyRAF software was developed to enable error propagation using Data Quality (DQ) and error (variance) planes. The DQ plane represents a bit-map mask, indicating which of the science data elements (image pixels or spectrum values) are regarded as valid. This allowed masking of cosmic rays, bad pixels and other detector defects in the data. The error plane represents a "noise" plane reflecting the equivalent noise level at each pixel location (of a 2-dimensional image) or wavelength index (of a one-dimensional spectrum). The variance at each location was estimated as the sum of a photon noise and a readout noise component:

$$\sigma^2 = C \cdot g + (R \cdot g)^2, \tag{4.1}$$

with C representing the signal count at the CCD location (in ADU), R the readout noise of the amplifier (in ADU) and g its gain (in electrons per ADU).

The raw data were therefore augmented by these two meta-data planes and subsequently prepared according to standard SALT pipeline reduction steps. Data from each of six CCD readout channels were de-biased using counts from the CCD overscan regions, gain corrected according to the specific amplifier gain and pre-binning selection, cross-talk between amplifiers was removed and finally mosaiced into a single image.

Science and variance planes were then processed to remove cosmic-ray artifacts via median filtering - either based on surrounding pixels or, if multiple similar frames were available (for instance in the case of a polarimetry sequence) based on the median across the image set.

[1]PyRAF is part of the `stsci_python` package of astronomical data analysis tools, and is a product of the Science Software Branch at the Space Telescope Science Institute. Copyright © 2005 Association of Universities for Research in Astronomy (AURA).

[2]IRAF is distributed by the National Optical Astronomy Observatory, which is operated by the Association of Universities for Research in Astronomy (AURA) under cooperative agreement with the National Science Foundation.

While flat-fielding may be appropriate in some cases, this was generally not available for the commissioning data used in this study and was not deemed to significantly impact the reduction of differential data sets, such as those used in polarimetry of bright objects.

4.3 Extracting the spectra

Once prepared, the NOAO IRAF `twodspec.longslit.identify` task was used to wavelength-calibrate the data frames based on spectral lines of known wavelength identified in a calibration arc lamp frame taken prior to or following the science sequence. Mapping of pixels to wavelength was achieved using a best-fit polynomial (typically 3rd order) to the arc line positions. Typically the root mean square (RMS) error of the fit for PG0300 (300 l/mm) grating data was ∼13 Å (based on a HgAr arc lamp features), while PG0900 (900 l/mm) grating data were fit to an RMS error of ∼3 Å (using a Neon arc lamp)[3]. This mapping was repeated for a number of rows across the image, thus producing a two-dimensional map used to transform the science frames (using the NOAO `twodspec.transform` task) to ensure one image dimension was aligned with the dispersion direction while the other was perpendicular to it. Data counts in the latter dimension could then be safely "binned" or summed to improve the signal to noise of the extracted spectrum without introducing blending of data from different wavelengths. This process is especially pertinent to the curved spectra produced by VPH gratings and the calcite beamsplitter as used in RSS-VIS for spectropolarimetry.

A software aperture was then defined (using the NOAO `twodspec.apextract.apall` task) on the wavelength-calibrated frame for the O- and E-beam spectrum at a specific wavelength. In cases where telescope guidance was good (little or no drift of the spectra in the "spatial" direction was present between subsequent exposures) it was appropriate

[3]While these wavelength calibration errors are admittedly large and improved identification of emission lines need to be performed for future observations, they do not materially affect the results discussed in Chapter 5

to define the apertures on a combined image, created from the mean of all exposures in the waveplate sequence (using the `imcombine` task). This allowed using constant apertures for all exposures, limiting detector related variations during the extraction process. Alternatively, in the case of poor guiding, the two apertures were defined on one frame and allowed to shift as a unit in the "spatial" direction when re-centering to the spectra of each exposure, while keeping all other parameters of the apertures constant. The apertures were selected to exclude higher-order spectra while including the maximum amount of signal. For each aperture a background region was also defined to be used for background-subtraction during extraction. Again care needed to be taken to avoid higher order spectra from contaminating this region. A background region was therefore defined on only one (the "inner", i.e. between the two O and E beam spectra) side of each target spectrum, avoiding image rows peripheral to the pair of target spectra apertures where the higher order spectra lie. Such higher order spectra were especially prominent in the PG0300 surface relief grating data at wavelengths longer than 7000Å, as indicated in Figure 4.1 where O- and E-beam apertures for HD14069 at 8000Å are shown.

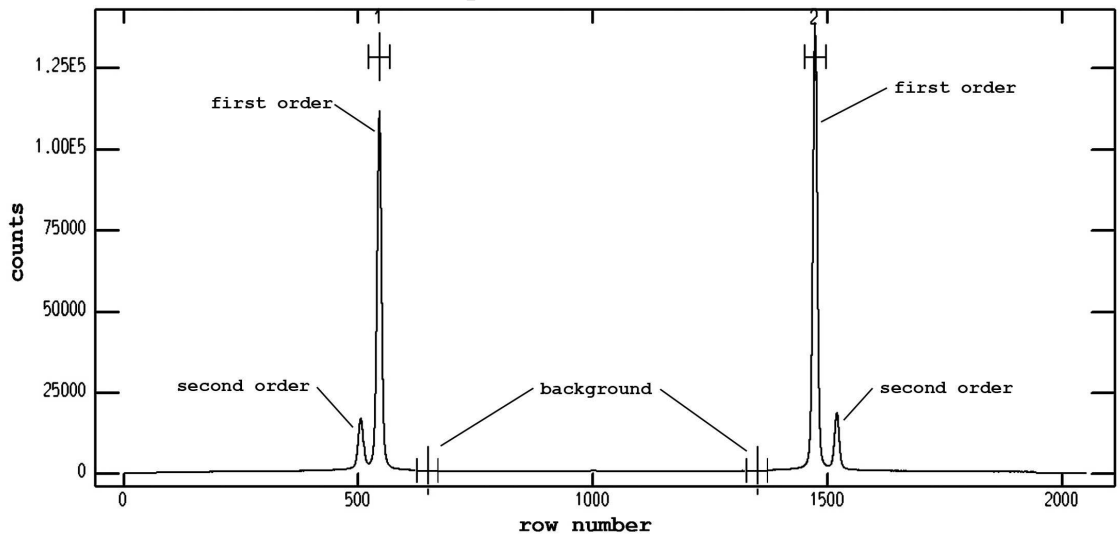

Figure 4.1: Example of O- and E-beam apertures (left and right, respectively), defined at 8000Å for a PG0300 grating spectrum. The aperture widths (indicated by H-shaped bars at the top of the graph) are chosen to minimise contamination from second order spectra clearly visible in regions peripheral to the first-order pair.

After defining the target and background apertures at a wavelength of choice, they were extrapolated to other wavelengths by tracing the shape of the spectrum with a best-fit polynomial of (typically) fifth order. Examples of the typical O- and E-beam aperture profiles for PG0300 grating data are shown in Figures 4.2 and 4.3, respectively. An example of the extracted apertures for the spectra of unpolarised standard star HD14069 observed with the PG0300 grating is shown in Figure 4.4.

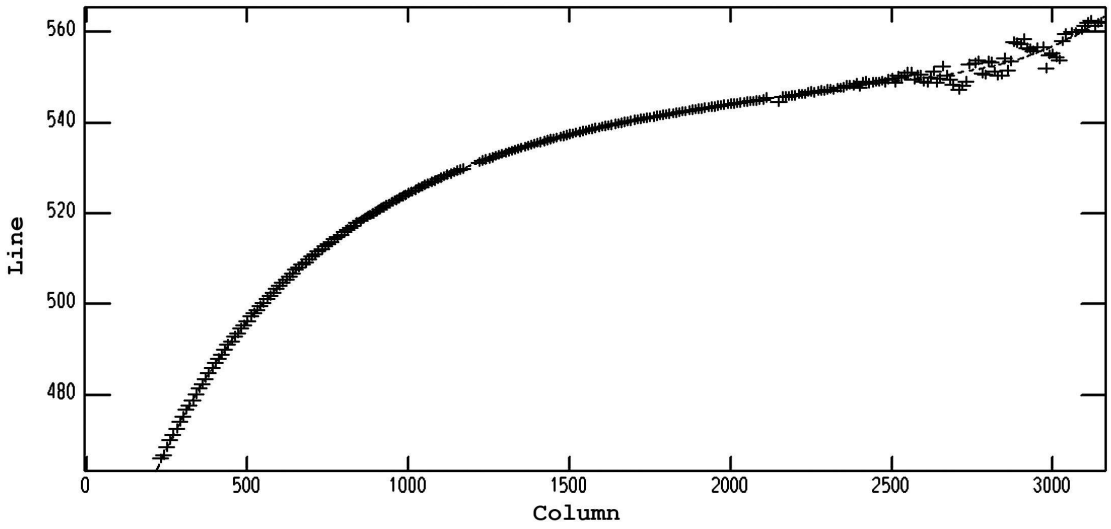

Figure 4.2: O-beam aperture trace for a PG0300 grating spectrum, indicating a fifth order polynomial fit to the aperture shape. Curvature of the spectrum is dominated by the dispersion of the calcite beamsplitter employed in RSS. Breaks at columns ∼1200 and ∼2200 are due to gaps in the CCD detector mosaic.

Using the `apall` task, binning of counts in the "spatial" direction was then performed using the method of *optimal extraction* (Horne, 1986) where each count is weighted according to the intensity of the spectral profile. Background counts from the accompanying background region in the image were then subtracted to correct for sky emission. After such binning a one-dimensional spectrum of electron counts versus wavelength was obtained for each polariser beam.

The above extraction process was repeated for the variance planes of the data, producing an accompanying "variance spectrum" for each science spectrum. These extracted spectra were then used to determine the polarisation parameters of the target using

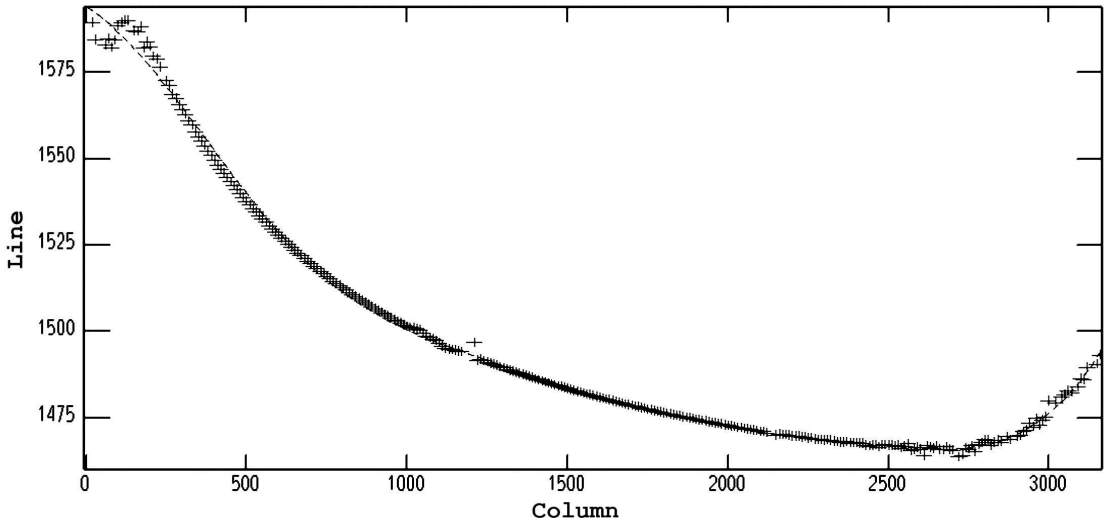

Figure 4.3: E-beam aperture trace for a PG0300 grating spectrum, indicating a fifth order polynomial fit to the aperture shape.

Figure 4.4: Extracted apertures for O- and E-beam spectra (top and bottom panel, respectively) of unpolarised standard star HD14069, observed with the PG0300 grating.

the method described below.

4.4 Reduction Method

In this section the methods introduced in Section 2.7 are extended for specific application to the data used in this study and to include an analysis of the measurement errors. This treatment specifically details linear polarimetry, but may easily be extended to apply to circular and all-Stokes modes. The principal steps involved were using the spectra extracted from each exposure of the waveplate sequence (as described above) to estimate I, Q and U separately for the O- and E-beam, normalising the O- to E-beam derived parameters and combining these to estimate the linear polarisation properties of the target. Custom software was developed, following suggestion from Prof. K. Nordsieck, to implement the methods described here.

4.4.1 Separate-beam analysis

As mentioned in Section 2.7, the method employed in this study considers data from each polarised beam separately. While dual-beam[4] analysis would double the observation efficiency, this assumes a constant (or well characterised) O- versus E-beam throughput efficiency of the instrument. As mentioned in Section 3.2.2, in the case of RSS the E-beam is generally more efficient than the O-beam due to reflection off the 45° fold mirror and dispersion by the grating that affects polarisation efficiency aligned with the beamsplitter optic axis. The E/O efficiency ratio is therefore a (possibly time-varying and wavelength-dependent) function of not only the effects of the dielectric coating on the fold-mirror and the chosen grating and dispersion angle, but also the position angle of the target's polarisation, making it difficult to calibrate to the 0.1% level as required for the calibration goals of this study. For the purposes of this study and until an adequate characterisation of the E/O efficiency ratio is available, combining the results from separate O and E-beam analyses of RSS polarimetric data is therefore proposed as the optimal method.

An example E/O efficiency curve as a function of wavelength for the unpolarised standard star HD14069 is shown in Figure 4.5. In this plot the E/O ratio reflects the average efficiency ratio for all frames in the waveplate sequence. It is clear that in this case the E-beam starts less efficient at 4000Å, but becomes up to ∼10% more efficient from wavelengths of 5000Å and longer.

4.4.2 Normalising the spectra

Firstly a normalisation scheme was used to compensate for variations in the total intensity of the target recorded in each exposure. This occurs due to the varying effective collecting area of the SALT during an observation (as explained in Chapter 3)

[4]directly comparing O- to E-beam intensities to obtain Stokes parameters

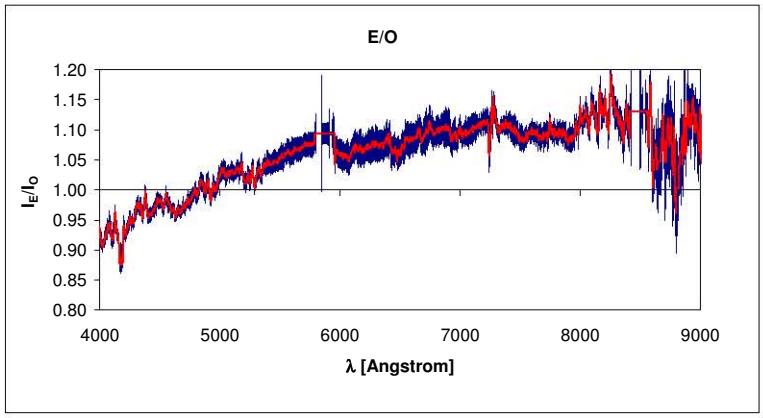

Figure 4.5: Example of the average E/O beam efficiency ratio as a function of wavelength for HD14069, observed with the PG0300 (300 l/mm) grating at an articulation angle of 13°.

and may also occur due to changes in atmospheric transparency, dispersion[5], seeing, telescope focus or position of the target on the slit during the polarimetric sequence. For each exposure i the total intensity at wavelength λ along the spectrum is the sum of the O- and E-beam intensities:

$$I_{tot_{i\lambda}} = I_{O_{i\lambda}} + I_{E_{i\lambda}} \tag{4.2}$$

The same relation holds for the intensity averaged over the wavelength range of the spectrum:

$$\overline{I}_{tot_i} = \overline{I}_{O_i} + \overline{I}_{E_i} \tag{4.3}$$

The mean target intensity during the polarimetry sequence was then estimated by

$$\overline{I}_{tot} = \tfrac{1}{8} \sum_{i=1}^{8} \overline{I}_{tot_i} \tag{4.4}$$

Each point along the spectrum of either beam of exposure i was then normalised by

$$k_i = \frac{\overline{I}_{tot}}{\overline{I}_{tot_i}} \tag{4.5}$$

before intensities from different exposures were compared. k_i therefore represents a normalisation factor to mitigate against variation in sky transparency and system efficiency over time.

[5]The SALT atmospheric dispersion compensator (ADC) was not available during the 2006 observations.

4.4.3 Determining a measure of the systematic error

The redundant information inherent in the eight-frame polarisation exposure sequences defined in Section 2.7 was used to estimate the systematic error as a function of wavelength by determining two independent estimates for I_λ along the spectrum (separately for each polariser beam):

$$I_{1\lambda} = \tfrac{1}{2}\sum_{i=1}^{4} k_i I'_{i\lambda} \tag{4.6}$$

$$I_{2\lambda} = \tfrac{1}{2}\sum_{i=5}^{8} k_i I'_{i\lambda} \tag{4.7}$$

with $I'_{i\lambda}$ the intensity at wavelength λ along the spectrum of exposure i (for the O-beam $I'_{i\lambda} = I_{O_{i\lambda}}$ and for the E-beam $I'_{i\lambda} = I_{E_{i\lambda}}$).

With k_i normalising different exposures, I_1 and I_2 should be equivalent. An estimate of the systematic error along the spectrum could therefore be calculated as

$$\varepsilon_\lambda = \frac{I_{1\lambda} - I_{2\lambda}}{I_{1\lambda} + I_{2\lambda}} \tag{4.8}$$

4.4.4 Normalising the Stokes parameters

The Stokes parameters were estimated separately for each polariser beam according to the relations defined in Section 2.7, but with the normalisation factors k_i included. Additionally the polarisation parameters were expressed as a fraction of the intensity I. For instance, using the standardised notation from Landi Degl'Innocenti et al. 2007, the fractional parameter Q/I at wavelength λ was defined as:

$$P_{Q_\lambda} = \frac{Q_\lambda}{I_\lambda} \tag{4.9}$$

$$= \frac{\frac{1}{2}\sum_{i=1}^{8} \cos 4\phi_i k_i I'_{i\lambda}}{\sum_{i=1}^{8} k_i I'_{i\lambda}} \tag{4.10}$$

with ϕ_i the angle of the half-wave plate at exposure i (compare with Eqn. 2.31). P_U and P_V were determined in a similar fashion.

4.4.5 Estimating the extraction error

With an estimation of the relevant Stokes parameters known, the extent of the spectrum extraction error for each exposure could then be determined by calculating the χ^2 error at each wavelength along the spectrum. In the case of linear polarimetry, from Eqn. 2.30 the χ^2 error was defined as:

$$\chi^2_{i\lambda} = \frac{\delta^2_\lambda}{N^2_\lambda} \tag{4.11}$$

$$= \frac{(\frac{1}{2}I_\lambda(1 + P_{Q_\lambda}\cos 4\phi_i + P_{U_\lambda}\sin 4\phi_i) - k_i I'_{i\lambda})^2}{I_\lambda} \tag{4.12}$$

with δ_λ the deviation between the expected intensity (calculated from Eqn. 2.30 given I_λ, P_{Q_λ} and P_{U_λ}) and the measured intensity ($I'_{i\lambda}$) and N_λ the expected error, based on the assumption that $\sqrt{I_\lambda}$ is a good estimate of the expected noise in photon-noise dominated data[6].

The expected intensity and χ^2 error in the cases of circular and all-Stokes polarimetry can be estimated in similar fashion.

The average χ^2 error at wavelength λ over all exposures in a sequence was then defined as

$$\overline{\chi^2}_\lambda = \tfrac{1}{8}\sum_{i=1}^{8}\chi^2_{i\lambda}. \tag{4.13}$$

Finally, it is customary to report the *reduced* χ^2 error where the results are normalised to the degrees of freedom of the estimation, to make the results more easily comparable.

The reduced χ^2 value is simply determined as:

$$\overline{\chi^2}_{\lambda,red} = \tfrac{1}{N-n}\overline{\chi^2}_\lambda, \tag{4.14}$$

where $N - n$ represents the degrees of freedom, with N the number of observations (number of exposures in the waveplate sequence) and n the number of parameters being estimated (Q and U in the case of linear polarimetry).

[6] Alternatively, for low signal-to-noise data, a more accurate estimation of N_λ would be to use the variance-plane data obtained during spectrum extraction as defined in Section 4.1

The average of this value for the O- and E-beam was used as a scaling factor of the measurement error of the polarisation parameters (see Section 4.4.8).

4.4.6 Combining data from the O- and E-beams

The methods described above may be used to obtain the polarisation parameters by inspecting only one of the polariser beams. Making use of both beams improves the signal-to-noise ratio of the estimation and was calculated for each parameter from:

$$X_\lambda = \tfrac{1}{2}\left(X_{O_\lambda} - X_{E_\lambda}\right), \tag{4.15}$$

where X is one of P_Q, P_U or P_V determined for each of the two beams.

As an additional diagnostic parameter, the average E/O beam efficiency ratio for the polarimetry sequence as a function of wavelength was determined from:

$$(E/O)_\lambda = \frac{I_{E_\lambda}}{I_{O_\lambda}}, \tag{4.16}$$

with I_{X_λ} the intensity at wavelength λ for polariser beam X, averaged over all exposures of the waveplate sequence:

$$I_{X_\lambda} = \tfrac{1}{8}\sum_{i=1}^{8} I_{X_{i\lambda}} \tag{4.17}$$

4.4.7 Determining a data-quality mask

A χ^2-clipping threshold was used to discard data points exhibiting excessive extraction errors. A data-quality vector was constructed separately for the O- and E-beam such that

$$\begin{aligned} DQ_\lambda &= 1 \text{ for } \overline{\chi^2}_{\lambda,red} < \kappa, \\ DQ_\lambda &= 0 \text{ otherwise,} \end{aligned} \tag{4.18}$$

where κ was chosen subjectively as a constant for a specific polarimetry data set, depending on the extraction errors present. The data-quality vector for combined

O+E beam polarisation parameters was then simply calculated as

$$DQ_\lambda = DQ_{O_\lambda} \cdot DQ_{E_\lambda}, \tag{4.19}$$

Data points where $DQ_\lambda = 1$ were included in further analysis, while values corresponding to $DQ_\lambda = 0$ were excluded.

4.4.8 Measurement errors and binning

Measurement errors were estimated from the variance-plane spectra obtained during spectrum extraction as defined in Eqn 4.1. Assuming $P_Q \approx P_U$, the same error amplitude can be assumed for all three fractional intensity parameters P_Q, P_U and P_L (Fossati et al., 2007). This error was defined as:

$$\sigma_{P_\lambda} = \frac{1}{\sqrt{\sigma_{I_\lambda}}} \text{ rad}, \tag{4.20}$$

where σ_I is the variance spectrum. The measurement error in radians for the position angle (PA) was defined as

$$\sigma_{PA_\lambda} = \frac{\sigma_{P_\lambda}}{P_{L_\lambda}} \text{ rad}, \tag{4.21}$$

These errors were then reduced by co-adding, or binning, data points along the spectrum.

The binned values were defined as:

$$N_k = \sum_{i=(k-1)N}^{kN-1} DQ_{\lambda_i} \tag{4.22}$$

$$\overline{DQ}_k = 1 \text{ for } N_k > 0, \text{ 0 otherwise} \tag{4.23}$$

$$\overline{\lambda}_k = \frac{1}{N_k} \sum_{i=(k-1)N}^{kN-1} \lambda_i DQ_{\lambda_i} \tag{4.24}$$

$$\overline{X}_k = \frac{1}{N_k} \sum_{i=(k-1)N}^{kN-1} X_{\lambda_i} DQ_{\lambda_i} \tag{4.25}$$

$$\overline{\sigma}_{P_k} = \frac{1}{\sqrt{\sum_{i=(k-1)N}^{kN-1} \sigma_{I_{\lambda_i}} DQ_{\lambda_i}}} \tag{4.26}$$

$$\overline{\chi^2}_{k,red} = \frac{1}{N_k} \sum_{i=(k-1)N}^{kN-1} \overline{\chi^2}_{\lambda,red_i} DQ_{\lambda_i}, \tag{4.27}$$

where N_k is the number of valid data points within bin k, $\overline{DQ}_k$ defines the data-quality indication of bin k, $\overline{\lambda}_k$ is the weighted-mean wavelength of the bin, $\overline{X}_k$ is the weighted-mean signal value with X representing P_Q or P_U, $\overline{\sigma}_{P_k}$ is the reduced error and $\overline{\chi^2}_{k,red}$ is the weighted-mean reduced-χ^2 error. Binned values were only defined if $\overline{DQ}_k = 1$. $\overline{\sigma}_{PA_k}$ was determined as in Eqn. 4.21, but from σ_{P_λ} and P_{L_λ} derived from the binned versions of P_Q and P_U.

For low signal-to-noise data, a statistically superior method of calculating the binned values of P_Q and P_U would be summation of the raw intensity data ($I'_{i\lambda}$), from which the binned stokes parameters are then determined.

Finally, as mentioned above, the average χ^2 error within each bin was used to scale $\overline{\sigma}_{P_{\lambda_k}}$ to include the contribution of extraction errors. This scaling factor was defined as:

$$\eta_k = 1 \text{ for } \overline{\chi^2}_{k,red} < 1, \tag{4.28}$$

$$\eta_k = \sqrt{\overline{\chi^2}_{k,red}} \text{ otherwise}, \tag{4.29}$$

limiting the scaling factor to be > 1, since η_k can never reduce the error.

4.4.9 Position angle calibration

The PA obtained thus far remained to be corrected for any wavelength-dependent instrumental PA. Such a curve was determined via laboratory measurements by the principal investigator for RSS (K.H. Nordsieck) and is reproduced in Figure 4.6. The correction applied to the measured PA was then:

$$PA'_\lambda = MOD\pi(PA_\lambda + \alpha_\lambda) - \tfrac{\pi}{2}, \tag{4.30}$$

where $MOD\pi(x)$ represents the modulus of x with respect to π and α_λ is the value of the instrumental polarisation curve at wavelength λ. The original data was interpolated by a cubic spline curve to obtain estimates of the correction at any specific λ. With this correction applied, the only remaining adjustment required to obtain the equatorial position angle should be a constant offset.

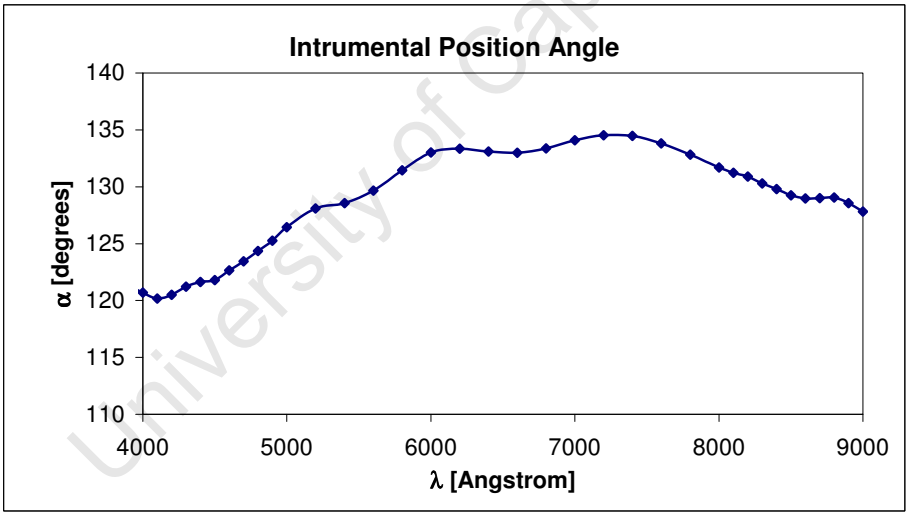

Figure 4.6: RSS instrumental position-angle curve, from Nordsieck (private communication).

4.4.10 Determining mean values

In cases where polarisation parameters remained fairly constant over the wavelength range, an inverse-error-weighted mean of the binned values was defined as:

$$\overline{X} = \frac{1}{\Gamma}\sum_{k=1}^{M}\gamma_k\overline{X}_k, \text{ with} \tag{4.31}$$

$$\gamma_k = \frac{MIN\{\overline{\sigma}_{P_k}\}}{\overline{\sigma}_{P_k}} \text{ and} \tag{4.32}$$

$$\Gamma = \sum_{k=1}^{M}\gamma_k, \tag{4.33}$$

where X can be P_Q or P_U, and M is the total number of bins. γ_k represents a weighting factor that equals 1 for the bin with smallest error and scales inversely to the error for larger errors ("MIN{}" indicates the *minimum* operation). The weighted mean was normalised by the sum of these weights, Γ. Values for P_L and PA were then determined as per Eqn. 2.34, but from the binned instances of P_Q and P_U.

The methods described here were applied to data obtained for polarised and unpolarised standard stars to estimate the combined instrumental polarisation characteristics of the SALT and RSS, and the results are discussed in the following chapter.

Chapter 5

Observations and results

5.1 Objectives

The objectives of this study are firstly to develop reduction techniques suitable for reducing RSS polarimetry data and secondly to apply these methods in characterising instrument and telescope polarimetric parameters - specifically estimating the level of instrumental linear polarisation and the relation of the position angle of this polarisation as determined via the reduction routines compared to the actual equatorial position angle.

A further aim is to investigate the quality of the observations and the reduction method by determining the extent of the systematic and extraction errors of each data set. Additional information (telescope tracker trajectory, effective pupil size and RSS E/O beam efficiency) for each observation is presented to aid in analysing possible causes for these errors and to provide some information on the E/O beam efficiency ratio of RSS under various conditions.

5.2 Data

This section details the data used in this study, including the requirements of each data set to allow for polarimetric and error analysis and the observations performed to collect the data.

5.2.1 Requirements

Spectro-polarimetric data of unpolarised and strongly-polarised targets were required. The redundant information available from full eight-frame linear polarimetric observations allow for estimation of systematic and extraction errors within each data set. Science data were accompanied by at least one arc spectrum taken just prior or following the polarimetric sequence to allow for wavelength calibration. The availability of bias frames further aids in reducing extraction artifacts. In the case of differential spectro-polarimetry flat fielding is typically not required. While flat-fielding may yield additional insights in the analysis systematic and extraction errors, these were not included as part of this study, largely because the SALT calibration system was not yet fully commissioned.

5.2.2 Observations

Spectro-polarimetric data were obtained by K.H. Nordsieck, S.B. Potter and the author with the aid of the resident SALT Operators during observing runs in late 2006. Polarised and unpolarised standard stars were observed, appropriate for characterisation of the instrument and verification of the reduction techniques.

While unpolarised standards may be used to estimate the extent of instrumental and telescope polarisation, highly polarised targets are useful for verifying the performance of the reduction technique as well as the position angle offset of the measured linear polarisation.

Unpolarised standards HD14069 and HD12021 (Mathewson and Ford, 1970) were selected from the available data. The characteristics for each target are listed in Table 5.1.

Object	$\mathbf{P_L}$	**PA**
HD14069	0.03%	17.8°
HD12021	0.06%	152.4°

Table 5.1: Unpolarised standards, from Mathewson and Ford (1970). The columns P_L and PA indicate the percentage linear polarisation and its position angle, respectively (no estimates of the measurement errors are presented for these targets in the reference text).

Data for polarised standards HD73882 (Serkowski, Mathewson and Ford, 1975) and Vela 1 #95, (Fossati et al., 2007) were available and selected as suitable targets for this study due to their significant degree of linear polarisation and well defined position angle in each case. Information on these targets is listed in Table 5.2 and shown as a function of wavelength in Figures 5.1 and 5.2, from UBVRI polarimetry.

Refer to Table 5.3 for a complete list of observations.

Object	$\mathbf{P_L}$**(average)**	**PA (average)**
HD73882	$2.0 \pm 0.05\%$	$164.25 \pm 1.09°$
Vela1 #95	$7.49 \pm 0.06\%$	$172.0 \pm 0.28°$

Table 5.2: Average linear polarisation parameters for polarised standards, adapted from Serkowski et al. (1975) and Fossati et al. (2007).

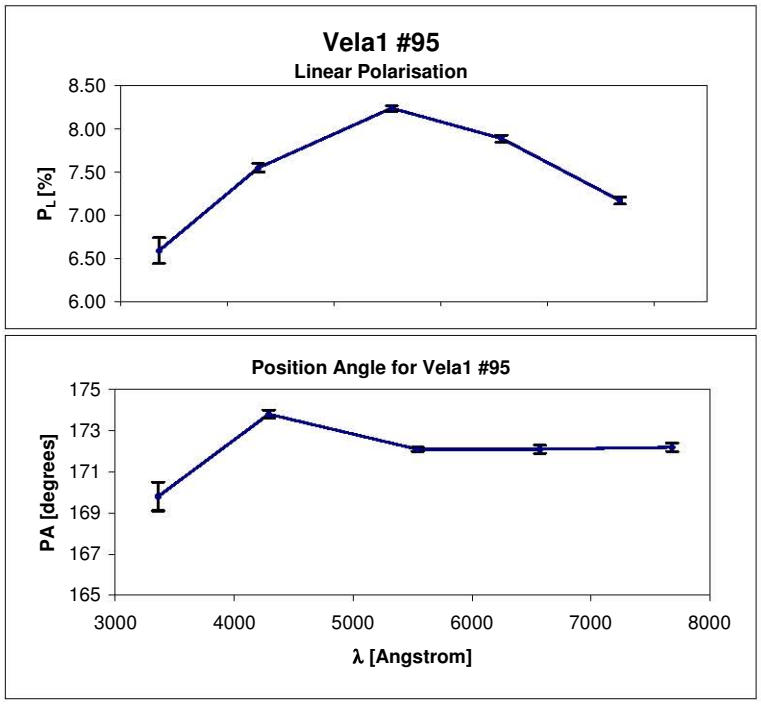

Figure 5.1: Vela1 #95: Linear polarisation characteristics, adapted from Fossati et al. (2007).

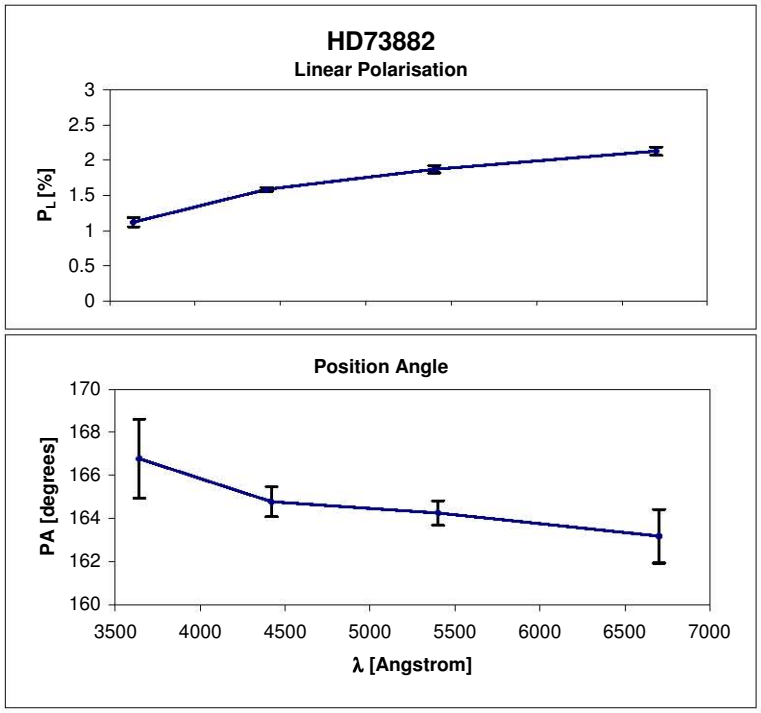

Figure 5.2: HD73882: Linear polarisation characteristics, adapted from Serkowski et al. (1975).

Date	*Target*	*Grating*	*Artic.*	*Exposures*	*Gain / Readout*	filter	*Type*
20061029	HD73882	PG0900	26.5°	8×40s	B/F	PC03200	Pol
20061029	HD73882	PG0900	40°	8×40s	B/F	PC04600	Pol
20061101	HD14069	PG0900	26.5°	16×60s	B/F	PC03200	Unpol
20061101	Vela1 #95	PG0900	40°	8×100s	F/S	PC04600	Pol
20061105	HD14069	PG0900	40°	8×100s	F/S	PC04600	Unpol
20061107	HD14069	PG0300	13°	8×100s	B/F	PC00000	Unpol
20061107	HD14069	PG0300	13°	8×100s	B/F	PC00000	Unpol
20061107	HD14069	PG0300	13°	8×100s	B/F	PC00000	Unpol
20061111	HD12021	PG0300	13°	8×100s	B/F	PC00000	Unpol

Table 5.3: List of polarimetric standards observed during the 2006 observing run and used in this study. Columns indicate the grating used (PG0300 and PG0900 indicate the 300 l/mm and 900 l/mm gratings, respectively), articulation angle, number and length of exposures, gain (B=Bright, F=Faint), readout speed (F=Fast, S=Slow), the cutoff filter used (PC00000=clear filter), and finally the object type (Pol=Polarised standard, Unpol=Unpolarised standard). All observations were performed at 2x2 pre-binning of the CCD and using a 1.5 arc-second wide focal-plane slit.

5.3 Estimation of instrumental polarisation

In this section data from unpolarised standard star observations are analysed to estimate the extent of instrumental linear polarisation contributed by the SALT and RSS as a combined system.

5.3.1 Observations

The unpolarised standard HD14069 was observed using the standard 8-frame linear polarimetry sequence described in Section 2.7. The target was observed multiple times while varying the instrument configuration and the target's position in the telescope field-of-view to sample effects these parameters may have on the observed polarisation.

Firstly, the target was observed with the PG0300 (300 l/mm) grating to obtain simultaneous coverage of the available spectral range provided by SALT. Secondly the PG0900 (900 l/mm) grating was employed to obtain medium-resolution results for the blue and red half of the spectral range respectively. Finally the PG0300 grating was used to obtain results with the target at 1.5 arc-minutes off-axis in the field-of-view, as opposed to the standard on-axis configuration.

Data for a second unpolarised standard, HD12021, taken with the PG0300 grating was analysed to independently verify the on-axis results obtained earlier.

5.3.2 Results and discussion

HD14069: PG0300 grating

The extraction results for HD14069 observed with the PG0300 grating and an articulation angle of 13° covering the entire 4000Å to 9000Å wavelength range are shown in Figure 5.3. The left panel indicates results for the O-beam, with those for the E-beam at right. From the top down, the panels show the raw extracted spectra for each of

the eight exposures in the waveplate sequence (and corresponding waveplate angle in boxes on the right), the data-quality (DQ) mask derived from the χ^2-clipping threshold (plotted points indicate areas of valid data), the systematic error and finally the reduced-χ^2 extraction error as a function of wavelength.

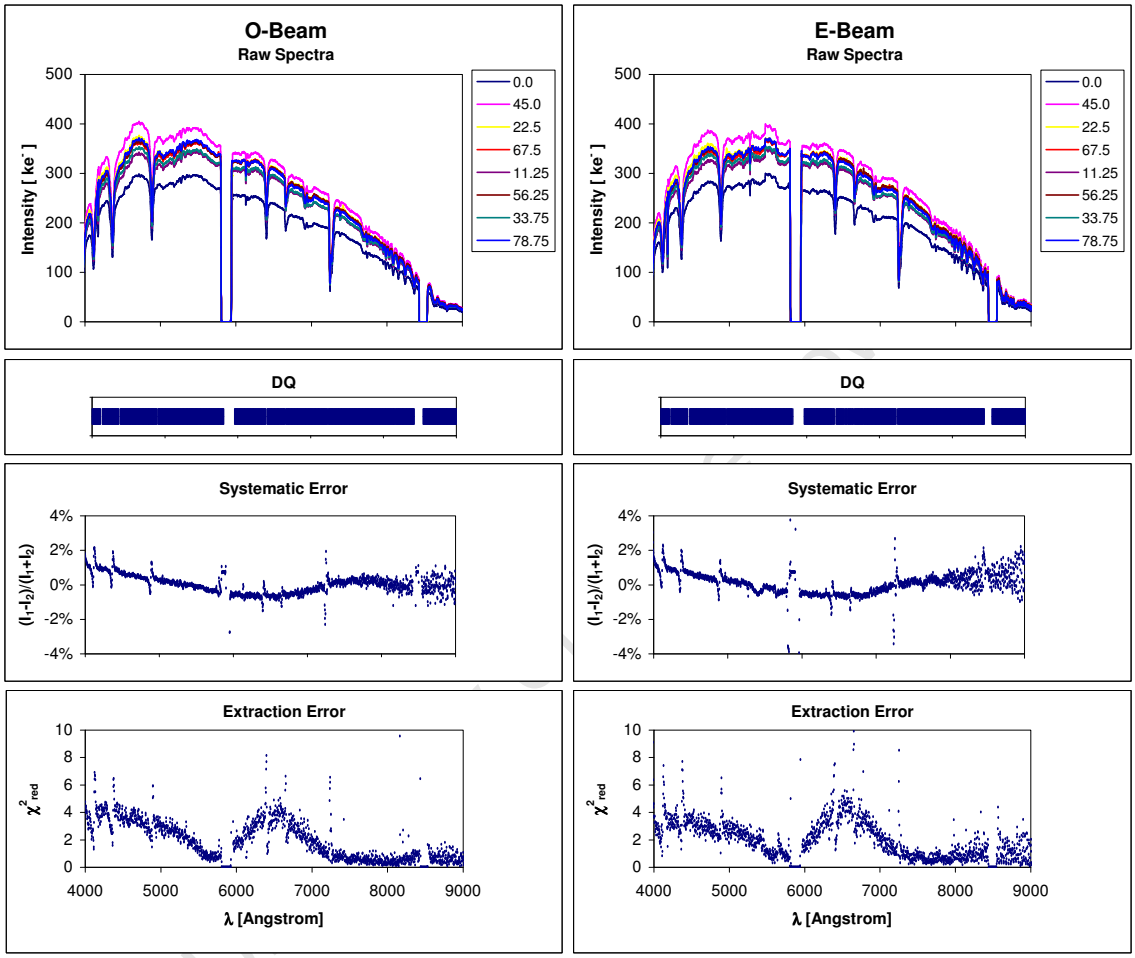

Figure 5.3: HD14069 extraction results for O and E beam (PG0300 grating).

An artifact is visible on the raw E-beam spectra (at 5600Å) if compared to the O-beam. This arose due to two row-aligned linear blemishes at or close to the CCD surface at the position of the E-beam aperture (on either side of the "bump" in the spectra). This artifact is also clearly visible in the E/O efficiency ratio shown in Figure 5.6. As the amount of signal lost is similar in all the exposures this only causes a slight deviation in systematic error and does not significantly affect the polarisation results.

The lower counts seen in the first exposure of the sequence ($\phi = 0°$) indicates a decrease

in system efficiency, most likely caused by slit-losses due to the target drifting slightly from the focal-plane slit. After normalisation (by scaling each exposure to match the intensity of the average exposure, as defined by Eqn. 4.5) a slowly varying systematic error of amplitude $\sim 1\%$ remains, also visible as an elevated extraction error (compared to an expected value of order 1). Additional "spikes" are evident in both systematic and extraction plots, caused by slight (sub-pixel) variation of the wavelength solution for each exposure that are enhanced by discontinuities in the spectrum at strong absorbtion features and detector boundaries. An increase in systematic noise is also evident as the total intensity of the target spectrum drops dramatically at wavelengths longer than ~ 8500Å.

As defined by Eqn. 4.13, a wavelength-dependent systematic error indicates changes in shape of the observed spectra over the exposure sequence not consistent with the assumption that the total intensity for each polariser beam is the sum of the intensities over the first and second set of four exposures - as would be expected only for a perfect system. Causes for this error may therefore include:

1. Observational issues, such as an atmospherically dispersed object drifting in the slit (these observations were performed without the SALT atmospheric dispersion compensator (ADC) installed).

2. Spectrum extraction errors, such as drift of the spectrum profile as compared to the extraction aperture or varying amounts of higher-order spectra spilling into the aperture for each exposure.

3. Wavelength dependence of the optical system's efficiency as a function of time / tracker position, where the motion of the tracker during the observation may cause wavelength-dependent variations in efficiency. For instance, different primary mirror segments visible within the moving pupil exhibit different reflectance characteristics and changes in the telecentric angle affects instrumental polarisation from the primary mirror (see Figure 3.9).

4. Wavelength dependence of the optical system's efficiency as a function of polar-

isation, where the rotation of the linear waveplate between each exposure may cause varying efficiency, for instance in the reflectivity of the RSS fold-mirror.

Extraction errors from the reduced-χ^2 values firstly include any systematic errors, and secondly indicate variation in intensity of the spectra not expected due to polarisation, given the estimated Q and U values.

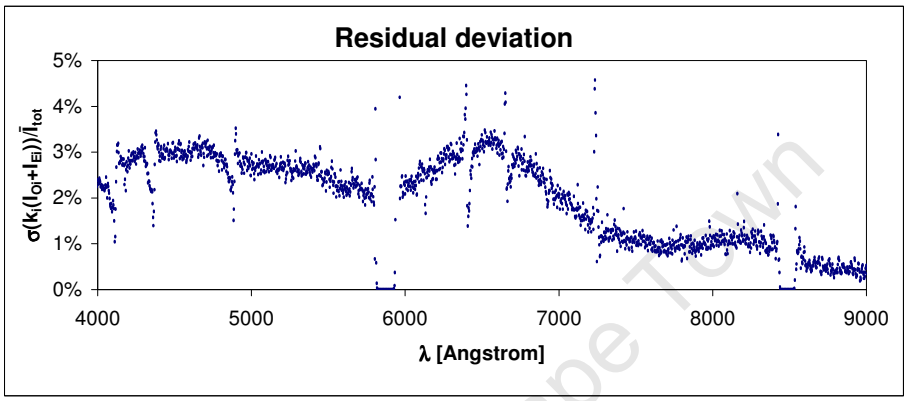

Figure 5.4: Standard deviation of the normalised O+E beam intensity within the set of eight exposures of the waveplate sequence. Data for HD14069 using the PG0300 grating.

The errors shown in Figure 5.3 were analysed further by comparing the summed O+E beam spectra from each exposure after they were normalised to compensate for variations in system efficiency (as per Eqn. 4.5). One would expect the sum of the O- and E-beam intensities (at every wavelength) to be equal for all exposures once normalised (barring noise). Any residual variation between exposures as a function of wavelength would then indicate a change in shape of the spectra during the observation. The remaining variation of the normalised O+E intensities over the eight exposures of the observation (estimated by calculating the standard deviation of the eight values) is indicated in Figure 5.4. This 1-σ deviation (indicated as a percentage of the average intensity during the observation, $\overline{I}_{tot}$) as a function of wavelength closely echoes the extraction errors shown in the bottom panels of Figure 5.3 and indicates that the main component of this error is indeed the underlying systematic error. For this specific observation, spectrum extraction errors (cause number 2. above) were likely not the

cause for the systematic error, as extreme care was taken to ensure correct aperture definitions.

The trajectory of the SALT tracker during the exposure sequence is indicated in Figure 5.5 (left). The physical X and Y position of the tracker mechanism is shown, indicating the trajectory location within the total available envelope of ±1.6 meters in each axis. The origin of the trajectory (at readout of the first exposure) is circled, indicating a North/South (telescope structure azimuth) trajectory starting at the periphery of the primary mirror, moving towards the centre in X during the sequence. The tracker location directly relates to the effective collecting area of the SALT (maximum at centre) as well as which primary mirror segments contribute to the detected signal.

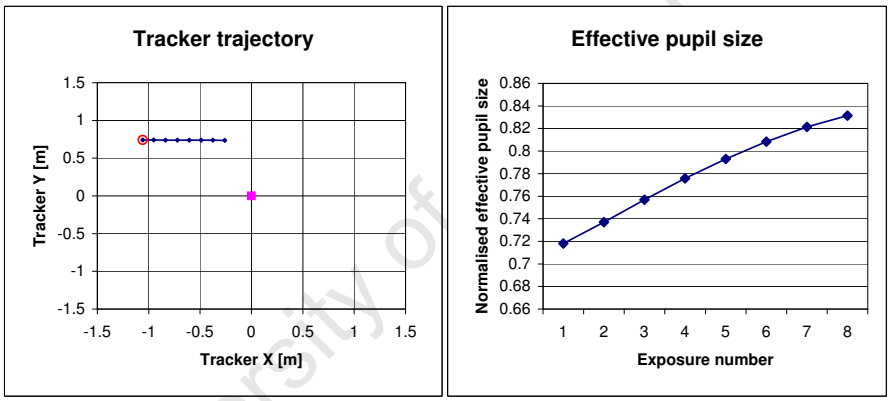

Figure 5.5: Observation trajectory and effective pupil size (left and right panels, respectively) for HD14069 observed with the PG0300 grating. The origin of the track is circled and the centre of the primary mirror is indicated by a square.

The effective telescope pupil size at each exposure's readout time is indicated in the right-hand panel of Figure 5.5. Given the tracker location for each exposure, a simplified approximation of the effective collecting area for each was estimated by determining the location of the telescope entrance pupil on the primary mirror (via the SALT Telescope Control System's pointing model) and approximating the telescope primary mirror as a monolithic circular mirror with a diameter of 11 metres. The overlap in area between the pupil and the primary mirror then provides an estimate of the collecting area. The values plotted here are normalised to the maximum collecting area.

The effect of the track on the collecting area is clear with the effective pupil starting at 72% of the maximum available area and increasing towards 83% as the track progresses towards the centre of the primary.

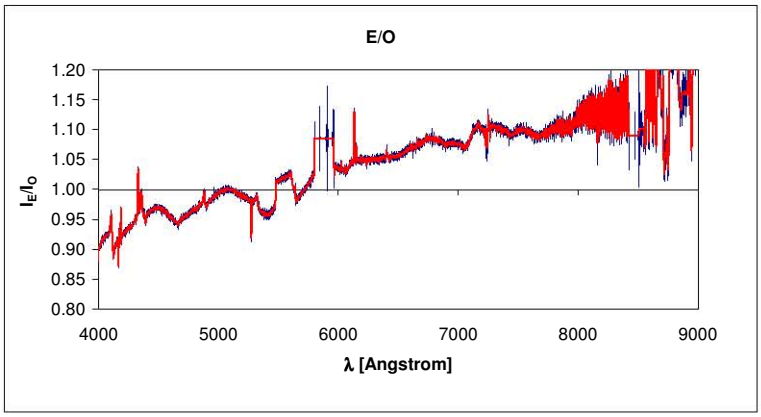

Figure 5.6: The average E/O beam intensity ratio for HD14069 (PG0300 grating), shown in red. The standard deviation of this ratio between the exposures of the observation is indicated by error bars (blue) above and below the red line.

The E/O beam intensity ratio as a function of wavelength, as averaged over all eight exposures, is shown in Figure 5.6, indicating a fairly linear relationship between the efficiency ratio and wavelength with the E-beam efficiency starting ∼10% lower than the O-beam at 4000Å, becoming more efficient at $\lambda \simeq 6000$Å and peaking at ∼10% above the O-beam at 9000Å. The artifact on the E-beam data around 5600Å is again visible in this plot as well as the CCD mosaicing gaps. As stated earlier, the E/O beam efficiency ratio is a complex function of the RSS fold-mirror characteristics, the grating used, the dispersion angle and the position angle of any polarisation present in the incident light from the target. Barely visible in this plot are "error bars" (in dark blue) above and below the graph. This indicates the standard deviation of the E/O ratio over the eight exposures in the observation. In this case the exposure-to-exposure deviation is small (<1%) as would be expected for an unpolarised target.

The polarimetry results for HD14069 observed with the PG0300 grating are detailed in Figure 5.7. The top panels show the target spectrum's total intensity (I), calculated from the sum of the eight raw O- (left-hand panel) and E-beam (right-hand panel)

exposures. The two detector-gaps are clearly visible at $\sim$ 6000Å and $\sim$ 8500Å. The next pair of panels indicate the raw (indicating un-binned) estimates for P_Q and P_U at left and right, respectively. In each case the red trend-line indicates a moving-window average, alluding to the binned results shown in the following two plots. Finally the bottom panels detail binned plots of the linear polarisation P_L and its position angle PA. The binned plots also indicate the reduced-χ^2 scaled error bars. Unless otherwise specified a constant binning window of 100 data points was used for all targets.

The relatively small amount of scatter in the raw P_Q and P_U results (second panel from the top) indicate good consistency between exposures and low levels of error. P_Q and P_U values are typically below 0.2% over the wavelength range, resulting in linear polarisation values of 0.2% in the blue, reducing to $\sim$ 0.1% in the red. This compares with the known unpolarised nature of HD14069 ($P_L = 0.03\%$) and directly indicates what the contribution of the telescope and RSS is to the instrumental linear polarisation. The position angle is not well defined for this unpolarised target, as indicated by relatively large ($\sim$10°) error bars in the bottom-right panel of Figure 5.7. An increasing trend is, however, present with the PA starting at $\sim$109° in the blue and reaching 135° at $\sim$6500Å.

The inverse-error weighted-mean values (as defined by Eqn. 4.31) for the polarisation parameters of this data set are listed in Table 5.4, indicating an average instrumental linear polarisation of 0.17±0.02%.

$\mathbf{P_Q}$	$\mathbf{P_U}$	$\mathbf{P_L}$	**PA**
$0.12 \pm 0.02\%$	$-0.09 \pm 0.02\%$	$0.17 \pm 0.02\%$	$123.3 \pm 4.6°$

Table 5.4: HD14069 weighted-mean values of the polarisation parameters (PG0300 grating).

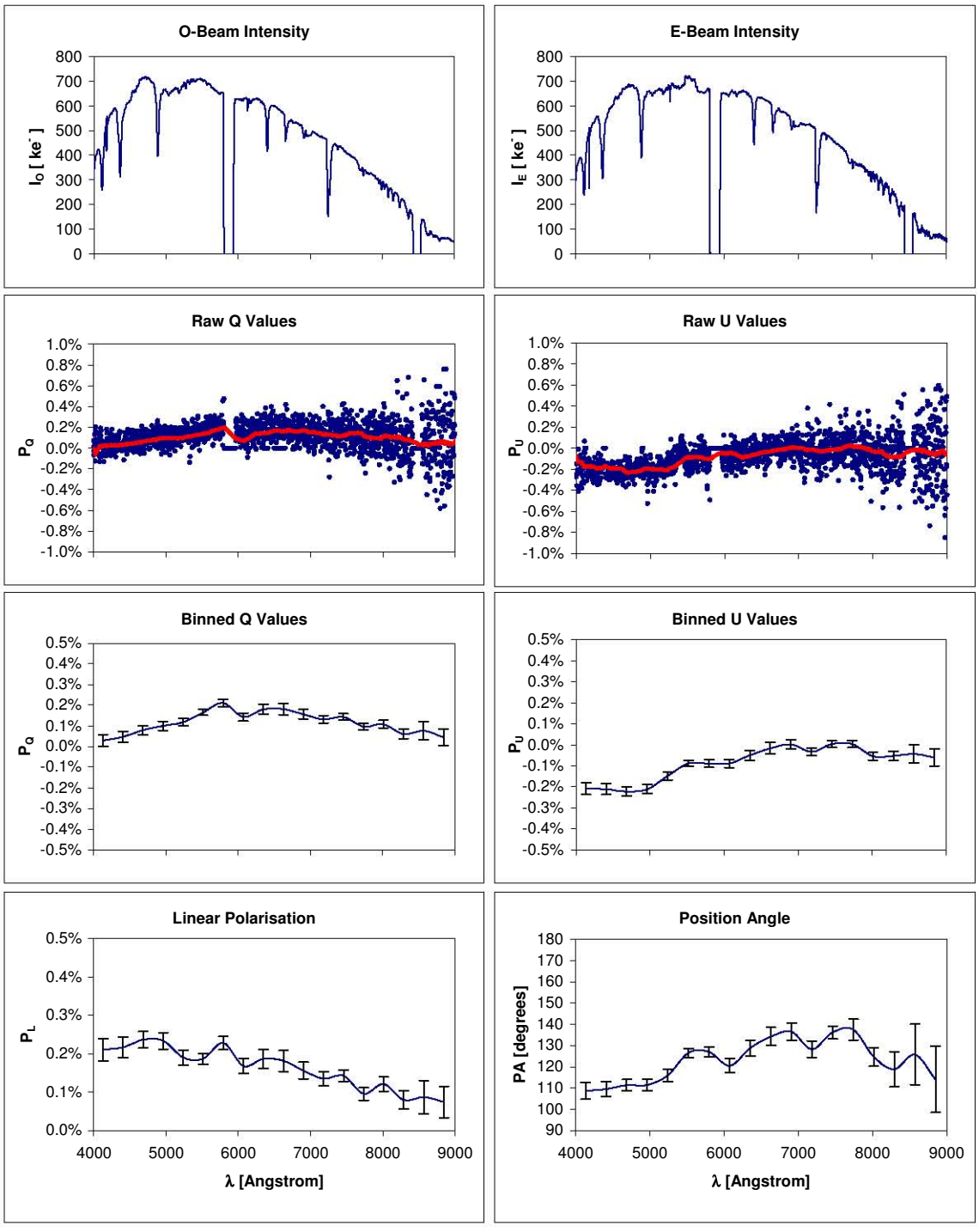

Figure 5.7: HD14069 linear polarisation parameters (PG0300 grating).

HD14069: PG0900 grating, blue coverage

Extraction results for HD14069 observed with the PG0900 grating and an articulation angle of 26.5° covering the blue end of the spectrum (3450Å to 6700Å) are shown in Figure 5.9. As before the left panel indicates results for the O-beam, with E-beam plots at right.

The tracker trajectory and effective pupil size plot in Figure 5.8 indicate a track starting near the centre in X, but already at 851 mm in Y and moving towards a more marginal pupil size as the polarimetry sequence progresses. This progressive decrease in effective collecting area is evident in the raw spectrum plots in Figure 5.9, where successive exposures yield lower average counts.

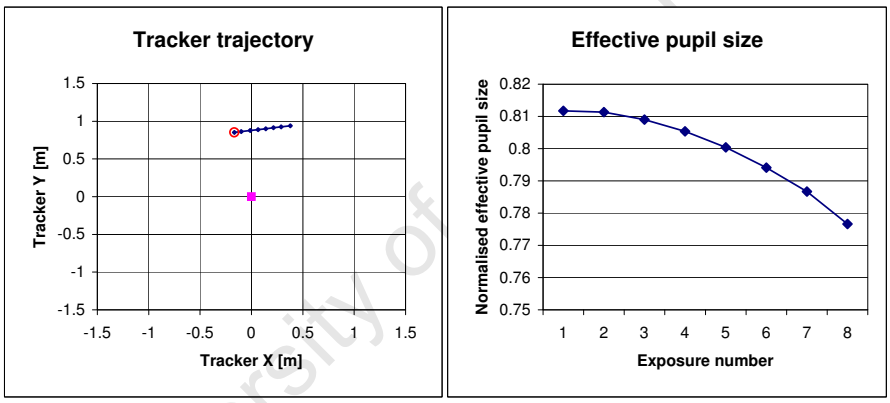

Figure 5.8: Observation trajectory and effective pupil size (left and right panels, respectively) for HD14069 (PG0900 grating, blue coverage).

After normalisation (as per Section 4.4.2) a systematic error is evident comprising of both a slowly varying component (again due to remaining deviation of the normalised spectral shape between the exposures) as well as higher frequency "ripples" of almost 1% in amplitude. The "period" of this latter component is shorter at the blue end of the spectrum and longer towards the red end, indicative of some kind of optical interference or diffraction effect. These "ripples" are also evident in the raw spectra and result in a systematic error because of their varying nature in time (dependent on tracker position and possibly waveplate angle). In order to rule out an extraction artifact as the cause of this error the original images were inspected and it was found that even for

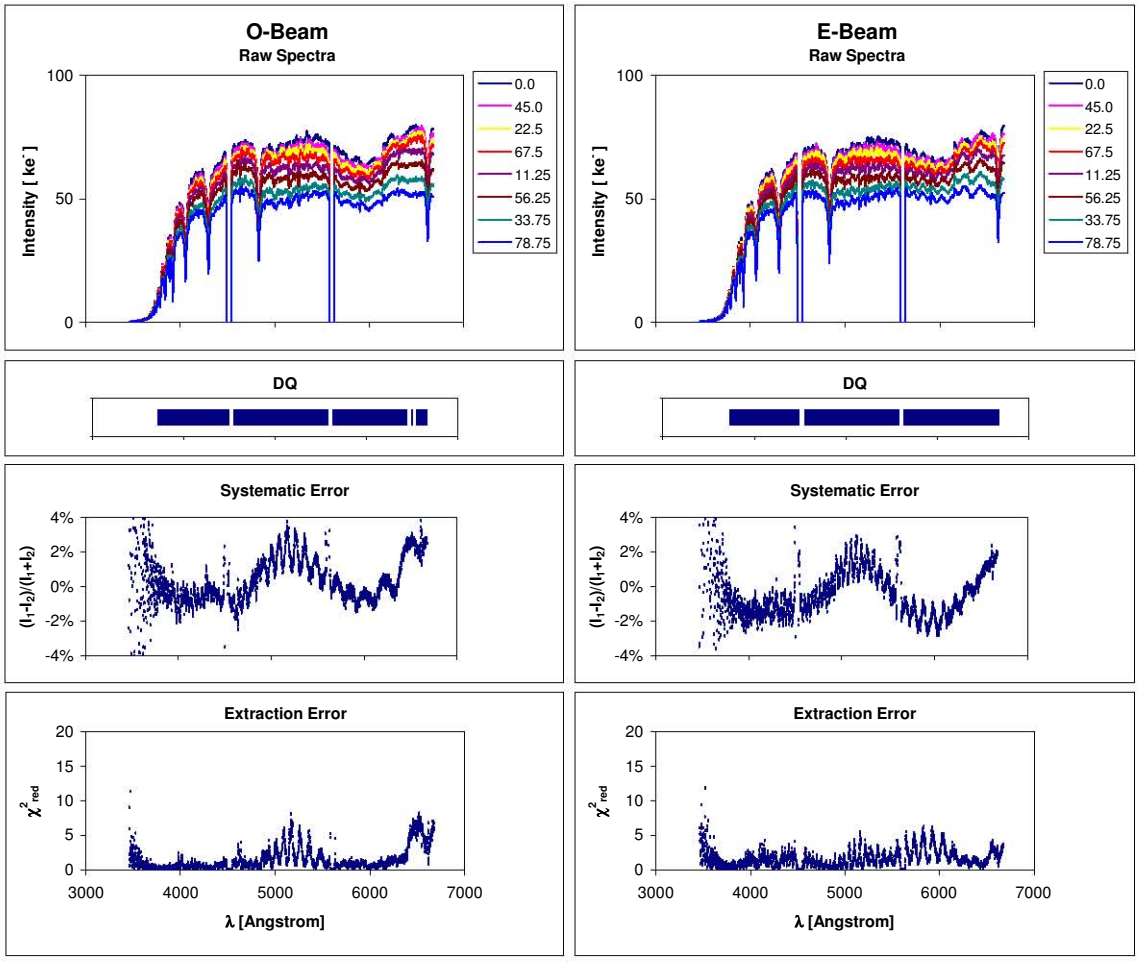

Figure 5.9: HD14069 extraction results for O and E beam (PG0900 grating, blue coverage).

two successive exposures with identical instrument configuration (including waveplate angle) the wavelength dependence of this interference does not remain constant. This is indicated in Figure 5.10, where the difference image between two such exposures is shown, indicating some variation over time. Typically a higher average frequency and larger change in frequency of the interference pattern is seen in the E-beam (top aperture), as illustrated in the difference spectra shown in Figure 5.11.

These systematic errors also translate into relatively large extraction errors shown in the bottom panels of Figure 5.9.

The independent effect of this interference pattern on the O- and E-beam is also evident

Figure 5.10: Difference image of two spectro-polarimetric exposures taken with the same instrument configuration (PG0900 grating, 26.5° articulation angle) during the same telescope track, indicating a time-varying interference component in both the E- and O-beam (top and bottom spectrum, respectively).

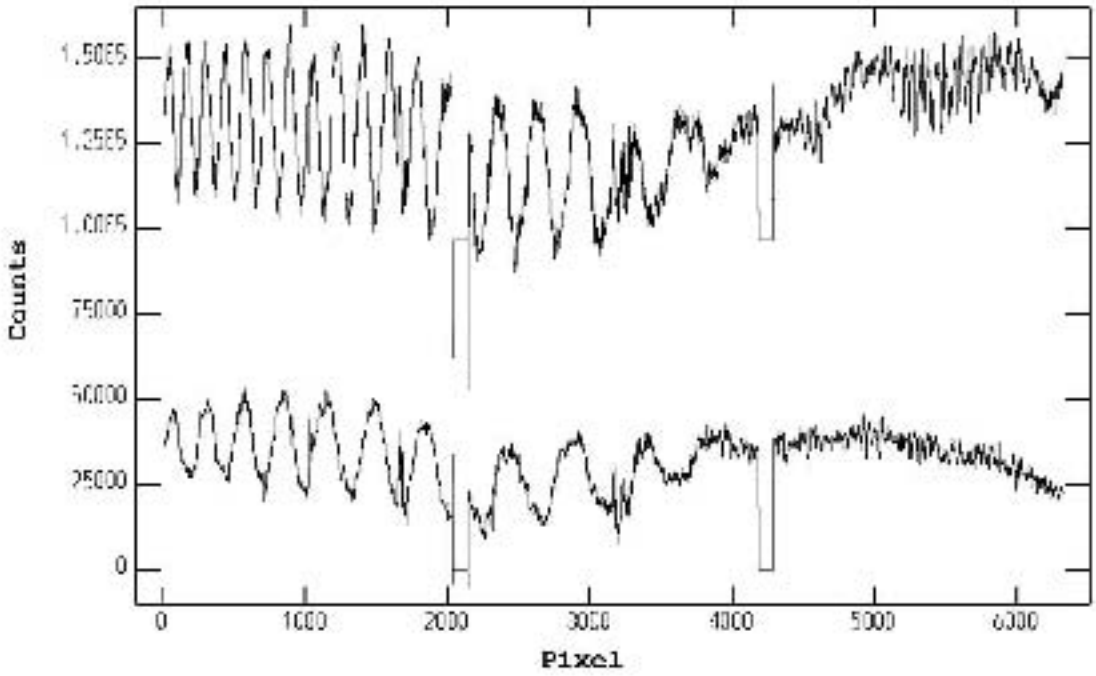

Figure 5.11: Difference spectra of two spectro-polarimetric exposures taken with the same instrument configuration (PG0900 grating, 26.5° grating angle), indicating a time-varying interference component. The two spectra are offset by 100,000 counts for clarity, with the E-beam difference spectrum at top.

from the E/O efficiency ratio plotted in Figure 5.12, where a more prominent "ripple" is seen at longer wavelengths, above 5500Å. Excluding this effect, the O- and E-beams remain within 5% of equal efficiency over most of the wavelength range. Large scatter below 4000Å is due to the low intensity of the spectrum in this region. The standard deviation of this ratio between the eight exposures of the observation is small at ∼2%.

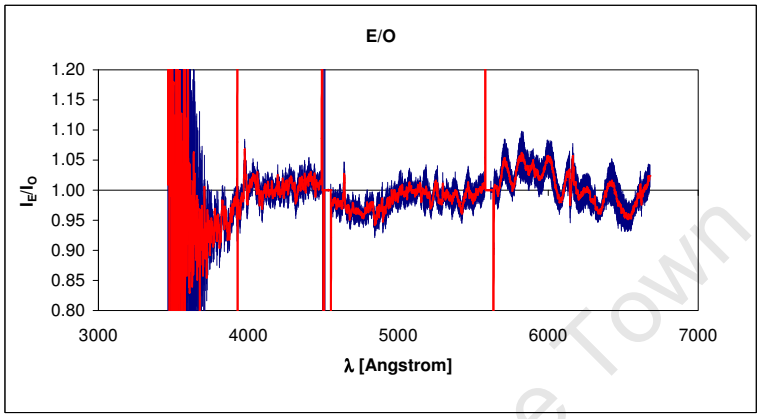

Figure 5.12: E/O beam intensity ratio for HD14069 (PG0900 grating, blue coverage), shown in red. The standard deviation of this ratio over the exposures of the observation are shown in blue.

The polarimetry results for HD14069 observed with the PG0900 grating are shown in Figure 5.13 in the same format as previously. Compared to the PG0300 grating results in Figure 5.7, much larger scatter in the raw (un-binned) P_Q and P_U results is evident. The trend-line of these raw plots also clearly indicate the oscillating systematic errors present in the data. The binned results mostly averages-out these oscillations at shorter wavelengths, but systematics due to the "ripple" remain evident for P_Q above ∼ 5500Å. The overall trend of P_Q starting close to zero in the blue and peaking at ∼ 5700Å seen in the PG0300 grating results remains while the trend for P_U starting negative and increasing towards longer wavelengths is even more pronounced in this case. The linear polarisation P_L results show higher polarisation on average with peaks at 0.4%, although the large variation with wavelength is likely attributable to the oscillating systematic error. This error also clearly impacts on the estimation of the position angle with large deviations seen at 5000Å and again beyond 6000Å. Excluding these, the PA seems to follow the trend seen in the PG0300 case, starting at negative ∼110°

and increasing towards 150° at 6000Å.

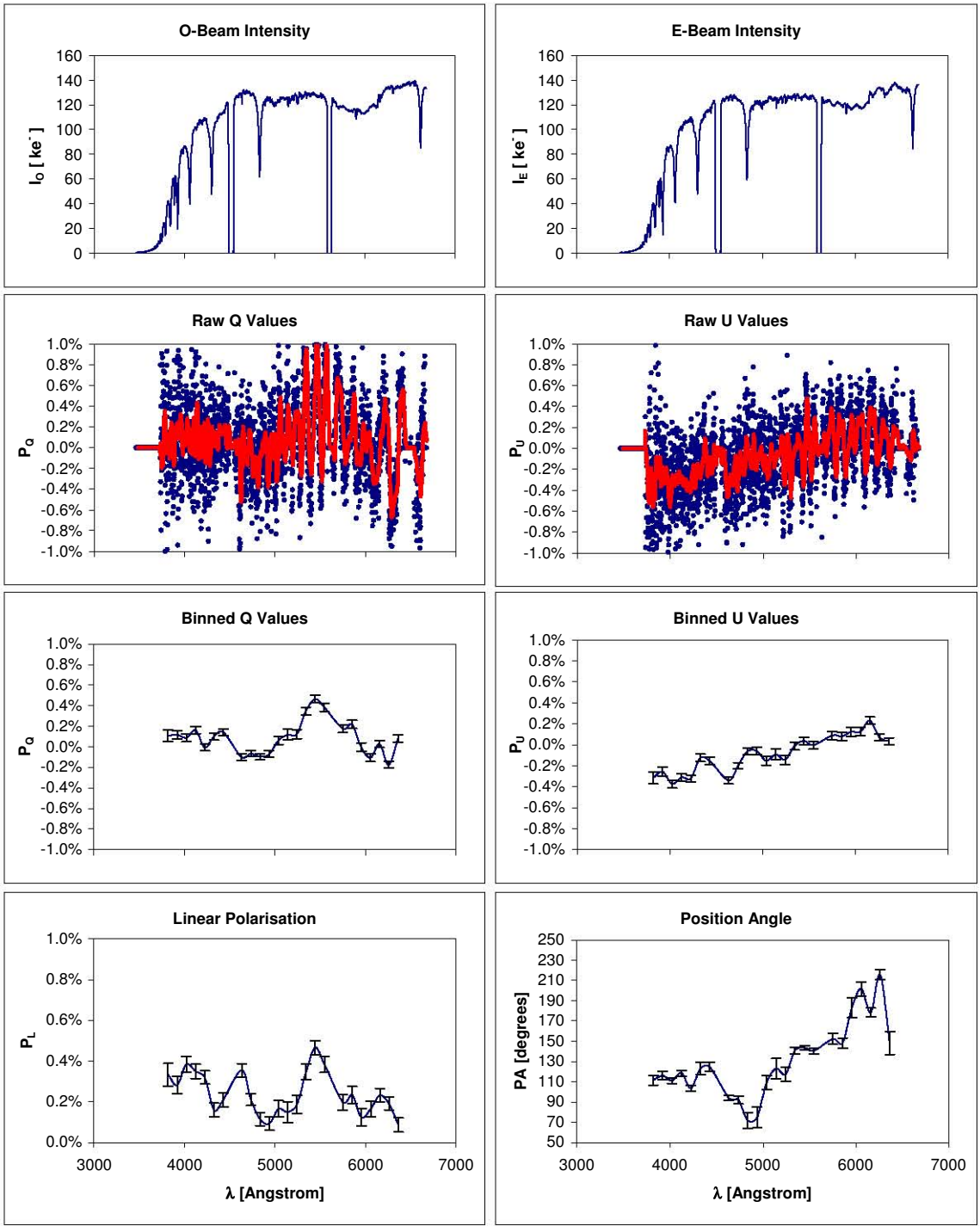

Figure 5.13: HD14069 linear polarisation parameters (PG0900 grating, blue coverage).

The weighted-mean values for the polarisation parameters from this data set are listed in Table 5.5. These are similar within errors to the PG0300 grating case, with an average linear polarisation of $0.24 \pm 0.04\%$.

$\mathbf{P_Q}$	$\mathbf{P_U}$	$\mathbf{P_L}$	**PA**
$0.07 \pm 0.04\%$	$-0.08 \pm 0.04\%$	$0.24 \pm 0.04\%$	$129.2 \pm 5.5°$

Table 5.5: HD14069 weighted-mean values of the polarisation parameters (900 grating, blue coverage).

HD14069: PG0900 grating, red coverage

Extraction results for HD14069 observed with the PG0900 grating and an articulation angle of 40° covering the red end of the spectrum (6000Å to 9000Å) are shown in Figure 5.15. The tracker trajectory and effective pupil size plot in Figure 5.14 indicates a similar track to the PG0300 grating case, with a trajectory starting at the periphery in X and approaching the centre, yielding an increase in effective collecting area over the polarimetry sequence. High frequency variations in the raw spectra from 8000Å and longer wavelengths (over and above the absorption features) are caused by fringing of the detector due to monochromatic sky illumination. Some systematic error is present starting at $\sim$ 2% at the blue end and decreasing to zero near the first detector-gap at $\sim$ 7000Å (see Figure 5.15). An increase in the scatter of the systematic error above 8000Å as as result of the fringing is evident. The systematic error in the blue is also reflected by large extraction errors relative to the rest of the spectrum and clipping by the data-quality vectors in the same region for both O- and E-beams. Again the systematic error arises from a slowly varying wavelength-dependent deviation remaining between the spectra of each beam after normalisation. No other serious systematic or extraction problems are evident and notably the oscillating intensity seen in the blue PG0900 grating data is not present.

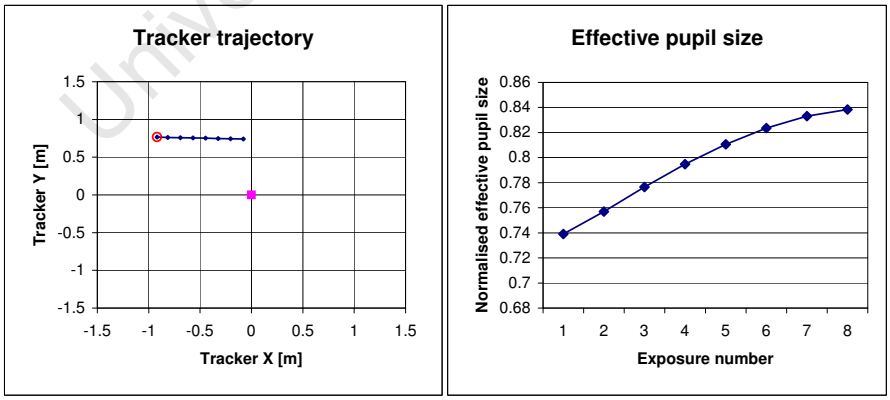

Figure 5.14: Observation trajectory and effective pupil size (left and right panels, respectively) for HD14069 (PG0900 grating, red coverage).

The E/O beam efficiency ratio for this observation is indicated in Figure 5.16. The

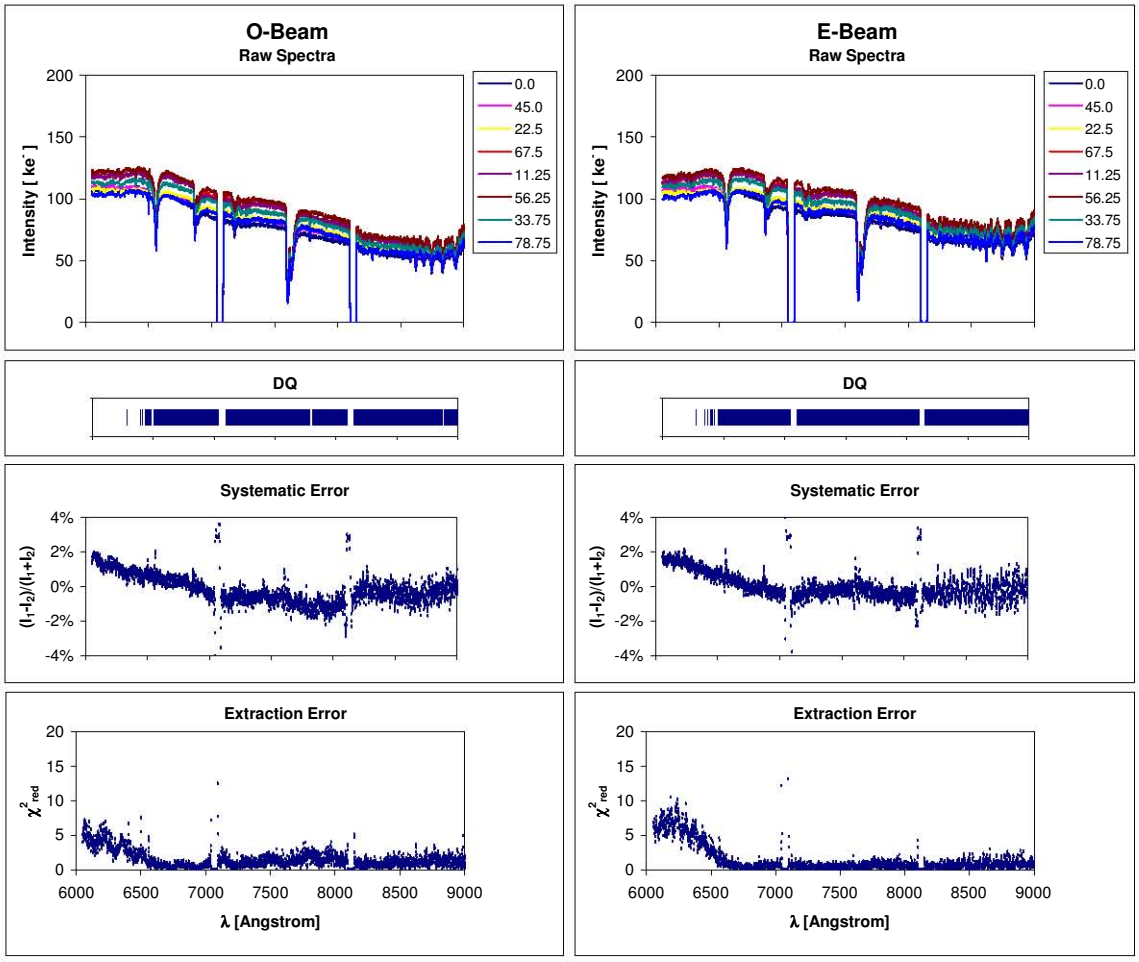

Figure 5.15: HD14069 extraction results for O and E beam (PG0900 grating, red coverage). Data clipping is evident below ∼6500Å due to large χ^2 extraction errors in this region relative to the rest of the spectrum.

increased efficiency of the E-beam in the red part of the spectrum is clearly visible with the ratio increasing monotonically with wavelength and peaking at ∼1.2 at 9000Å. Larger scatter above ∼8000Å due to detector fringing is also evident. Again, deviation of the ratio between exposures (indicated in blue above and below the graph) is small, indicating little or no variation as a function of waveplate angle as expected for an unpolarised target.

Polarimetry results for the red coverage of HD14069 are shown in Figure 5.17, where the scatter of the raw P_Q and P_U values is less than that seen in the blue coverage results. The binned results indicate values close to zero and slightly negative across

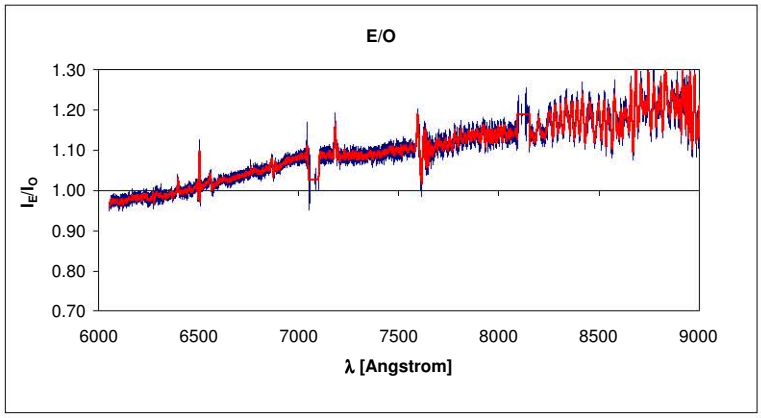

Figure 5.16: Average E/O beam intensity ratio for HD14069 (PG0900 grating, red coverage). Blue error bars above and below the plot indicate the 1-σ deviation level between exposures of the waveplate sequence.

the spectrum for both P_Q and P_U, resulting in total linear polarisation below 0.2% over most of the wavelength range. As may be expected, the low level of polarisation results in a fairly unreliable estimation of the position angle, but a significantly more negative value is estimated compared to the previous cases. Weighted-mean values for the polarisation parameters over the 6000-9000Å wavelength range are listed in Table 5.6. These indicate smaller errors than the blue data set and a change in sign of P_Q to a slight negative value, leading to a shift in PA to an average value of 84.4°, with an uncertainty of ±8.9°.

$\mathbf{P_Q}$	$\mathbf{P_U}$	$\mathbf{P_L}$	**PA**
$-0.05 \pm 0.03\%$	$-0.11 \pm 0.03\%$	$0.14 \pm 0.03\%$	$84.4 \pm 8.9°$

Table 5.6: HD14069 weighted-mean values of the polarisation parameters (900 grating, red coverage).

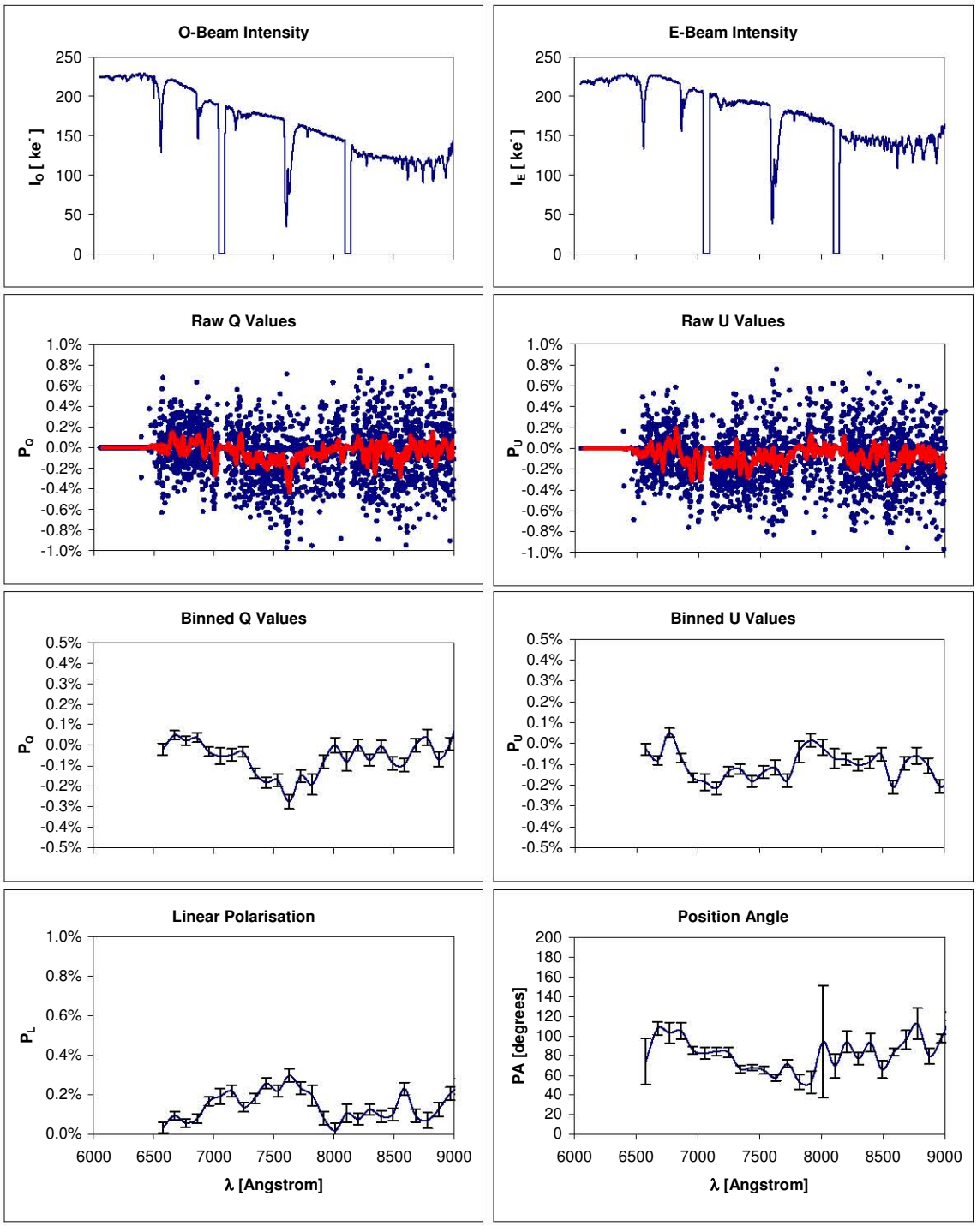

Figure 5.17: HD14069 linear polarisation parameters (PG0900 grating, red coverage).

HD14069: PG0300 grating, off-axis

In this section results from two observations of HD14069 using the PG0300 grating are compared to the original observation discussed above. In this case the observations were performed with the target offset 1.5 arc minutes in the spatial axis along the slit to the North and South in the field from the normal on-axis case.

The two observations were performed subsequent to each other as part of the same telescope track. Figures 5.18 and 5.19 indicate a tracker trajectory starting at the periphery in X and 770 mm in Y, moving towards the centre in X and slightly more peripheral in Y (increasing the effective pupil size), reaching 1 m in Y by the end of the first polarimetry sequence (+1.5 arc minute offset observation) and moving further towards the periphery (decreasing pupil size) during the second sequence (-1.5 arc minute offset observation).

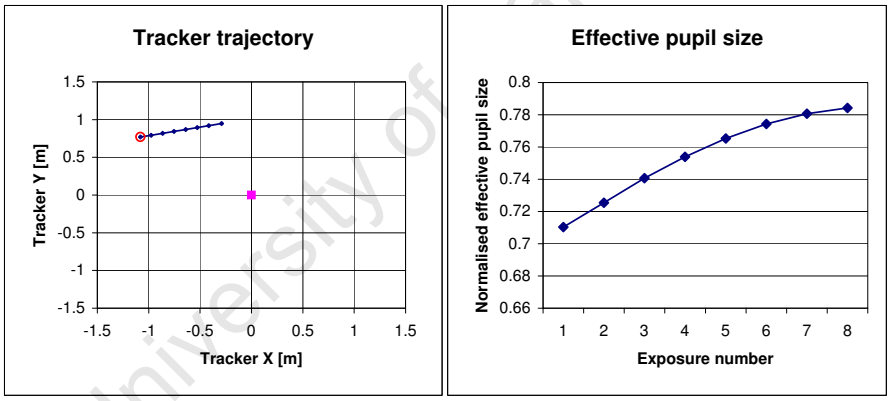

Figure 5.18: Observation trajectory and effective pupil size (left and right panels, respectively) for HD14069 (PG0300 grating, +1.5 arc-minutes off-axis).

Extraction results for the +1.5 arc minute offset observation are shown in Figure 5.20, where varying slit losses due to suboptimal guidance are clear for the first ($\phi = 0°$) and second ($\phi = 45°$) exposures of the sequence (significant drifting in the spectra was observed in the spatial direction during spectrum extraction). Some smaller random variations in intensity remain evident for subsequent exposures, leaving the first and second frame at significantly higher and lower intensity than the rest. After normalisation a slowly varying systematic error of $\sim 2\%$ amplitude over the wavelength

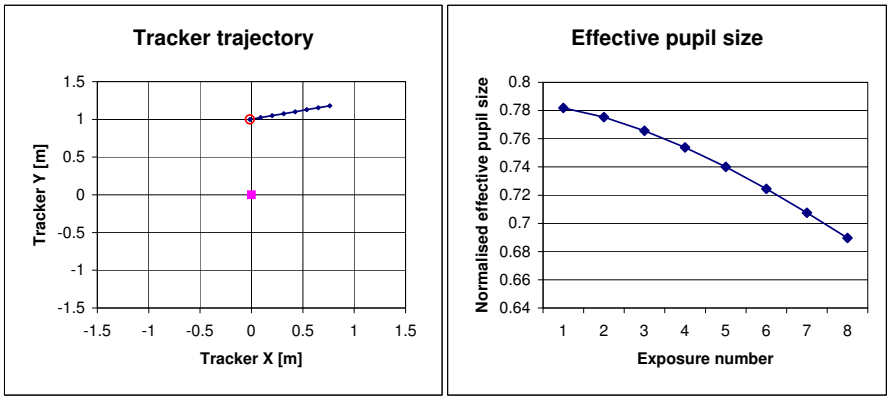

Figure 5.19: Observation trajectory and effective pupil size (left and right panels, respectively) for HD14069 (PG0300 grating, -1.5 arc-minutes off-axis).

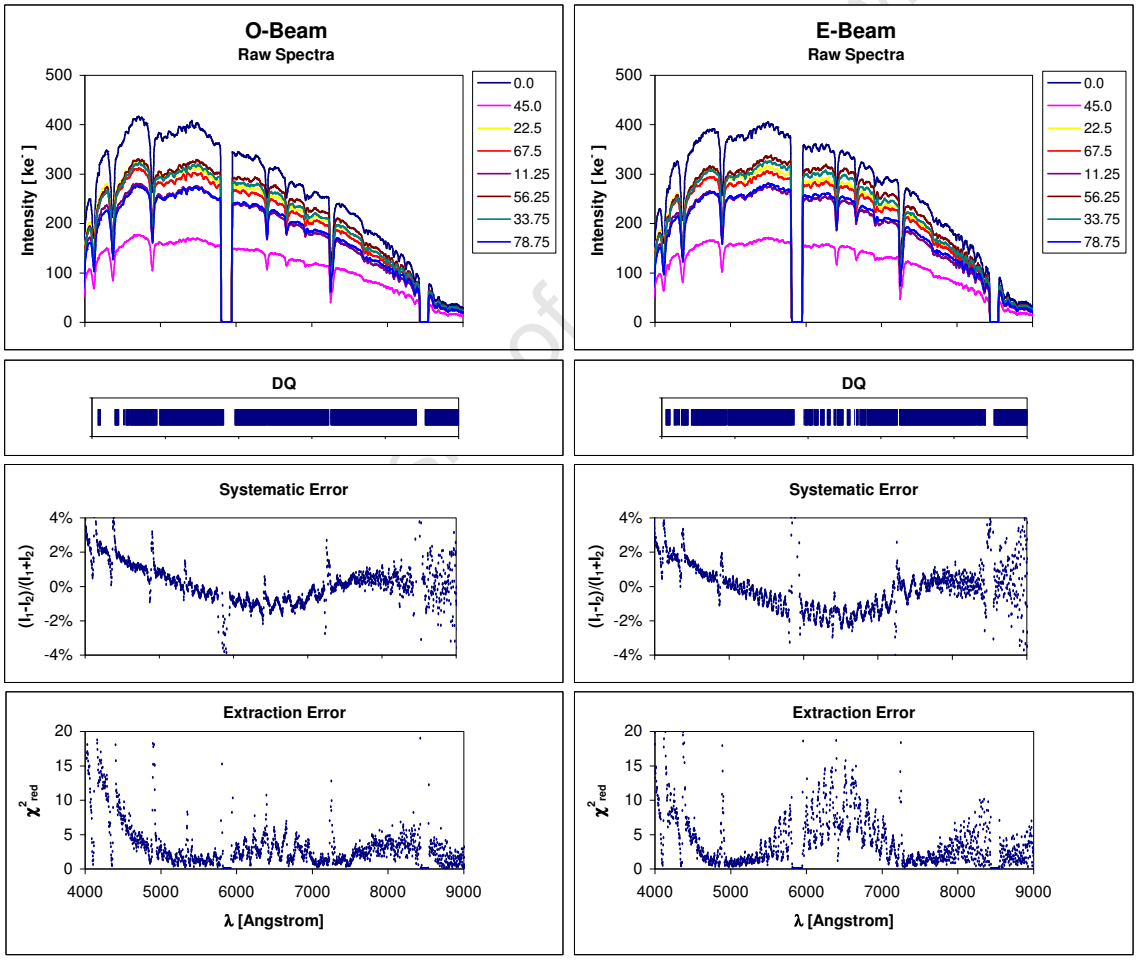

Figure 5.20: HD14069 extraction results for O and E beam (PG0300 grating, +1.5 arc-minutes off-axis).

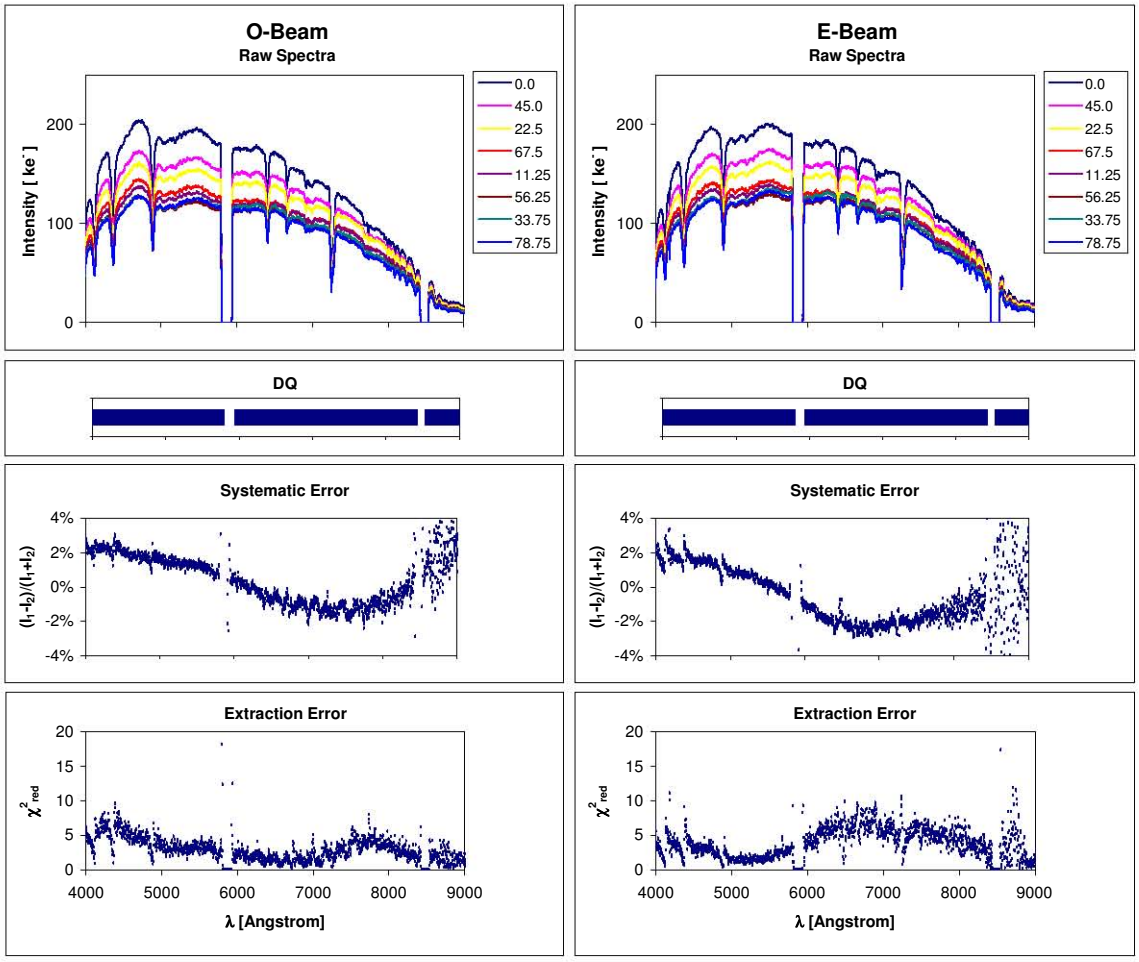

Figure 5.21: HD14069 extraction results for O and E beam (PG0300 grating, -1.5 arc-minutes off-axis).

range remains for both O- and E-beams. This systematic error is similar in shape, but more pronounced, to that seen in the on-axis case (possibly due, in part, to the larger intensity variation of the raw spectra between exposures). Some evidence of the high-frequency error seen in the blue coverage of the PG0900 grating seems to be present at most wavelengths in the raw spectra of this data set as well, although to a lesser extent. These errors result in correspondingly large extraction errors as shown in the bottom panels of Figure 5.20, including significant variations due to the high-frequency error component.

The decreasing pupil size shown in Figure 5.19 is evident in the raw spectra of the -1.5 arc minute offset observation (top panels, Figure 5.21) as the track progresses towards

the periphery of the envelope. A similar systematic error is present, but with the high-frequency error less prevalent than in the +1.5 arc-minute case. This is echoed in less abrupt variations of the extraction error, which is also generally less severe in this case, seemingly consistent with less variation between the intensities of the raw spectra. Comparing these intensities to those of the +1.5 arc-minute offset case it is clear that while the range of effective pupil sizes are similar for each, the intensity of the spectra in the -1.5 arc-minute case is nearly halved. This points to additional varying losses in the system. During image preparation it was noted that the telescope focus continuously deteriorated during the track and could thus be the cause for steadily increasing slit-losses during these two observations.

Similar E/O beam intensity ratio's for the +1.5 and -1.5 arc-minute offset observations are shown in Figures 5.22 and 5.23, respectively, indicating an efficiency profile comparable to the on-axis case. In both cases the E-beam starts less efficient in the blue and increases to ∼10% more efficient at 6500Å. The blue "error bars" indicate a median 1-σ deviation of this ratio between the exposures of each observation of ∼2.3% and ∼2.5%, for the +1.5 and -1.5 arc-minute offset observations, respectively. These values still seem consistent with the small deviation expected when observing an unpolarised standard, but are larger than that seen in the on-axis case. In the +1.5 arc-minute case, this seems to be caused by the "ripple" that causes variations in the raw spectra from one exposure to the next and in the -1.5 arc-minute case also due to generally more noisy data from fainter raw spectra.

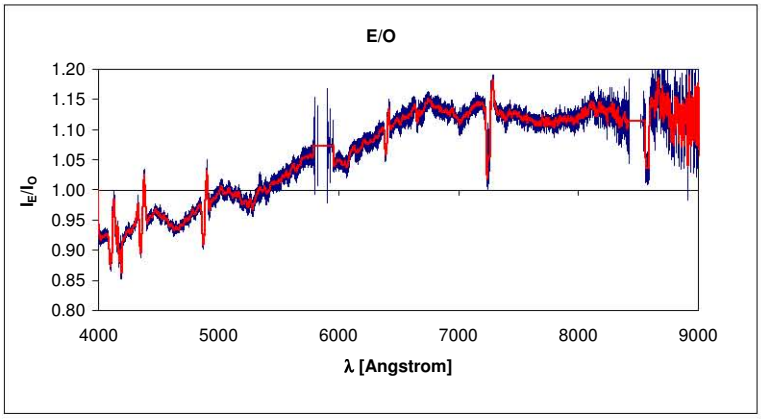

Figure 5.22: E/O beam intensity ratio for HD14069 (PG0300 grating, +1.5 arc-minutes off-axis). Dark blue bands indicate 1-σ deviation over the exposure sequence.

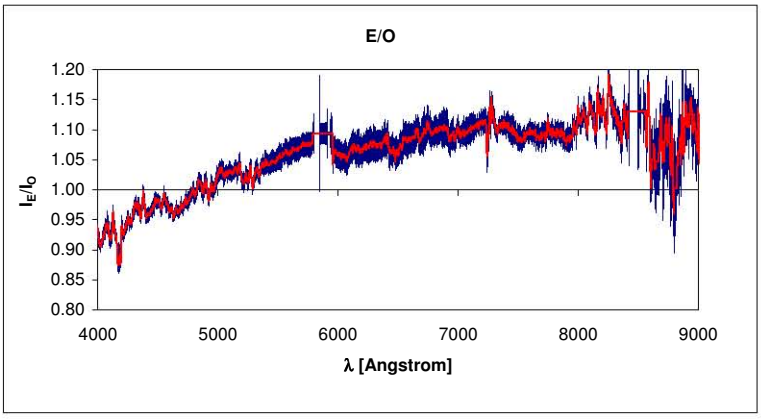

Figure 5.23: E/O beam intensity ratio for HD14069 (PG0300 grating, -1.5 arc-minutes off-axis). Dark blue bands indicate 1-σ deviation over the exposure sequence.

Polarimetry results for the +1.5 arc-minute and -1.5 arc-minute offset observations of HD14069 are shown in Figures 5.24 and 5.25, respectively. For both observations scatter of the raw P_Q and P_U values is not too excessive, although some evidence of a high-frequency systematic error is present - especially in the +1.5 arc-minute offset case.

In the +1.5 arc-minute offset results, P_Q is similar within errors to the on-axis case, peaking at 0.2% near 5500Å, but otherwise remaining close to zero. Compared to the on-axis case, P_U has changed sign to +0.2% in the blue, decreasing in the red. The peak at 6600Å seems spurious, caused by the oscillating systematic errors. This change in P_U results in a shift in PA to $\sim$170° over most of the wavelength range (compared to a lower PA in the on-axis case). Linear polarisation remains low, but peaks higher than the on-axis case with P_L at 0.4% near 5600Å. Weighted-mean values for the polarisation parameters from this data set are listed in Table 5.7. These indicate similar errors to the on-axis data set and a change in sign of P_U to +0.2%, leading to a shift in the position angle to 171.4±4.6°, compared to 123.3±4.6°. The average linear polarisation is similar within errors to the on-axis case at 0.24±0.03%, compared to 0.17±0.02%.

$\mathbf{P_Q}$	$\mathbf{P_U}$	$\mathbf{P_L}$	**PA**
$0.10 \pm 0.03\%$	$0.20 \pm 0.03\%$	$0.24 \pm 0.03\%$	$171.4 \pm 4.6°$

Table 5.7: HD14069 weighted-mean values of the polarisation parameters (300 grating, +1.5 arc-minutes off-axis).

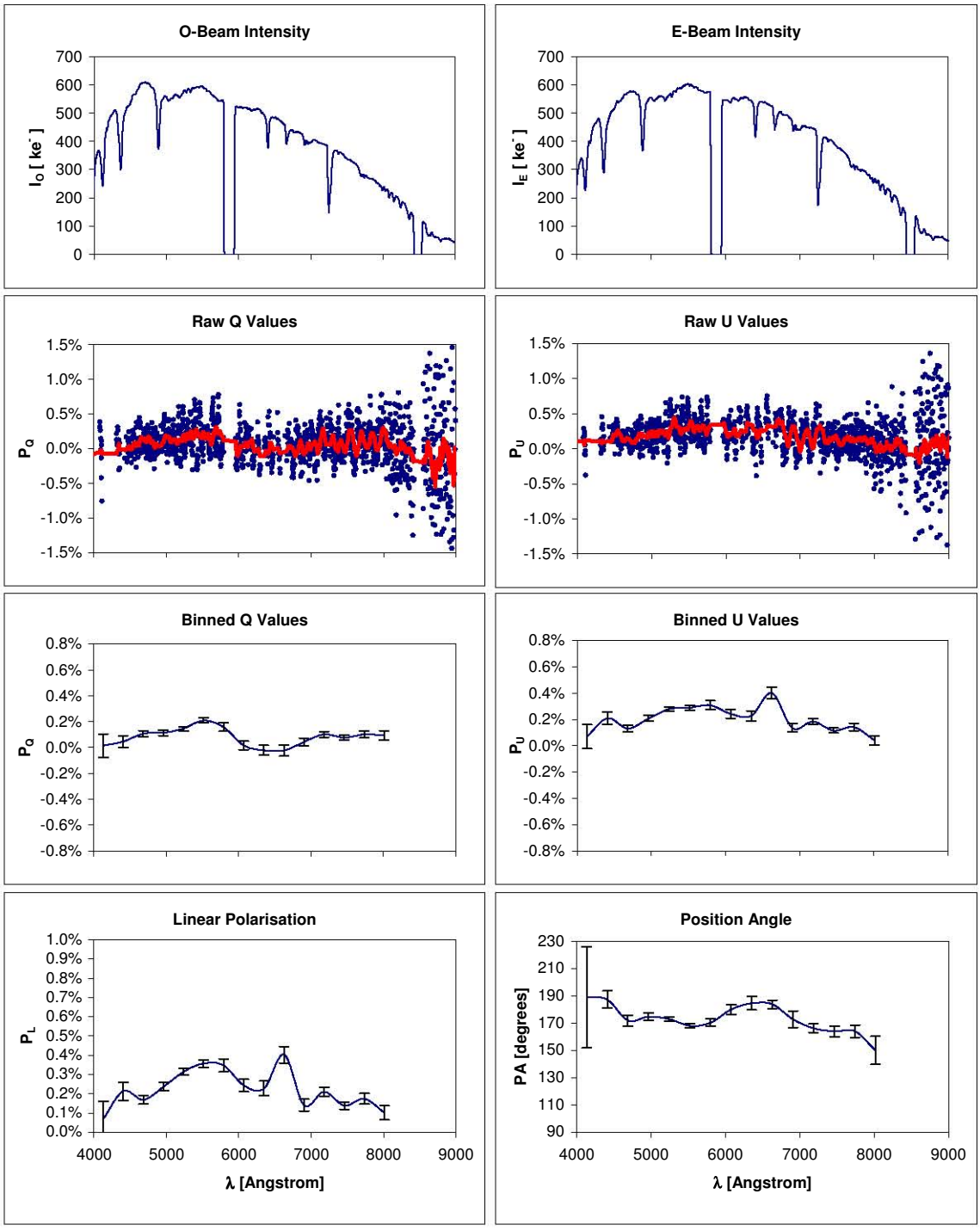

Figure 5.24: HD14069 linear polarisation parameters (PG0300 grating, +1.5 arc-minutes off-axis).

In the -1.5 arc-minute offset results, both P_Q and P_U seem markedly different from the on-axis case, with P_Q shifted higher, averaging close to 0.4%. The trend in P_U is even more pronounced ranging from -0.3% at the blue end to +0.4% in the red. This translates to a fairly constant linear polarisation of $\sim 0.4\%$ over the wavelength range, while the position angle is shifted more positive and echoes the trend in P_U, starting at $\sim$130° and peaking near 160° in the red. The weighted-mean values of the polarisation parameters from this data set are listed in Table 5.8. These indicate a more pronounced average P_L than the on-axis data set (0.45±0.04% compared to 0.17±0.02%), while the position angle is shifted somewhat more positive (142.7±2.7° compared to 123.3±4.6°).

$\mathbf{P_Q}$	$\mathbf{P_U}$	$\mathbf{P_L}$	**PA**
$0.38 \pm 0.04\%$	$0.03 \pm 0.04\%$	$0.45 \pm 0.04\%$	$142.7 \pm 2.7°$

Table 5.8: HD14069 weighted-mean values of the polarisation parameters (300 grating, -1.5 arc-minutes off-axis).

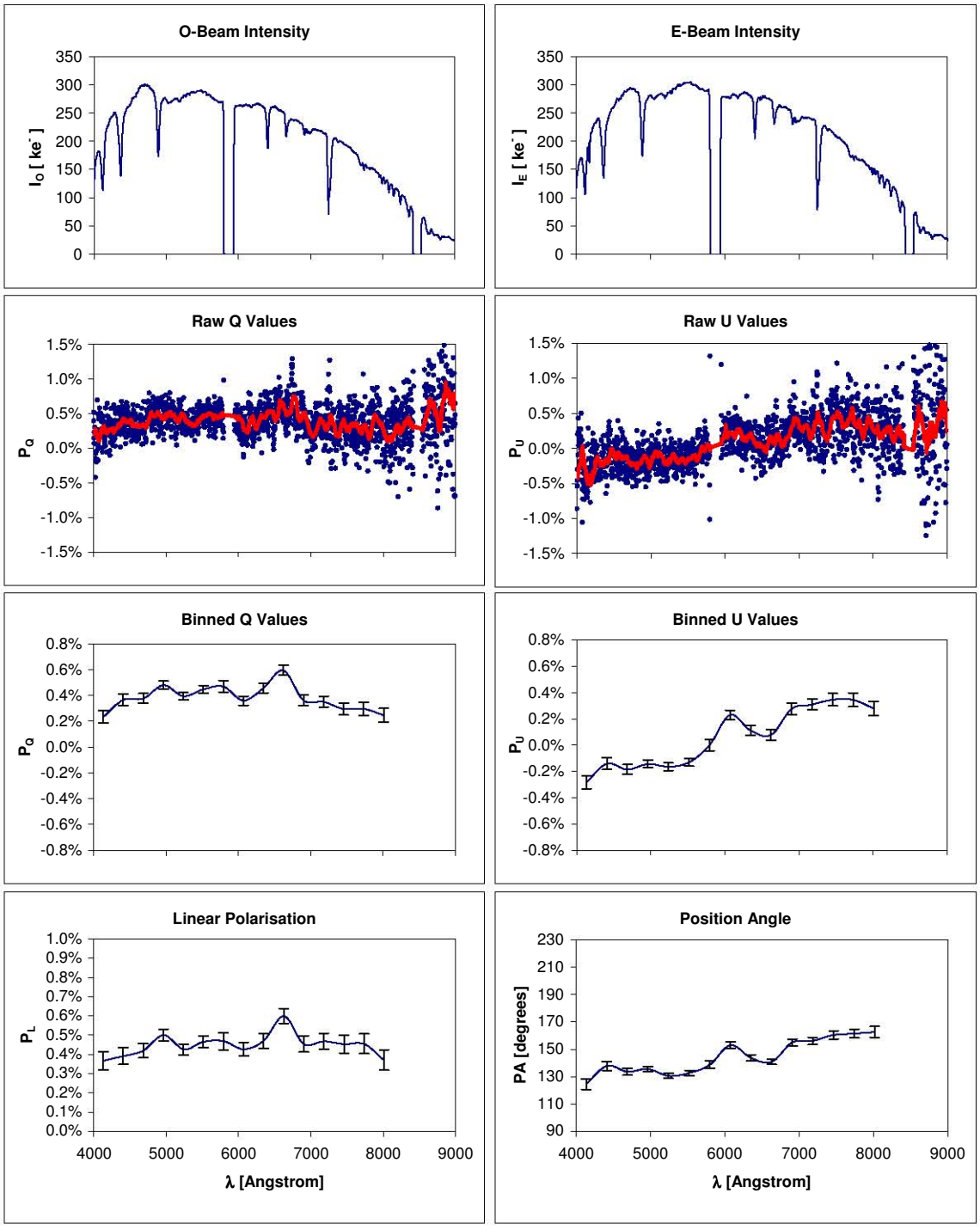

Figure 5.25: HD14069 linear polarisation parameters (PG0300 grating, -1.5 arc-minutes off-axis).

Comparison with HD12021

In this section an observation of the unpolarised standard star HD12021 using the PG0300 grating at an articulation angle of 13° is analysed and the results compared with those obtained for HD14069.

The tracker trajectory shown in Figure 5.26 indicates a track starting near the centre, moving towards a more extreme Y location during the exposure sequence, leading to a decrease in effective collecting area. This is reflected in the steady decrease in average intensity of the raw spectra shown in the top two panels of Figure 5.27. After normalisation a slowly varying systematic error remains for both the O- and E-beam, reaching $\sim +2\%$ and $\sim -2\%$ at the blue and red wavelength extremes, respectively. The extraction errors also peak at the extremes of the spectra, with an increase in scatter towards the red as the intensity decreases. Significant drift along the slit during the observation combined with deteriorating telescope focus was evident during spectrum extraction in this case. Some contamination from second-order spectra may therefore be included in the higher systematic and extraction errors seen in the red from 6700Å. The residual 1-σ deviation between the intensities of the normalised O+E beam spectra from each exposure is plotted as a function of wavelength in Figure 5.28 and confirms deviations up-to 4% of the average spectrum intensity with peaks at wavelengths consistent with the systematic and extraction errors.

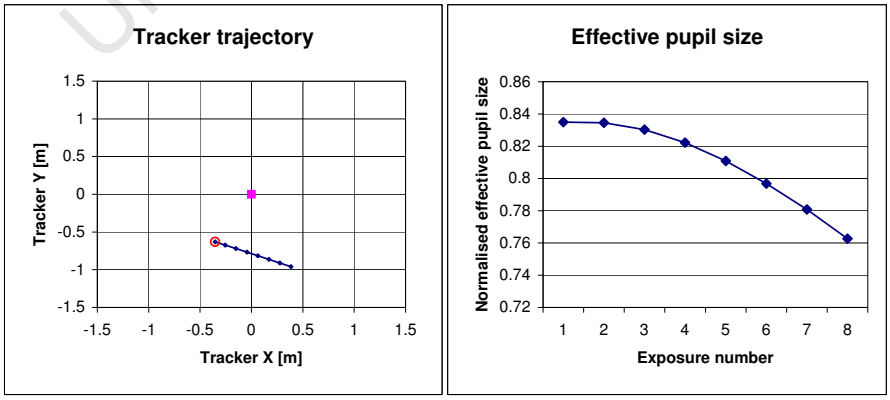

Figure 5.26: Observation trajectory and effective pupil size (left and right panels, respectively) for HD12021 (PG0300 grating).

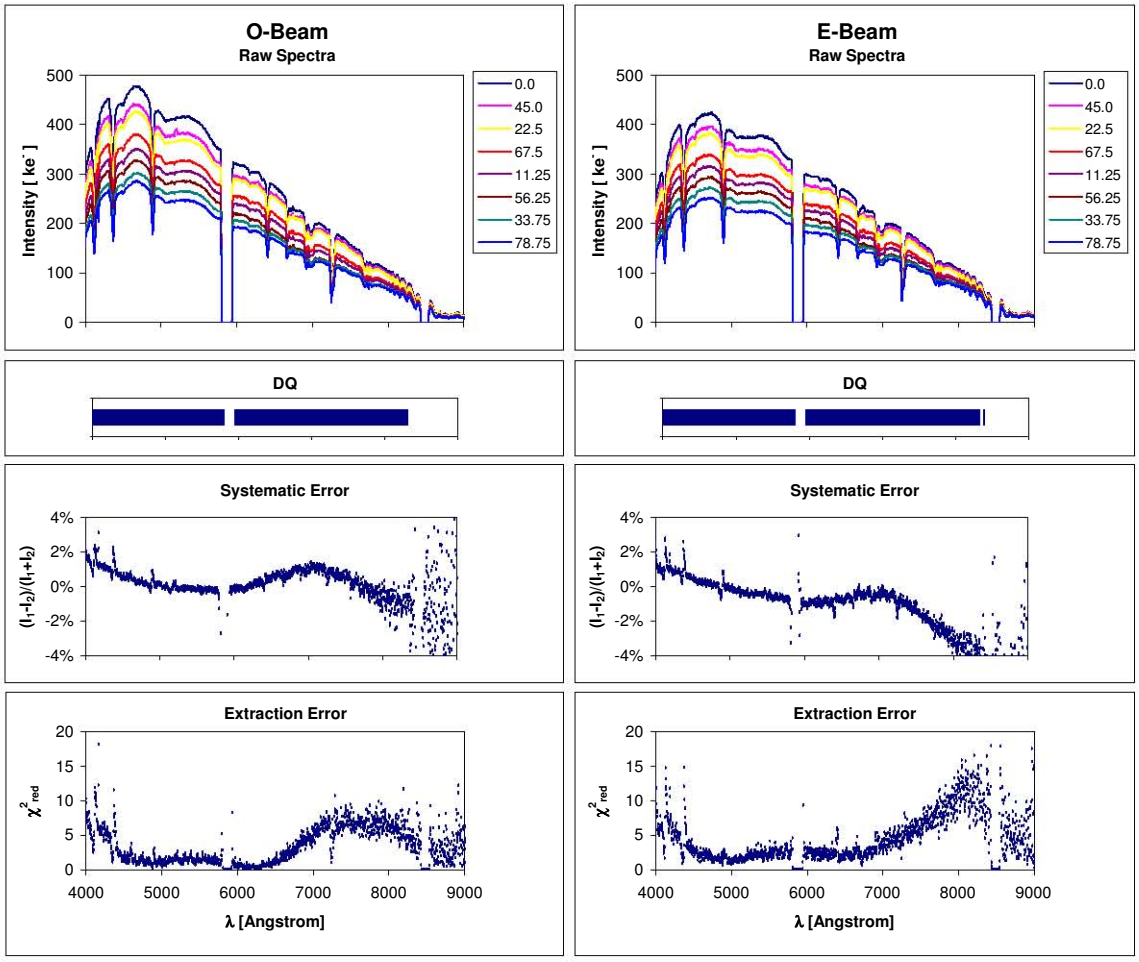

Figure 5.27: HD12021 extraction results for O and E beam (PG0300 grating).

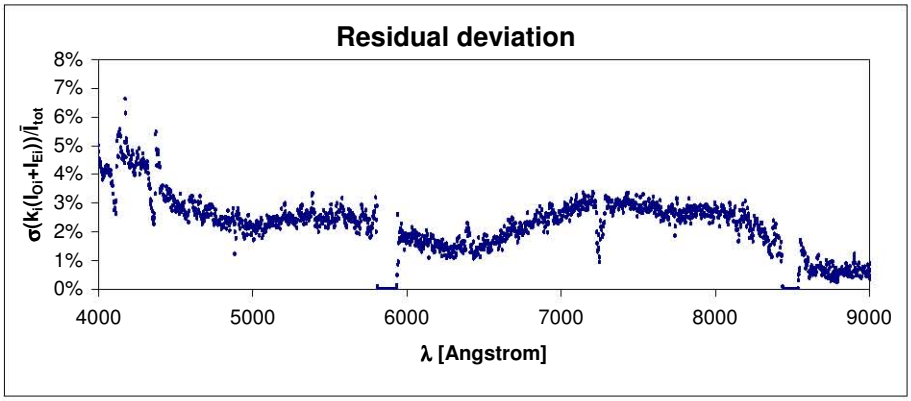

Figure 5.28: Standard deviation of the normalised O+E beam intensity within the set of eight exposures of the waveplate sequence. Data for HD12021 using the PG0300 grating.

The E/O beam intensity ratio as a function of wavelength is shown in Figure 5.29, indicating a similar trend to that seen in the previous PG0300 observations with E/O increasing with wavelength, but with a general shift to lower E-beam efficiency with E/O only reaching unity at ∼6800Å, compared to ∼5000Å previously. Increasing 1-σ deviation levels (indicated in blue) with wavelength seem consistent with the data becoming more noisy as the spectral intensity decreases towards the red.

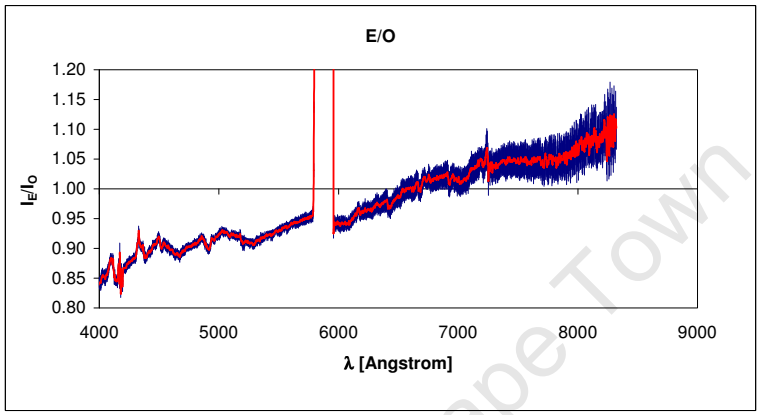

Figure 5.29: E/O beam intensity ratio for HD12021 (PG0300 grating).

The polarimetry results for HD12021 are shown in Figure 5.30, where the scatter of the raw P_Q and P_U values is similar in scale to that seen in the HD14069 on-axis PG0300 grating results (Figure 5.7). P_Q results are similar to that of HD14069 in the blue, averaging around 0.2%, while in the red it becomes more prominent rather than decreasing. P_U follows a more pronounced trend starting at -0.3% in the blue and reaching 0.5% at 8000Å. This translates to a more pronounced linear polarisation in the blue, starting at 0.4%, compared to 0.2% in the HD14069 case. Larger values for P_L towards the red are accompanied by larger errors due to the relatively large extraction errors and fainter spectral intensity in this region. The position angle follows the increasing trend with wavelength dictated by P_U, ranging from ∼125° in the blue to ∼160° in the red.

Weighted-mean values for the polarisation parameters from 4000Å to 6700Å (excluding the range possibly contaminated by second-order spectra) are listed in Table 5.9. These indicate more pronounced values to those in the HD14069 case, with a P_L of

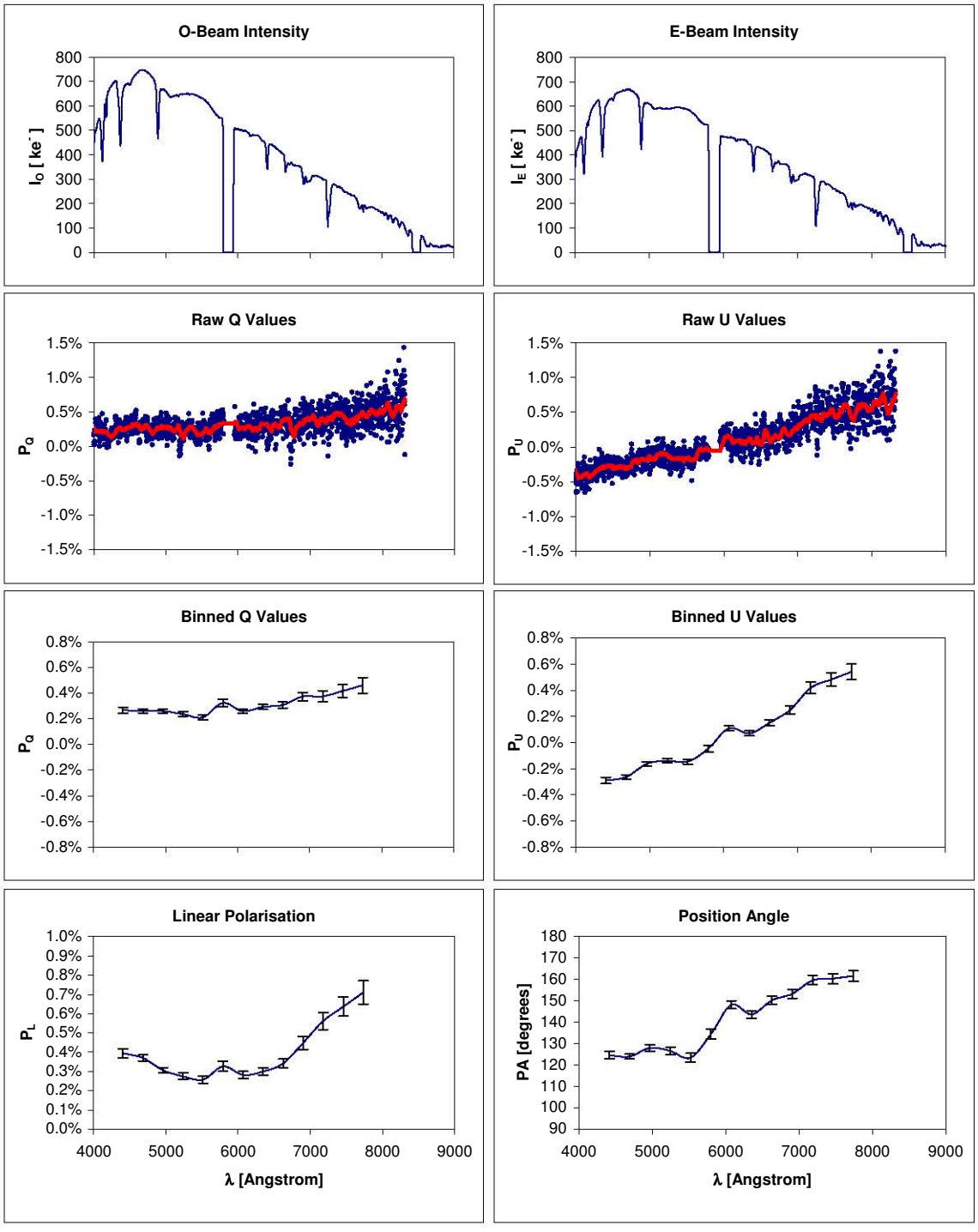

Figure 5.30: HD12021 linear polarisation parameters (PG0300 grating).

0.32±0.02% (compared to 0.17±0.02%) and a shift in average PA to 131.8±1.9° (compared to 123.3±4.6°).

$\mathbf{P_Q}$	$\mathbf{P_U}$	$\mathbf{P_L}$	**PA**
$0.26 \pm 0.02\%$	$-0.11 \pm 0.02\%$	$0.32 \pm 0.02\%$	$131.8 \pm 1.9°$

Table 5.9: HD12021 weighted-mean values of the polarisation parameters (300 grating).

5.3.3 Conclusion

Results from the on-axis observation of the unpolarised standard star HD14069 with the PG0300 grating indicate average values for the instrumental linear polarisation of the combined SALT and RSS over the 4000Å to 9000Å range of 0.17±0.02%, at an average position angle of 123.3±4.6°. The blue coverage PG0900 grating results were contaminated by significant systematic error, while the red coverage results indicate similar instrumental polarisation of 0.14±0.03%, but at a shifted PA of 84.4±8.9°.

Moving the target off-axis in the field by up-to 1.5 arc minutes seems to increase the magnitude of instrumental linear polarisation, with P_L reaching 0.45±0.04% and causes significant shifts in the estimated position angle (reaching 171.4±4.6°).

Comparing the on-axis HD14069 results with those obtained for unpolarised standard star HD12021, indicates a 0.15% higher average linear polarisation for the latter (0.32±0.02%). This seems to indicate that changes in the telescope tracker location alone can have a significant impact on the instrumental polarisation.

The E/O beam intensity ratio for the PG0300 observations consistently indicate a E-beam efficiency starting ∼10% lower than the O-beam at the blue end of the spectrum, increasing to equal efficiency around 5500Å and peaking at ∼10% more efficient in the red. In the HD12021 case the E/O ratio is shifted lower by ∼5%. The PG0900 grating observations indicate a similar trend of increasing E-beam efficiency at longer wavelengths, although with a more efficient E-beam in general with the ratio remaining

at or above unity throughout the blue coverage region.

Changes in effective area and other causes of variation in the total system throughput during a polarimetry sequence seem to aggravate the deficiencies in the normalisation scheme, resulting in more pronounced wavelength-dependent systematic errors. Analysis of the residual deviation in intensity of the normalised O+E spectra of each observation confirms a remaining wavelength-dependent systematic error, with the deviation curve indicative of the reduced-χ^2 extraction errors. An alternative measure of the systematic error is therefore proposed, as outlined in Section 6.2.2.

Extraction artifacts were found including a high frequency wavelength-dependent intensity oscillation at the 1% level indicative of an optical effect. This contamination also varies with time as the telescope track progresses, indicated by the degree of change in this contamination between two subsequent exposures taken with identical RSS configurations as part of the same track (Figures 5.10 and 5.11). This contamination is especially pronounced in the PG0900 grating results with blue wavelength coverage, although some evidence of this is also seen in one of the PG0300 grating data sets.

5.4 Estimation of the position angle correction

This section details results from polarised standard stars in order to verify the accuracy of the reduction methods, the efficiency of the system in detecting linear polarisation and to establish an estimate of the telescope polarimetric position angle offset.

5.4.1 Observations

Two significantly polarised standard stars with known polarisation characteristics from the literature were observed. Vela1 #95 was observed with the PG0900 grating in the red coverage region, while PG0900 data for both blue and red articulation angles were available for HD73882.

5.4.2 Results and discussion

Vela1 #95

The polarised standard Vela1 #95 (see Table 5.2) was observed with the PG0900 grating and articulation angle of 40° providing red coverage from 6000Å to 9000Å. The target was observed while rising during an East-track, as can be inferred from the tracker trajectory shown in Figure 5.31. The track originates close to the centre of the envelope and progresses towards more negative tracker Y, leading to a decrease in effective pupil area as shown in the right-hand panel.

Extraction results are shown in Figure 5.32, where large varying systematic errors are evident. Analysing the intensity deviation of the O+E beam spectra after normalisation again indicates a residual wavelength-dependent deviation consistent with the extraction errors (compare Figure 5.33 with the bottom panels of Figure 5.32).

The E/O beam intensity ratio is plotted in Figure 5.34, where the increasing E-beam efficiency with wavelength is again seen. The total 12.5% 1-σ deviation of the ratio

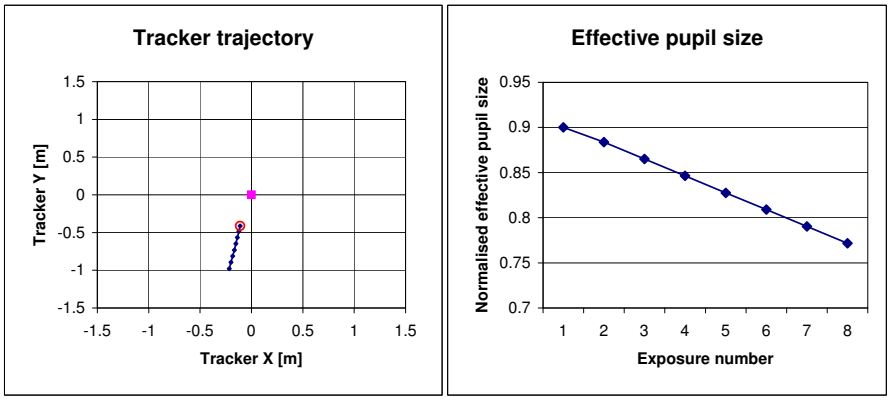

Figure 5.31: Observation trajectory and effective pupil size (left and right panels, respectively) for Vela 1 #95 (PG0900 grating, red coverage).

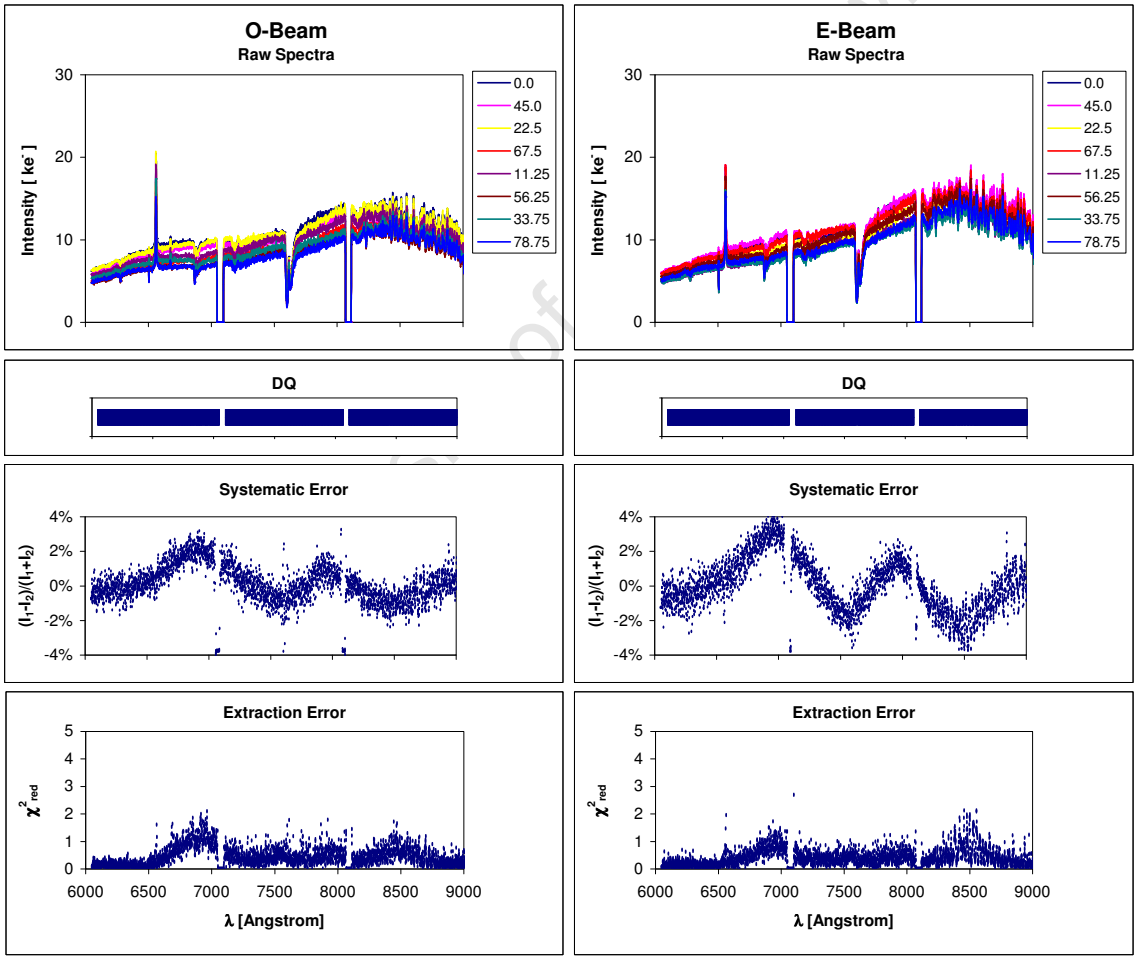

Figure 5.32: Vela 1 #95 extraction results for O and E beam (PG0900 grating, red coverage).

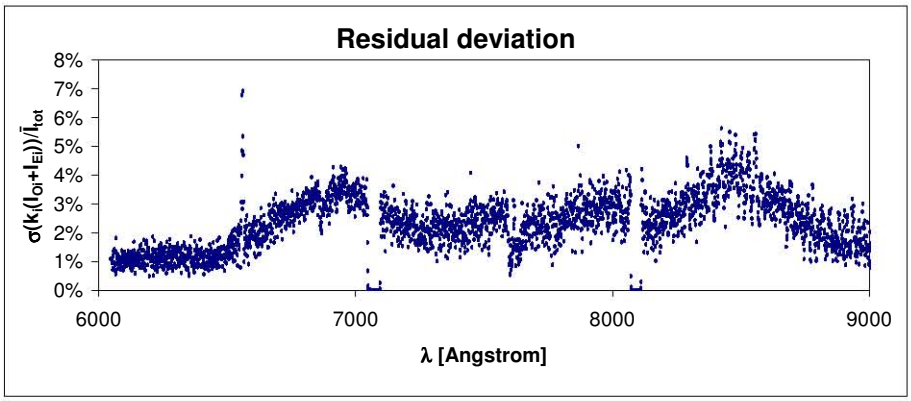

Figure 5.33: Residual standard deviation of the normalised O+E beam intensity within the set of eight exposures of the waveplate sequence. Data for Vela1 #95 using the PG0900 grating.

(indicated in blue) show significant shifts in the ratio between exposures, as would be expected for this highly polarised target.

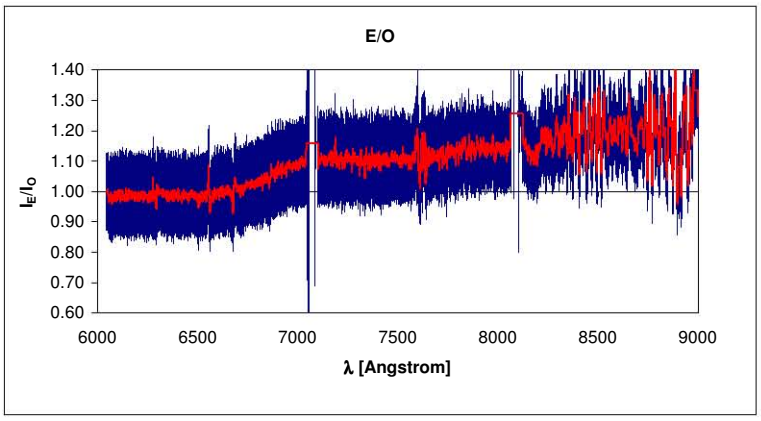

Figure 5.34: E/O beam intensity ratio for Vela 1 #95 (PG0900 grating, red coverage). Blue error bars indicate the 1-σ deviation level of the ratio between exposures in the waveplate sequence.

The polarimetric results obtained for Vela1 #95 are shown in Figure 5.35. The strong polarisation of the target is immediately evident from both raw and binned P_Q and P_U values with P_Q fairly constant at $\sim$ 2.5% over the wavelength range and P_U starting at 7.7% at 6000Å, peaking at 7.8% at 6860Å and then gradually decreasing to 5.7% at 9000Å. This translates to a linear polarisation of 8.1% in the blue, decreasing to 6.4% at 9000Å. The position angle is well defined and fairly constant over the wavelength range

with a weighted-mean value of $172.16 \pm 0.29°$, as listed in Table 5.10. Also shown in the bottom panels of Figure 5.35, are some values for P_L and PA from the literature (Fossati et al., 2007), indicated by $\diamondsuit$. The measured P_L, though slightly higher, agree with the literature to within the measurement errors, confirming the reduction techniques and indicating good linear polarisation efficiency of the system. The PA results shown agree with the reference values to well within the errors. Minimising the least-squares error between a linear fit of the reference data and the measured PA values indicates an average constant offset of only 0.05°. This implies that essentially no telescope position angle correction is required, to within an error of $\pm 0.29°$.

The weighted-mean results shown in Table 5.10 were calculated from 6000Å to 8500Å, coinciding with the overlap of the wavelength coverage of the reference data available from literature. The mean $P_L = 7.53 \pm 0.08\%$ compares well with the average reference value from R and I filters $P_{L_{R+I}} = 7.53 \pm 0.04\%$.

$\mathbf{P_Q}$	$\mathbf{P_U}$	$\mathbf{P_L}$	**PA**
$2.57 \pm 0.08\%$	$7.07 \pm 0.08\%$	$7.53 \pm 0.08\%$	$172.16 \pm 0.29°$

Table 5.10: Vela1 #95 weighted-mean values of the polarisation parameters for the wavelength range 6000Å to 8500Å (PG0900 grating, red coverage). The PA value is listed as determined from the reduction method, without any telescope PA correction applied.

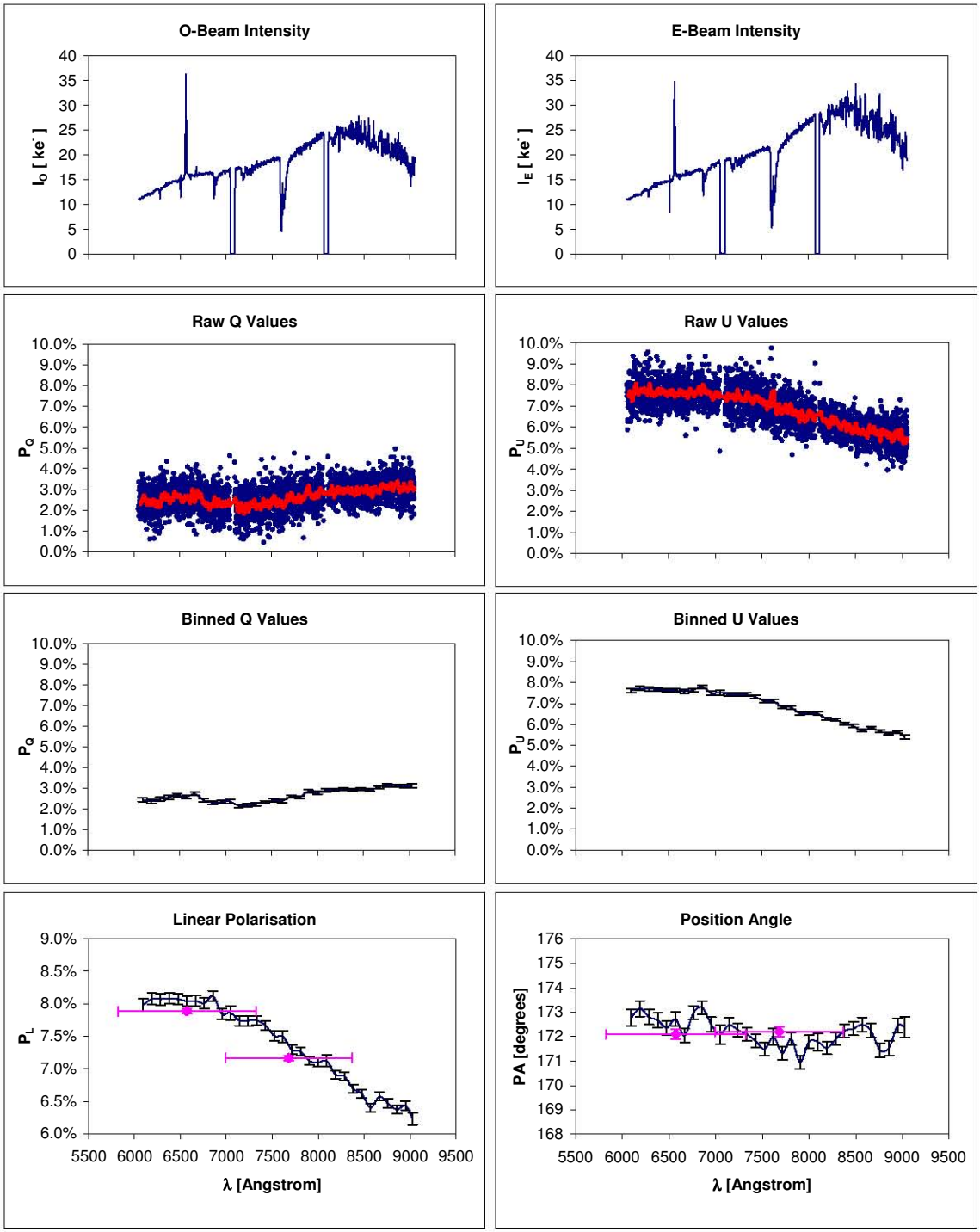

Figure 5.35: Vela 1 #95 linear polarisation parameters (PG0900 grating, red coverage). Data points (indicated by ◊) for the R and I filters from the FORS1 measurements in Figure 5.1 are also shown for reference on the $\%P$ and PA plots. Horizontal error bars for the reference points indicate the full-width-half-maximum of each filter.

HD73882

The polarised standard HD73882 (see Table 5.2) was observed with the PG0900 grating for both blue and red wavelength coverage. Blue and red coverage observations were performed as part of the same telescope track, as seen from Figures 5.36 and 5.37, respectively. The trajectory for the first observation originates close to the centre of the envelope and moves towards more negative Y values. The second observation starts at Y=914 mm and moves further toward to edge of the envelope. The right-hand panels in both figures indicate the decreasing effective collecting area during the track.

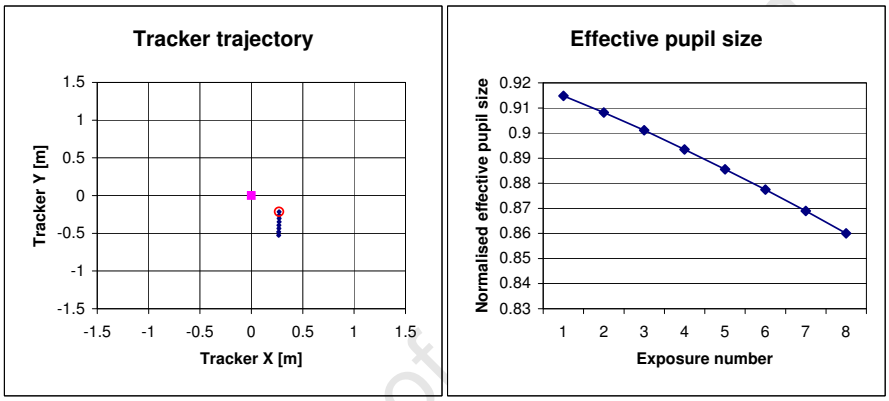

Figure 5.36: Observation trajectory and effective pupil size (left and right panels, respectively) for HD73882 (PG0900 grating, blue coverage).

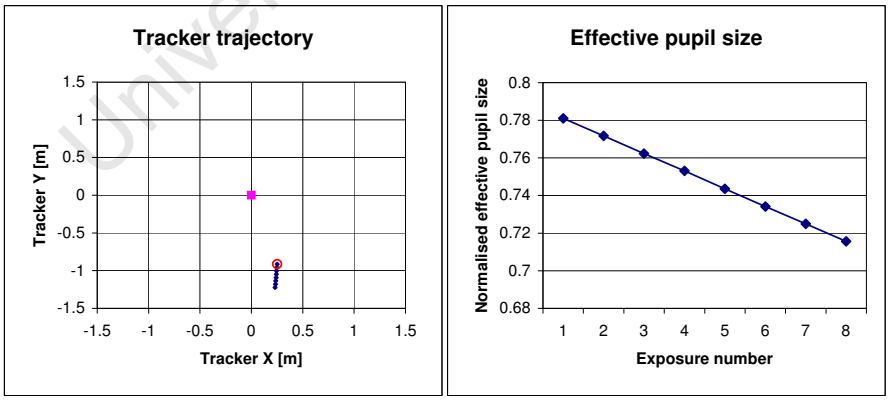

Figure 5.37: Observation trajectory and effective pupil size (left and right panels, respectively) for HD73882 (PG0900 grating, red coverage).

The changes in pupil size from this track remains limited, because of the relatively short duration of each polarimetry sequence using 40-second exposures on this bright

target. The raw spectrum plots are shown at the top rows of Figures 5.38 and 5.43 for the blue and red coverage observations, respectively.

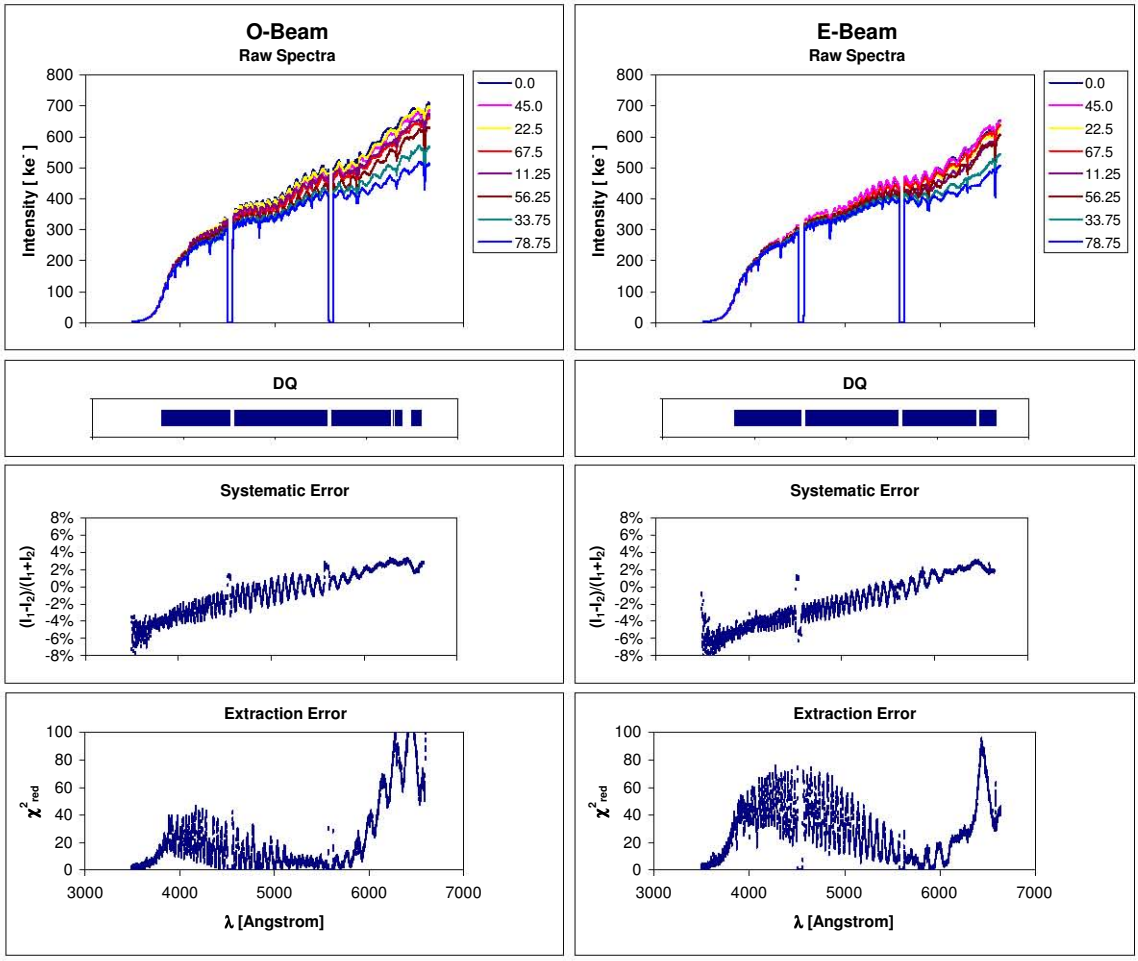

Figure 5.38: HD73882 extraction results for O and E beam (PG0900 grating, blue coverage).

In the blue coverage observation a large monotonically rising systematic error is evident for both the O- and E-beam, emulating the shape if the raw spectra's intensities. Also clearly seen is an oscillating systematic error similar to that seen for the PG0900 grating blue coverage results in the previous section. As before, the "period" of this oscillation is directly proportional to wavelength. The variation of this pattern between exposures causes large extraction errors, especially on the E-beam results. Figure 5.39 show the remaining 1-σ deviation of the normalised spectra (O+E beam combined for each exposure). The correlation of this deviation with the extraction errors shown in

Figure 5.38 is clear, indicating systematics as the main cause for these errors. The normalised O+E beam intensities are plotted in Figure 5.40 and illustrate the differences remaining between the total intensity spectra from different exposures after normalising each with a constant scaling factor as detailed in Section 4.4.2.

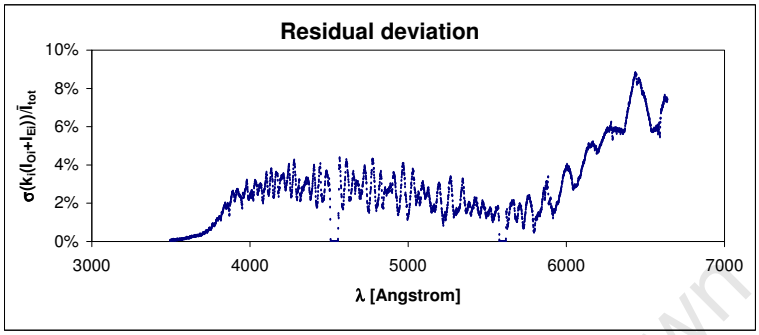

Figure 5.39: Residual standard deviation of the normalised O+E beam intensity within the set of eight exposures of the waveplate sequence. Data for HD73882 using the PG0900 grating, blue coverage.

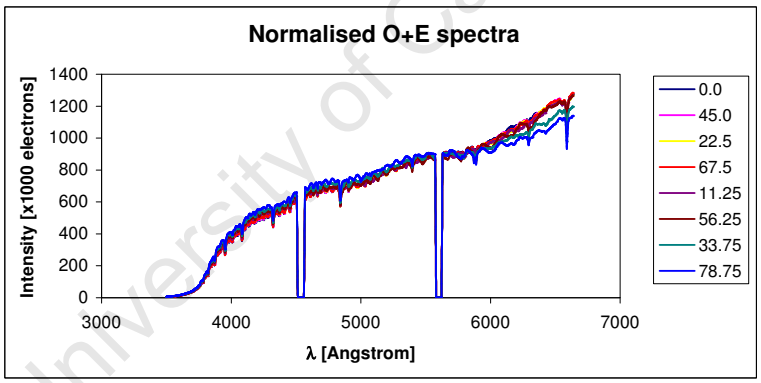

Figure 5.40: Normalised O+E beam spectra, indicating the remaining deviation after normalisation.

The E/O beam intensity ratios for the blue and red coverage observations are indicated in Figures 5.41 and 5.42, respectively. The E-beam is less efficient in the blue and clearly shows the different impact of the oscillating interference on the O and E beam. This interference is less prominent in the red part of the spectrum, which is also reflected in the 1-σ deviation of the ratio over the exposures of 7% and 4%, for blue and red coverage respectively (indicated in blue on the plots). Some shifting of the ratio between exposures is expected, as this is a polarised target.

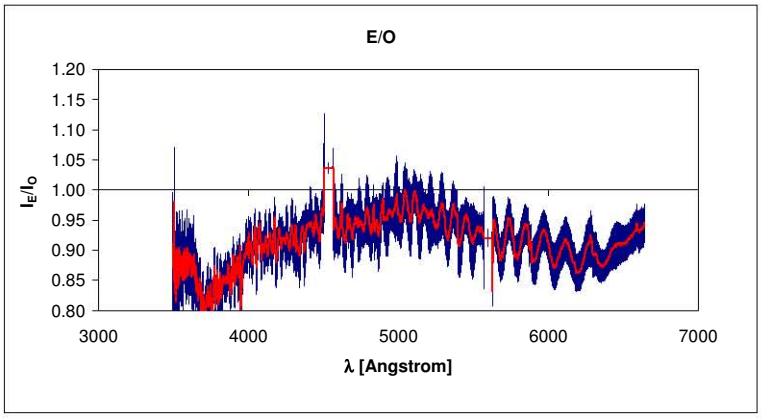

Figure 5.41: E/O beam intensity ratio for HD73882 (PG0900 grating, blue coverage).

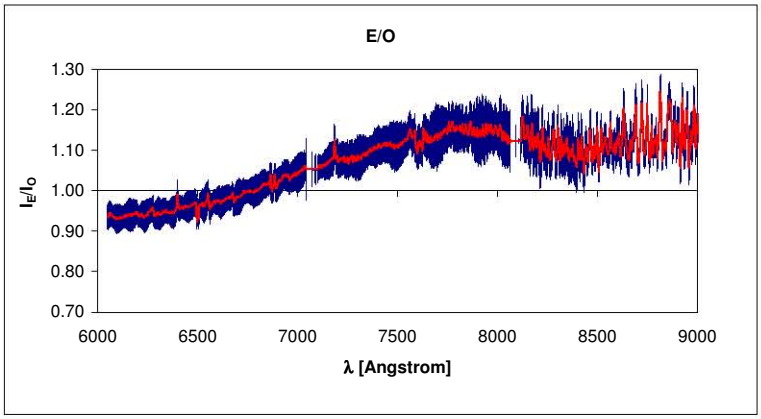

Figure 5.42: E/O beam intensity ratio for HD73882 (PG0900 grating, red coverage).

The extraction results for the red coverage observation in Figure 5.43 shows less systematic error up to $\sim$ 8000Å, although it does increase towards longer wavelengths. In this instance an oscillating error is visible in results for the red coverage as well, clearly influencing the extraction errors. Data at wavelengths longer than $\sim$ 8500Å are excluded by the data-quality vector because of excessive extraction error levels.

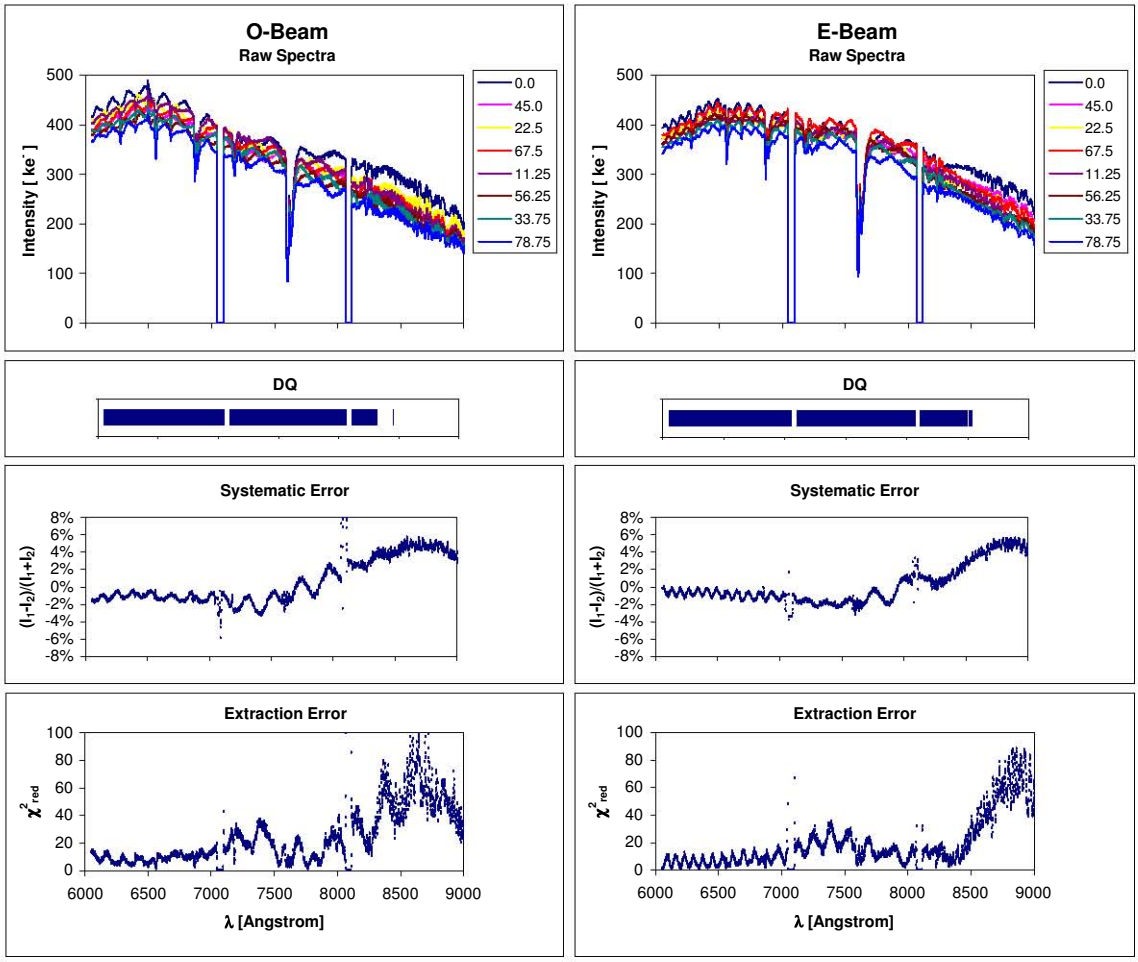

Figure 5.43: HD73882 extraction results for O and E beam (PG0900 grating, red coverage).

Polarimetry results for the blue and red coverage observations of HD73882 are shown in Figures 5.44 and 5.45, respectively. The significantly polarised nature of this target is clearly visible in the results, but the raw P_Q and P_U results show large contamination from an oscillating systematic component that is not always compensated for through binning (a larger binning window of 200 data points was used for this target). This translates into large uncertainties shown by the error bars on the binned plots. The errors for the red coverage results are noticeably smaller than those for the blue coverage plots. In the latter case P_Q starts close to 1% at 4000Å, peaks at 1.5% at 4590Å and remains close to 1% up to 6000Å. P_U starts at 1.1% in the blue and steadily climbs to 1.9% at 6000Å. This results in a fairly flat linear polarisation with P_L between 1.5% and 2% throughout the wavelength range. The values correlate reasonably well with the values from literature (Serkowski, Mathewson and Ford, 1975), indicated by $\diamondsuit$'s in the bottom-left plot of Figure 5.44. In the blue wavelength coverage results the position angle varies between 171° and 166°. This trend compares well to the PA reference values from literature shown in the bottom right-hand panel of Figure 5.44, although a constant offset is evident. In this case minimising the least-squares error between a linear fit of the reference data and the measured values indicates an offset of 4.37±0.6°.

Weighted-mean values for the polarisation parameters from this data set are listed in Table 5.11. These correlate well with the reference data listed in Table 5.2 where $P_L = 2.0\%$.

$\mathbf{P_Q}$	$\mathbf{P_U}$	$\mathbf{P_L}$	**PA**
$1.15 \pm 0.04\%$	$1.56 \pm 0.04\%$	$1.96 \pm 0.04\%$	$168.7 \pm 0.6°$

Table 5.11: HD73882 weighted-mean values of the polarisation parameters (900 grating, blue coverage).

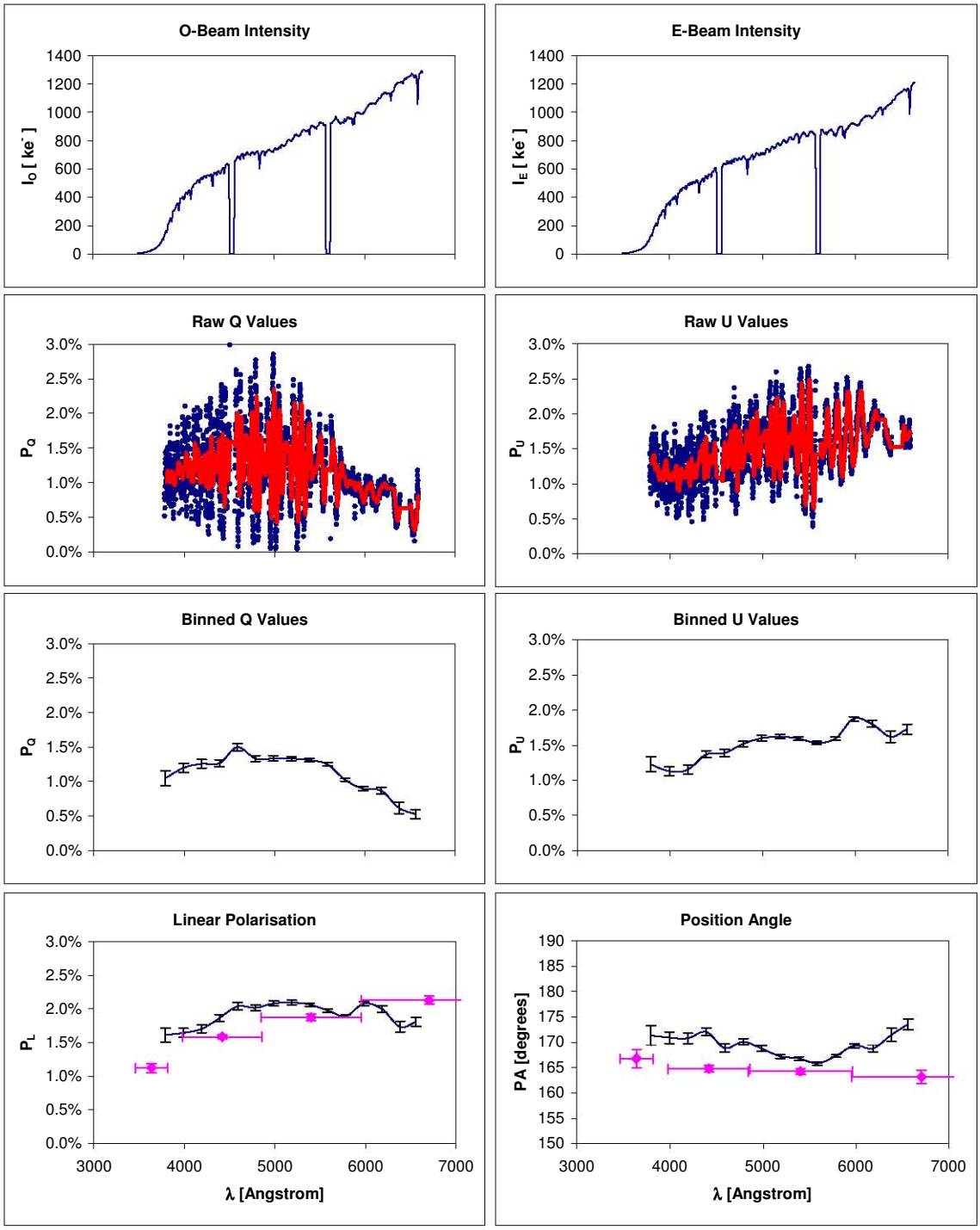

Figure 5.44: HD73882 linear polarisation parameters (PG0900 grating, blue coverage). Data points (indicated by ♢) for the U,B,V and R filters from literature as shown in Figure 5.2 are also indicated for reference on the $\%P$ and PA plots. Horizontal error bars for the reference points indicate the full-width-half-maximum of each filter.

In the red coverage results shown in Figure 5.45, P_Q starts close to 1% at 6000Åand climbs to 1.8% at 8000Å. P_U remains close to 1.7% for all wavelengths. Linear polarisation therefore remains flat into the red coverage range with P_L at ∼2%. A reference value from literature (Serkowski, Mathewson and Ford, 1975) is again plotted showing good agreement. The position angle varies from 165° to 160° and a reference value from literature at 6500Å compares well with these results, leading to an estimated telescope correction of 0.71±0.4°. Weighted-mean values for the polarisation parameters from this data set are listed in Table 5.12.

$\mathbf{P_Q}$	$\mathbf{P_U}$	$\mathbf{P_L}$	**PA**
$1.17 \pm 0.03\%$	$1.67 \pm 0.03\%$	$2.06 \pm 0.03\%$	$164.5 \pm 0.4°$

Table 5.12: HD73882 weighted-mean values of the polarisation parameters (900 grating, red coverage).

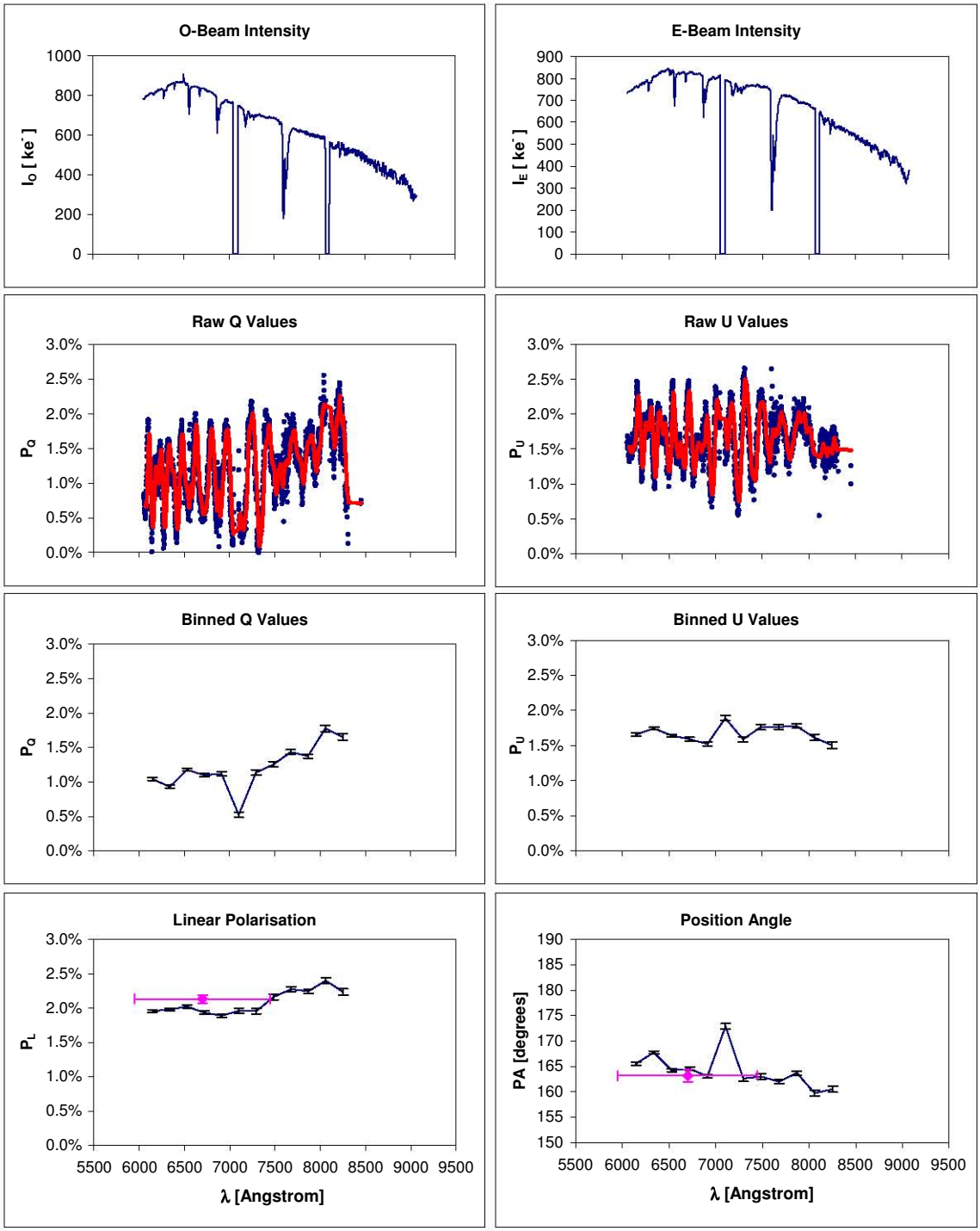

Figure 5.45: HD73882 linear polarisation parameters (PG0900 grating, red coverage). A data point (indicated by ♢) for the R filter from literature as shown in Figure 5.2 is indicated for reference on the $\%P$ and PA plots. Horizontal error bars for the reference point indicate the full-width-half-maximum of the filter.

5.4.3 Conclusion

Applied to the two polarised standards Vela1 #95 and HD73882, the reduction methods developed in this study produce results that agree well with published literature, delivering linear polarimetry parameters that agree with reference values to within 0.16%. This also indicates good system efficiency for detecting linear polarisation. An essentially zero telescope position angle correction was determined from the Vela1 #95 observation within a measurement error of $\pm 0.29°$. In the case of HD73882 the blue results indicate an offset of $-4.37°$, but with larger uncertainty of $\pm 0.6°$ influenced by the significant oscillating systematic error seen in the raw data. The red coverage results, while also influenced by some systematics, show an offset of -0.71$\pm$0.4°.

As in the case of the unpolarised standards, large systematic errors were evident for the polarised standards. A wavelength-dependent normalisation offset is present, directly proportional to the range of intensity of the target spectrum, as confirmed by analysing the remaining deviation of the normalised spectra. An alternative measure of systematic error is therefore proposed (see Section 6.2.2). The same wavelength-dependent intensity oscillation observed in PG0900 grating unpolarised standard data was evident in both the blue and red coverage HD73882 data, severely impacting the systematic and extraction errors.

The E/O beam efficiency ratio results confirms the trend observed for the unpolarised targets, with the E-beam efficiency increasing towards longer wavelengths and peaking at $\sim$10% above the O-beam at 9000Å. Deviation of the E/O ratio between exposures is expected for polarised targets and directly relates to their level of polarisation. This linear relationship was clearly evident. The independent effect of the "ripple" interference on O- and E-beam data was also evident from the propagation of this error to the E/O ratio results, for example in the blue coverage results of HD73882.

Chapter 6

Summary and conclusion

In this study a method for reducing SALT RSS polarimetry data is proposed, including techniques for robustly extracting spectra from the image data and propagating errors via data-quality and variance planes. A method for determining the Q and U Stokes and linear polarisation parameters, as well as their measurement errors, is developed and a new "all-Stokes" waveplate pattern is proposed that eliminates cross-contamination between the Q and V components.

These techniques were successfully verified on observations of unpolarised and linearly polarised standard stars where results were obtained that agree well with published literature. Results from the unpolarised standards produced estimates of the average on-axis instrumental polarisation of the combined SALT and RSS ranging from 0.14±0.03% to 0.32±0.02%, depending on instrument configuration and the observed target. The polarised standard star data were used to estimate a position angle correction value (for converting the obtained PA to equatorial PA) and indicated that essentially no offset is required (-0.05±0.29° in the Vela1 #95 case).

Significant wavelength-dependent systematic errors were evident in many of the data sets, comprising of two main components: a slowly varying component that seems to be related to an imperfect normalisation metric of the raw spectra from the waveplate sequence, and a high frequency "oscillating" component, mainly seen in the PG0900

(900 l/mm) grating data. This latter component is of particular concern as it seems to be time (or telescope tracker position) dependent, in addition to other factors such as the selected grating and the dispersion angle. The wavelength-dependent nature of this "ripple" seems to suggest that an optical effect may be the cause and may therefore indicate a possible interference effect from a plane-parallel optical element, such as a filter, VPH grating cover or even a multi-layer coating. An air bubble in the coupling fluid of the Wollaston prism was subsequently discovered and corrected, likely eliminating this issue in future observations.

The E/O beam efficiency exhibits a fairly consistent global trend with the E-beam becoming more efficient towards longer wavelengths, but significant smaller-level variations are present from one observation to another, depending on instrument configuration and possibly other factors such as telescope tracker position and the target's polarisation position angle.

A more detailed summary of the results is presented below.

6.1 Summary of results

From the unpolarised standard star results an average value for the combined instrumental linear polarisation for SALT and RSS was found ranging from $P_L = 0.14 \pm 0.03\%$ to $P_L = 0.45 \pm 0.04\%$. The position angle of this polarisation was found to vary from $84.4 \pm 8.9°$ to $171.4 \pm 4.6°$. Parameters such as the target, its position in the field of view and the instrument configuration (selected grating and grating angle) significantly affected the measured degree of instrumental polarisation. These results are summarised in Table 6.1.

The polarised standard data provided confirmation that the methods accurately extract the linear polarisation parameters as a function of wavelength with an average linear polarisation for Vela1 #95 of 7.64±0.08% from 6000Å to 8500Å at a position angle of 172.16±0.29°. Results for HD73882 show an average P_L of 1.96±0.04° at a PA of

Target	Grating	Artic.	Offset	$\mathbf{P_L}$	**PA**
HD14069	PG0300	13°	0'	$0.17 \pm 0.02\%$	$123.3 \pm 4.6°$
HD14069	PG0900	26.5°	0'	$0.24 \pm 0.04\%$	$129.2 \pm 5.5°$
HD14069	PG0900	40°	0'	$0.14 \pm 0.03\%$	$84.4 \pm 8.9°$
HD14069	PG0300	13°	+1.5'	$0.24 \pm 0.03\%$	$171.4 \pm 4.6°$
HD14069	PG0300	13°	-1.5'	$0.45 \pm 0.04\%$	$142.7 \pm 2.7°$
HD12021	PG0300	13°	0'	$0.32 \pm 0.02\%$	$131.8 \pm 1.9°$

Table 6.1: Weighted-mean values of the linear polarisation parameters of the observed unpolarised standard stars. Columns indicate the target, grating, articulation angle, offset (North) of the target in the field (in arc-minutes), the linear polarisation and the position angle.

168.7±0.6° from 4000Å to 6000Å and 2.06±0.03% at a PA of 164.5±0.4° from 6000Å to 9000Å. These results agree well to that available in the literature and by comparing them an essentially zero position angle correction of $-0.05 \pm 0.29°$ was estimated from the Vela1 #95 results, while a lower fidelity value was found for HD73882 of $-0.71 \pm 0.6°$[1]. This indicates that no gross offset is present and that the wavelength-dependent PA calibration curve (Figure 4.6) employed in the reduction process is sufficient to directly produce the correct equatorial position angle.

The E/O beam efficiency ratio analysed for each observation suggests that the coarse trend as a function of wavelength may be fairly predictable with the E-beam starting ∼10% less efficient in the blue and becoming ∼10% more efficient in the red. Large scale changes are a function of the grating selection and dispersion angle, but constant shifts over the wavelength range are also present from one observation to another unrelated to instrument configuration or target polarisation (seen for instance when comparing results for the two unpolarised standards HD14069 and HD12021 observed with the PG0300 grating). Possible target-dependent effects are also seen, for instance when

[1]The -4.37±0.6° offset implied by the blue coverage results are discounted here, based on the large systematic errors present in the raw data set.

comparing the blue-coverage PG0900 grating observations of HD14069 with those of HD73882, although parameters such as tracker trajectory were not constant. Characterisation of the E/O efficiency ratio at the small (0.1%) level would therefore require much more detailed sampling of the parameter space and assumes no time-dependence of such a model.

6.2 Recommendations and future work

6.2.1 Recommendations

A number of factors can influence the quality of spectropolarimetric data obtained with the SALT and RSS. Based on the data analysed in this study, some recommendations on observational, data preparation, spectrum extraction and data reduction techniques are listed below to aid future observations:

Observations

Accurate guidance during the observation is essential, as for any longslit spectroscopy observation, to avoid target drift across the slit that may lead to varying slit losses. Use of the SALT atmospheric dispersion compensator (ADC) is required to remove dispersion effect losses on the slit. Telescope focus and primary mirror stack quality should be good enough to avoid excessive slit losses and also signal overlap from higher orders if these are not masked using an order separation filter. Higher orders are especially prominent in PG0300 grating observations. Many of these issues will become less prominent as the SALT pointing model and guidance system is optimised and when the ADC is in place.

Calibration arc exposures should be taken before and after the waveplate sequence to ensure accurate wavelength calibration is possible. Typical arc lamps used for PG0300 and PG0900 observations were HgAr and Ne, respectively.

Data preparation

Preparing the data for analysis is easily performed via the standard SALT PyRAF pipeline reduction tools, but creation of data-quality masks and variance (error) planes is recommended to allow accurate propagation of errors. Tools to generate these planes have been created and will eventually be integrated as part of the SALT polarimetric reduction pipeline. Assuming good guidance and constant focus were achieved, cosmic ray masking should be performed by performing median-based sigma-clipping via the IRAF `imcombine` task, based on all the exposures of the waveplate sequence. Alternatively the standard `crmedian` task may be used, but this only uses a single frame to estimate the median and cosmic ray rejection levels.

Spectrum extraction

Similarly to cosmic ray masking, definition of the spectrum extraction apertures (via the `apall` task) should be performed on a median image based on all exposures of the waveplate sequence and kept constant when extracting the spectra from each exposure. Apertures should be chosen to include as much as possible of the spectral profile, while avoiding possible contamination from higher-order spectra. Background regions should typically also only be defined on one side of the aperture, to avoid higher-order spectra. Curvature of the spectra due to the polariser is easily mapped by a third or fifth order function. Using optimal extraction (employing variance weighting over the spectral profile) is recommended.

Spectra for both science and variance planes should be extracted, allowing the latter to be used as an error estimate when determining the polarisation parameters.

Obtaining polarisation parameters

Custom software for determining the polarisation parameters given the spectra from a waveplate sequence was developed and will be integrated into the SALT reduction

pipeline. Normalisation of the raw spectra from each exposure to the average O+E intensity of the waveplate sequence is essential to correct for the varying effective collecting area of the SALT during an observation. Co-addition, or binning, of data along the spectra can be used to greatly improve signal-to-noise to obtain more accurate estimates of the polarisation parameters within each bin.

6.2.2 Future outlook

While this study was successful in many respects, some artifacts and analysis issues came to light that needs to be addressed before spectropolarimetry can be efficiently performed with the RSS. Additional work is also required to extend the SALT pipeline reduction software to support spectropolarimetric observations.

Systematic error

The current transmission-based technique for estimating the systematic error seems inadequate as slowly varying wavelength-dependent errors remain in many cases when applied to the normalised spectra. An alternative systematic error estimate is therefore suggested, where comparing two estimates of the intensity (I_1 and I_2) separately for each polariser beam (see Eq. 4.13) is replaced by a comparison of the final Stokes parameters after combining the results from both beams, for instance Q_1 and Q_2, where Q_1 is determined from exposures 1 through 4 and Q_2 from exposures 5 through 8. Such an estimate then includes compensation for variations in E/O-beam efficiency during the observation.

Interference effects

In many cases a fast-varying oscillation or ripple contamination was observed in the raw spectra, especially for PG0900 grating data. From its appearance, this phenomenon seems to be induced by optical interference effects most likely caused by an air bubble

discovered in the optical coupling fluid of the Wollaston beam-spitter assembly. This has been corrected and transmission tests should confirm that this issue has been resolved.

Dual-beam polarimetry

The feasibility of characterising the variation in E/O beam efficiency as a function of instrument configuration, tracker position and target polarisation angle needs to be investigated to determine to what level of accuracy direct comparison of O- and E-beam intensities for obtaining polarisation parameters can be performed using RSS. This will aid in allowing more efficient observations of targets varying in intensity and/or polarisation over short timescales (hours), such as cataclysmic variable (CV) stars. Currently the method described in Section 4.4, using separate O- and E-beam analyses followed by combining the results from each, allows for canceling many variable transmission effects and remains the optimal reduction technique.

Reduction tools

The techniques and software developed for this study are applicable to the reduction of future RSS spectropolarimetry observations and needs to be used as a basis for extending the existing SALT PyRAF reduction tools to automate the process as far as possible.

References

Barnes, S. I., J. B. Hearnshaw, P. Cottrell, M. D. Albrow, and G. Kershaw. 2003. High resolution fiber-fed echelle spectrograph for the Southern African Large Telescope. In *Society of Photo-Optical Instrumentation Engineers (SPIE) Conference Series*, ed. M. Iye & A. F. M. Moorwood. Vol. 4841 pp. 1157–1161.

Buckley, D.A.H., J.B. Hearnshaw, K.H. Nordsieck, and D. O'Donoghue. 2003. Science drivers and first-generation instruments for the Southern African Large Telescope. In *Discoveries and Research Projects from 6- to 10-Meter Class Telescopes II*, ed. Gihathakurta Puraga. Vol. 4834 SPIE pp. 264–275.

Buckley, D.A.H. et al. 2004. The First-Generation Instruments for the Southern African Large Telescope. In *Ground-based Instrumentation for Astronomy*, ed. Alan F.M. Moorwood, and I. Masanori. Vol. 5492 SPIE pp. 60–74.

Burgh, E.B et al. 2003. Prime Focus Imaging Spectrograph for the Southern African Large Telescope: optical design. Vol. 4841 SPIE pp. 1463–1471.

Clarke, D., and J.F. Grainger. 1971. *Polarized light and optical measurement.* Oxford: Pergamon Press.

D'Odorico, S., H. Dekker, R. Mazzoleni, J. Vernet, I. Guinouard, P. Groot, F. Hammer, P. K. Rasmussen, L. Kaper, R. Navarro, R. Pallavicini, C. Peroux, and F. M. Zerbi. 2006. X-shooter UV- to K-band intermediate-resolution high-efficiency spectrograph for the VLT: status report at the final design review. In *Society of Photo-Optical Instrumentation Engineers (SPIE) Conference Series.* Vol. 6269

of *Presented at the Society of Photo-Optical Instrumentation Engineers (SPIE) Conference*.

Fossati, L., S. Bagnulo, E. Mason, and E. Landi Degl'Innocenti. 2007. Standard Stars for Linear Polarization Observed with FORS1. In *The Future of Photometric, Spectrophotometric and Polarimetric Standardization*, ed. C. Sterken. Vol. 364 of *Astronomical Society of the Pacific Conference Series* pp. 503–+.

Hass, G. 1965. *Applied Optics and Optical Engineering*. Vol. III New York: Academic Press p. 309.

Horne, K. 1986. "An optimal extraction algorithm for CCD spectroscopy." *Publications of the Astronomical Society of the Pacific* 96 (June):609–617.

Janesick, J.R. 2001. *Scientific Charged-Coupled Devices*. Bellingham, WA: SPIE.

Kobulnicky, H.A. et al. 2003. The Prime Focus Imaging Spectrograph for the Southern African Large Telescope: operational modes. Vol. 4834 SPIE pp. 264–274.

Landi Degl'Innocenti, E., S. Bagnulo, and L. Fossati. 2007. Polarimetric Standardization. In *The Future of Photometric, Spectrophotometric and Polarimetric Standardization*, ed. C. Sterken. Vol. 364 of *Astronomical Society of the Pacific Conference Series* pp. 495–+.

Mathewson, D. S., and V. L. Ford. 1970. "Polarization observations of 1800 stars." *Mem. R.A.S.* 74:139–+.

Nordsieck, K. H., E. B. Burgh, H. A. Kobulnicky, T. B. Williams, D. O'Donoghue, J. W. Percival, and M. P. Smith. 2001. The Prime Focus Imaging Spectrograph for the Southern African Large Telescope. In *Bulletin of the American Astronomical Society*. Vol. 33 of *Bulletin of the American Astronomical Society* pp. 1465–+.

Nordsieck, K. H., K. P. Jaehnig, E. B. Burgh, H. A. Kobulnicky, J. W. Percival, and M. P. Smith. 2003. Instrumentation for high-resolution spectropolarimetry in the visible and far-ultraviolet. In *Society of Photo-Optical Instrumentation Engineers (SPIE) Conference Series*, ed. S. Fineschi. Vol. 4843 SPIE pp. 170–179.

O'Donoghue, D. 2000. The correction of spherical aberration in the SALT. Vol. 4003 SPIE pp. 363–372.

O'Donoghue, D. et al. 2003. SALTICAM: $0.5M acquisition camera: every big telescope should have one. In *Society of Photo-Optical Instrumentation Engineers (SPIE) Conference Series*, ed. M. Iye & A. F. M. Moorwood. Vol. 4841 pp. 465–476.

Pancharatnam, S. 1955. Achromatic combinations of birefringent plates. In *Indian Acad. Sci.* Vol. A41 pp. 137–144.

Ramachandran, G.N., and S. Ramaseshan. 1961. *Handbuch der Physik*. Vol. 25 Berlin: Springer Verlag chapter Crystal optics, pp. 1–217.

Schurcliff, W. A., and S.S. Ballard. 1964. *Polarized light*. Princeton, N.J.: Van Nostrand Co.

Serkowski, K. 1974. *Planets, stars and nebulae studied with photo-polarimetry*. Tucson, Arizona: University of Arizona Press chapter Polarimeters for optical astronomy, pp. 135–174.

Serkowski, K., D. S. Mathewson, and V. L. Ford. 1975. "Wavelength dependence of interstellar polarization and ratio of total to selective extinction." *Ap. J.* 196 (February):261–290.

Stobie, R., J. Meiring, and D. A. Buckley. 2000. Design of the Southern African Large Telescope (SALT). In *Society of Photo-Optical Instrumentation Engineers (SPIE) Conference Series*, ed. P. Dierickx. Vol. 4003 pp. 355–362.

Stokes, G.G. 1852. "On the composition and resolution of streams of polarized light from different sources." *Transactions from the Cambridge Philosophical Society* 9:399–416.